Quantitative Imaging of Cerebral Oxygen Metabolism using MRI

Hannah V. Hare

A Thesis submitted for the Degree of
Doctor of Philosophy

Keble College
Nuffield Department of Clinical Neurosciences
University of Oxford
Trinity Term 2015

Quantitative Imaging of Cerebral Oxygen Metabolism using MRI

Hannah V. Hare
Keble College, University of Oxford
A Thesis Submitted for the Degree of Doctor of Philosophy
Trinity Term 2015

Abstract

Magnetic resonance imaging (MRI) is a non-invasive medical imaging technique that is sensitive to the level of oxygen in the blood. Calibrated MRI is capable of producing maps of absolute oxygen metabolism by using gas challenges to independently manipulate blood flow and blood oxygen content. In this thesis, several aspects of the signal model are investigated. It is confirmed that the commonly used Davis model is reassuringly insensitive to field strength, provided sufficient signal-to-noise (SNR) can be obtained. The effect in varying the experimental parameter of echo time is explored, and the results are shown to match the theory more closely when intravascular signal contribution is reduced by crusher gradients.

A direct comparison was performed between resting oxidative metabolism as measured by calibrated MRI and the gold standard method of positron emission tomography (PET). Good correlation was observed for resting blood flow, but no correlation was found for oxygen extraction fraction (OEF) or absolute cerebral metabolic rate of oxygen consumption ($CMRO_2$). A follow-up study was performed to further investigate some methodological aspects of the calibrated MRI procedure, including the application of background tissue suppression, different gas delivery methods, the effects of using measured respiratory timecourses as part of image analysis, and the impact of physiological noise correction.

The limiting factor in the quality of data obtained for calibrated MRI is the SNR of the arterial spin labelling (ASL) method, which is used to quantify blood flow to the brain. The alternative method of intravoxel incoherent motion (IVIM) was investigated, which is hypothesised to be sensitive to cerebral blood volume and perfusion without the signal limitations of ASL. However IVIM was shown to be primarily sensitive to the presence of cerebrospinal fluid within the brain, and thus is not a suitable alternative to ASL when quantification is of interest.

Acknowledgements

First and foremost, I must express my deepest gratitude to Dr Daniel Bulte for providing me with the support, encouragement and freedom to pursue the research leading up to this thesis. I cannot overstate how instrumental this support has been to me. Despite struggles with ethics, PET scanners, cyclotrons, MR scanner upgrades and the inevitable MR scanner crashes, we managed to keep a positive outlook and 'work our way through'. Special thanks also go to Prof. Peter Jezzard, whose door was always open for me.

I am grateful to Nicholas Blockley and Alan Stone for their many conversations and suggestions on improving protocols, to Robert Frost and James Meakin for help with pulse programming, and to the radiographers at AVIC and OCMR for their technical support. I also wish to thank all my collaborators at the Wolfson Brain Imaging Centre at Addenbrooke's Hospital for collecting and analysing the PET data, and Dr Nazneen Sudhan in particular for recruiting the subjects. Special thanks must go to all of the volunteers who have allowed me to scan them, without whom this thesis would have looked very empty indeed.

A special mention has to go to my fellow physics girls, Eleanor and Nadine, for so many good times – from baking a gingerbread scanner to a night out in Vegas, from canoeing across a Canadian lake to climbing up Angel's Landing, and of course, the innumerable coffee trips to keep ourselves motivated (or at least caffeinated) on those wet British days. We have learned and taught MRI together, and had many inspiring conversations along the way. The last three years would have been very different without you. Beyond this I wish to extend my thanks to the rest of the physics group for making FMRIB such a friendly and welcoming environment in which to work.

I would like to acknowledge the generous funding provided by the MRC for my studentship, and the additional support I received from the Keble Association and the Cairns Fund, which have allowed me to travel abroad to present my work at several international conferences.

Finally, I would like to thank my parents for their continued encouragement (despite the fact that I chose to study the 'foreign language' of science), my housemates for their baking, dinners and general entertainment, and Richard for his unwavering support throughout this endeavour.

Contents

List of Figures

List of Tables

List of Abbreviations

ASL	Arterial Spin Labelling
BOLD	Blood Oxygen Level Dependent
CBF	Cerebral Blood Flow
CBV	Cerebral Blood Volume
CSF	Cerebrospinal Fluid
CT	Computed Tomography
$CMRO_2$	Cerebral Metabolic Rate of Oxygen Consumption
D	Diffusion coefficient
D^*	Pseudo-diffusion coefficient
dHb	Deoxyhaemoglobin
FAIR	Flow-sensitive Alternating Inversion Recovery
f_v	Fractional content of capillary blood volume in a voxel
GLM	General Linear Model
GM	Grey Matter
GRE	Gradient Echo
IVIM	Intravoxel Incoherent Motion
MRI	Magnetic Resonance Imaging
NIRS	Near-Infrared Spectroscopy
OEF	Oxygen Extraction Fraction
PCASL	Pseudo-Continuous Arterial Spin Labelling
PET	Positron Emission Tomography
RF	Radio Frequency
SAR	Specific Absorption Rate
SE	Spin Echo
SNR	Signal-to-Noise Ratio
SPECT	Single Photon Emission Computed Tomography
T_1	Longitudinal relaxation time
T_2	Transverse relaxation time (irreversible)
T_2^*	Transverse relaxation time (includes reversible component)
TE	Echo Time
TR	Repetition Time
WM	White Matter

Declaration of the Contribution of Others

1. The BOLD signal simulations discussed in Chapter 4 were carried out by Nicholas Blockley.
2. Acquisition and initial data processing of PET images in Chapter 6 were performed by staff at the Wolfson Brain Imaging Centre at Addenbrooke's Hospital, Cambridge. For this I am very grateful to the following people: Nazneen Sudhan, Joanna Simpson, Joseph Donnelly, Xiuyun Liu and Jonathan Coles.
3. A separate study comparing resting OEF as measured by NIRS and PET was performed in parallel with the MRI–PET comparison described in Chapter 6. This study is referenced in Chapter 6, and all data collection, processing and analysis were performed by the scientists at the Wolfson Brain Imaging Centre, as mentioned above.

List of Publications

Journal Articles

1. **Hannah V. Hare**, Michael Germuska, Michael E. Kelly, Daniel P. Bulte. Comparison of CO2 in air versus carbogen for the measurement of cerebrovascular reactivity with magnetic resonance imaging. *Journal of Cerebral Blood Flow and Metabolism*, 33(11):1799–1805, 2013.

2. **Hannah V. Hare**, Nicholas P. Blockley, Alexander G. Gardener, Stuart Clare, Daniel P. Bulte. Investigating the field-dependence of the Davis model: Calibrated fMRI at 1.5, 3 and 7 T. *NeuroImage*, 112:189–196, 2015.

3. **Hannah V. Hare**, Daniel P. Bulte. Investigating the dependence of the BOLD calibration constant M on echo time. *Magnetic Resonance in Medicine*, 2015. DOI: 10.1002/mrm.25603.

4. Nicholas P. Blockley, Valerie E. Griffeth, Alan J. Stone, **Hannah V. Hare**, Daniel P. Bulte. Sources of systematic error in calibrated BOLD based mapping of baseline oxygen extraction fraction. *NeuroImage*, 122:105–113, 2015.

Conference Proceedings

1. **Hannah V. Hare**, Michael Germuska, Daniel P. Bulte. Carbogen for CVR? In *Proceedings of the British Chapter ISMRM Postgraduate Symposium*, London, UK, 2013.

2. **Hannah V. Hare**, Michael Germuska, Daniel P. Bulte. Comparison of CO2 in air versus carbon for the measurement of cerebrovascular reactivity with magnetic resonance imaging. In *Proceedings of the 21st Annual Meeting ISMRM*, Salt Lake City, USA, 2013.

3. **Hannah V. Hare**, Nicholas P. Blockley, Alexander G. Gardener, Michael Germuska, Stuart Clare, Daniel P. Bulte. Calibrated fMRI at 1.5, 3 and 7T: a comparative study. In *Proceedings of the British Chapter ISMRM Postgraduate Symposium*, Cardiff, UK, 2014.

4. Michael Kelly, **Hannah Hare**, Michael Germuska, Nicola Filippini, Daniel Bulte. Changes in cerebral physiology with ageing assessed by respiratory-calibrated MRI. In *Proceedings of the 22nd Annual Meeting ISMRM*, Milan, Italy, 2014.

5. **Hannah V. Hare**, Nicholas P. Blockley, Alexander G. Gardener, Michael Germuska, Stuart Clare, Daniel P. Bulte. Investigating the field-dependence of the Davis model: calibrated fMRI at 1.5, 3 and 7 tesla. In *Proceedings of the 22nd Annual Meeting ISMRM*, Milan, Italy, 2014.

6. **Hannah Hare**, Daniel Bulte. Investigating the dependence of the BOLD calibration constant M on echo time. In *Proceedings of the 20th Annual Meeting of the British Chapter ISMRM*, Edinburgh, UK, 2014.

7. **Hannah Hare**, Nicholas Blockley, Alexander Gardener, Stuart Clare, Daniel Bulte. A multi-field comparison of gas calibrated fMRI. In *Proceedings of the 2nd International Symposium on Imaging Cerebral Physiology*, Leipzig, Germany, 2014.

8. **Hannah Hare**, Daniel Bulte. Investigating the dependence of the BOLD calibration constant M on echo time. In *Proceedings of the 2nd International Symposium on Imaging Cerebral Physiology*, Leipzig, Germany, 2014.

9. J. Simpson, N. Sudhan, **H. Hare**, J. Donnelly, X. Liu, F. Aigbirhio, T. Fryer, G. Stocks-Gee, P. Smielewski, D. Bulte, J. Coles. Comparison of steady-state 15oxygen positron emission spectroscopy and near-infra red spectroscopy for quantitative measurement of cerebral physiology. In *Proceedings of the 35th International Symposium on Intensive Care and Emergency Medicine*, Brussels, Belgium, 2015.

10. **Hannah Hare**, Daniel Bulte. Oxygen saturation changes during hyperoxic and hypercapnic stimuli measured by near infrared spectroscopy (NIRS) cerebral oximetry. In *Proceedings of the 23rd Annual Meeting ISMRM*, Toronto, Canada, 2015.

11. **Hannah Hare**, Daniel Bulte. The impact of echo time on the calibration parameter M. In *Proceedings of the 23rd Annual Meeting ISMRM*, Toronto, Canada, 2015.

12. Daniel Bulte, **Hannah Hare**, Nazneen Sudhan, Joanna Simpson, Joseph Donnelly, Xiuyun Liu, Jonathan Coles. Multimodal validation of physiological MRI: Triple oxygen PET and NIRS. In *Proceedings of the 23rd Annual Meeting ISMRM*, Toronto, Canada, 2015.

13. **Hannah Hare**, Daniel Bulte. Using IVIM to measure cerebral perfusion: a direct comparison with arterial spin labeling (ASL). In *Proceedings of the Organization for Human Brain Mapping*, Honolulu, Hawaii, 2015.

1

Introduction

1.1 Motivation

Magnetic resonance imaging (MRI) is capable of acquiring high resolution, non-invasive images of the brain, providing both structural and functional information. This includes providing exceptional soft tissue contrast in anatomical images, localising areas of neural activation and visualising the connectivity between different structures within the brain. Whilst such qualitative images are doubtless invaluable to clinical diagnosis and treatment planning, the clinical application of functional MRI has remained very limited. This is due in large part to the complexity of the blood oxygen level dependent (BOLD) signal, which is at least as sensitive to local blood volume as it is to oxygenation. When the normal flow-metabolism coupling is affected by a pathology, it is possible to observe no change or even decreases in BOLD signal, despite normal underlying increases in oxygen consumption, making the resulting 'activation maps' rather difficult to interpret.

Until recently, positron emission tomography (PET) was the only method capable of providing quantitative information on the delivery and consumption of nutrients and oxygen to the human brain. Because all PET scans require the injection of radioactive tracers, they may only be performed when the perceived benefits outweigh the known risks; thus the method is not ideal for the investigation of healthy human brain function, nor is it suitable for routine use with paediatric patients. Unlike PET, MRI has no associated ionising radiation risks, is faster and cheaper to perform clinically, and is more widely available at hospital sites across the world.

The development of a reliable, non-invasive method of quantifying physiological parameters including cerebral blood flow (CBF), cerebral blood volume (CBV), oxygen extraction fraction (OEF) and cerebral rate of oxygen consumption ($CMRO_2$) using MRI would find wide clinical application for the monitoring of neurovascular disease. This could aid clinical diagnoses, treatment planning, longitudinal monitoring of patients and drug development, as well as basic research into how neurological diseases present and progress. In addition it would become feasible for the first time to investigate mismatches in CBF, OEF and $CMRO_2$ as potential biomarkers for a wide range of diseases, including neurodegenerative conditions (such as multiple sclerosis, Alzheimer's and Parkinson's diseases), oncology and psychiatric disorders (for example depression and schizophrenia).

Recent work carried out in Oxford [1], Montreal [2] and Cardiff [3] has culminated in the development of an MR imaging protocol capable of producing voxelwise maps of CBF, OEF and $CMRO_2$. Initial results have been encouraging, and compare well with previous data acquired by other modalities such as PET. However a direct comparison between the two has yet to be attempted, and a series of assumptions are made during the analysis of imaging data which may vary significantly within a patient population.

1.2 Thesis outline

First, a brief overview of MR image and contrast generation is given in Chapter 2. This is followed by a review of a range of imaging methods capable of measuring aspects of cerebral metabolism, including PET, MRI and near-infrared spectroscopy (NIRS). In Chapter 4 a calibrated BOLD MRI experiment is performed at 1.5, 3 and 7 T to explore how sensitive the Davis model is to field strength. Chapter 5 investigates the impact of echo time on the calibration parameter M, with and without the application of intravascular signal crushing gradients. In Chapter 6 calibrated MRI is performed alongside triple oxygen PET in a head-to-head comparison. Chapter 7 consists of a closer examination of several aspects of the calibrated MRI methodology, encompassing both experimental setup and analysis procedure. Chapter 8 explores the alternative method of intravoxel incoherent motion (IVIM) for generating perfusion-sensitive contrast. Finally, a summary and some suggestions for future work are given in Chapter 9.

2

Theory

In this chapter a brief overview is given of the physics underlying the field of magnetic resonance imaging (MRI), including the source of signals, the process of image formation and the principles of contrast generation. It is not intended to be an exhaustive introduction to MRI, and will focus primarily on the imaging methods used later in this thesis. More detailed discussions on the subject may be found elsewhere, for example in references [4–7].

2.1 MR Physics

MRI is unique amongst medical imaging methods in its flexibility. It is possible to vary the contrast between tissue types depending on the part of the body or the pathology that is of interest. Because it does not rely on the use of a tracer, one can take many repeated images and acquire a timecourse. This can be useful for monitoring continuous processes like the beating of a heart, or for measuring responses to external stimuli applied during the course of a scan, as in the case of functional brain imaging. Unlike many medical imaging methods, no damaging ionising radiation is involved, so there is no limit to the number of scans a person should be subjected to over the course of a lifetime. This section introduces the physical principles that underlie magnetic resonance, and outlines the steps involved in producing useful three-dimensional images.

2.1.1 Nuclear Magnetic Resonance

Any nucleus with an odd number of nucleons (protons plus neutrons) will have a non-zero value of spin. ‘Spin’ is a quantum phenomenon which may be thought of conceptually as the atomic nucleus spinning about its own axis very quickly, giving it a unit of angular momentum. This spin induces a magnetic moment which will interact with any externally applied magnetic fields. In the presence of a uniform static magnetic field, $\mathbf{B}_0$, the nuclear magnetic moment will tend to align with the direction of this field. By doing so it will be either parallel or anti-parallel to $\mathbf{B}_0$; both states exist and are relatively stable, but the parallel state has a lower energy associated with it, so an atom is more likely to favour this state. Across a large sample of atoms there will always be slightly more nuclei in the parallel than the anti-parallel state, which gives rise to a macroscopic magnetisation vector $\mathbf{M}$.

Because a spin has both a magnetic moment and angular momentum, it will precess about an external field with an angular frequency given by

$$\omega_0 = \gamma B_0 \tag{2.1}$$

where ω_0 is called the resonant or Larmor frequency. γ is the gyromagnetic ratio, which is a constant for any given type of nucleus, but varies between elements. This is how the abundance of different nuclei may be identified in nuclear magnetic resonance (NMR) spectroscopy experiments.

In the context of imaging, hydrogen nuclei (protons) are by far the most abundant NMR-active species in the human body. Thus the rest of this chapter –

indeed, the majority of MRI in general – is concerned only with the manipulation of signals generated from the excitation and subsequent relaxation of hydrogen nuclei.

2.1.2 Excitation

A magnetisation vector may be tipped away from its equilibrium position (which is parallel to $\mathbf{B}_0$) by briefly applying a second magnetic field $\mathbf{B}_1$ that rotates at the Larmor frequency. As the magnetisation returns to its lowest energy state, it emits photons at this same Larmor frequency. Thus the same hardware may be used to transmit and receive these electromagnetic waves. As the Larmor frequency of hydrogen atoms is in the radio frequency range, the applied magnetic fields are known as 'RF pulses' and the hardware as an 'RF coil'.

The longer an RF pulse is played out for, the further the magnetisation is tipped away from the $\mathbf{B}_0$ direction (which by convention also defines the positive z-axis). It is often useful to describe this motion from the reference frame of a rotating spin (the 'rotating frame'), in which precession does not need to be explicitly modelled and rotating $\mathbf{B}_1$ fields appear constant. In this frame, the angle $\Delta\theta$ by which a spin's magnetisation is rotated away from $+z$ is given by

$$\Delta\theta = \gamma B_1 \tau \tag{2.2}$$

where τ is the duration of $\mathbf{B}_1$ and the value of γ for protons is 42.6 MHz T^{-1}.

RF pulses are commonly described in terms of the angle $\Delta\theta$ that they produce; for example a 90° 'excitation' pulse tips $\mathbf{M}$ into the transverse x-y plane, and a 180° 'inversion' pulse will result in $\mathbf{M}$ pointing along the $-z$ instead of $+z$ direction, as shown in figure 2.1.

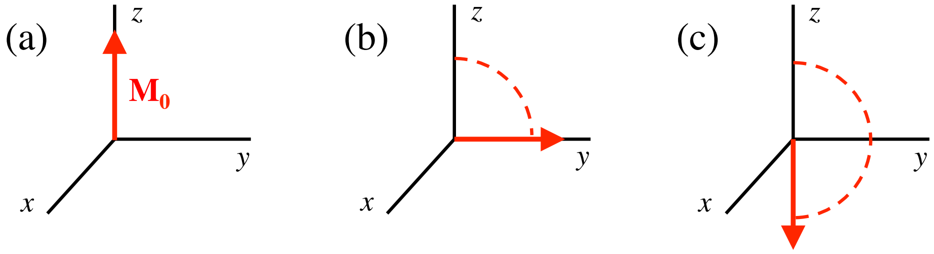

Figure 2.1: At equilibrium, the magnetisation vector $\mathbf{M}_0$ points along $+z$ (a). After a 90° pulse $\mathbf{M}$ lies in the transverse plane (b), and after a 180° pulse it is inverted (c). The trajectories are shown in the rotating frame of reference. By convention, the z-axis is chosen to coincide with the external $\mathbf{B}_0$ field, which is also the direction of the equilibrium magnetisation $\mathbf{M}_0$.

2.1.3 Relaxation

After a spin has been excited by an RF pulse, its magnetisation is no longer aligned with $\mathbf{B}_0$. However, over time, the magnetisation vector will realign with the external field in a process known as relaxation. The rate at which longitudinal magnetisation $\mathbf{M}_z$ is recovered after a 90° excitation is described by

$$M_z = M_0(1 - e^{-t/T_1}). \tag{2.3}$$

Similarly, the transverse magnetisation component $\mathbf{M}_{xy}$ decays back to zero according to

$$M_{xy} = M_0 e^{-t/T_2}. \tag{2.4}$$

T_1 and T_2 are characteristic time constants that describe the longitudinal and transverse magnetisation relaxation, respectively.

In addition to the relaxation processes described above, which are irreversible thermal processes, external effects can have an additional impact on the rate of transverse relaxation. Any small field inhomogeneities will cause protons to precess at slightly different rates; observed from the rotating reference frame, this looks like a gradual dephasing of a collection of spins (figure 2.2). To

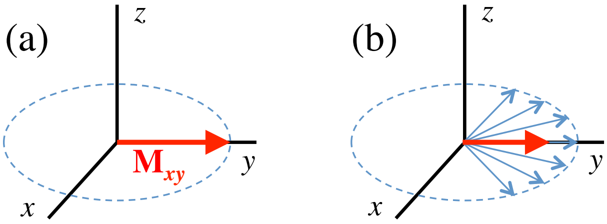

Figure 2.2: Over time spins with subtly different resonant frequencies will change from being in phase (a) to out of phase (b). The resultant $\mathbf{M}_{xy}$ vector has a smaller amplitude than any of the individual components, leading to T_2^* decay.

distinguish this effect, the apparent transverse relaxation rate as measured with a simple gradient echo sequence is denoted T_2^*. This will always be smaller than T_2, as dephasing increases the rate at which signal is 'lost' over time. Unlike intrinsic T_2 decay, the contribution from dephasing may be recovered by applying an extra 180° pulse, so pure T_2 may be measured using a spin echo sequence.

2.1.4 Gradient Echo and Spin Echo Sequences

Following an excitation pulse, both transverse and longitudinal relaxation will occur simultaneously; however, by varying the timing and number of RF pulses, the contrast in the resulting images can be carefully manipulated.

The two most basic pulse sequences are gradient echo (GRE) and spin echo (SE). A gradient echo sequence consists of an initial excitation pulse, typically but not always a 90° pulse, which is followed by a signal readout. Note that during a readout, the signal measured always depends on the *transverse* magnetisation magnitude only (which in turn depends on the longitudinal magnetisation prior to the excitation pulse). Thus by varying the echo time (TE, time between excitation and readout) and the repetition time (TR, time between successive excitations) the relative contributions of T_1 and $T_2^{(*)}$ relaxation may be controlled. This is shown in figure 2.3. To maximise T_1 contrast both TE and TR are kept short; conversely to enhance $T_2^{(*)}$ contrast long TE and TR values

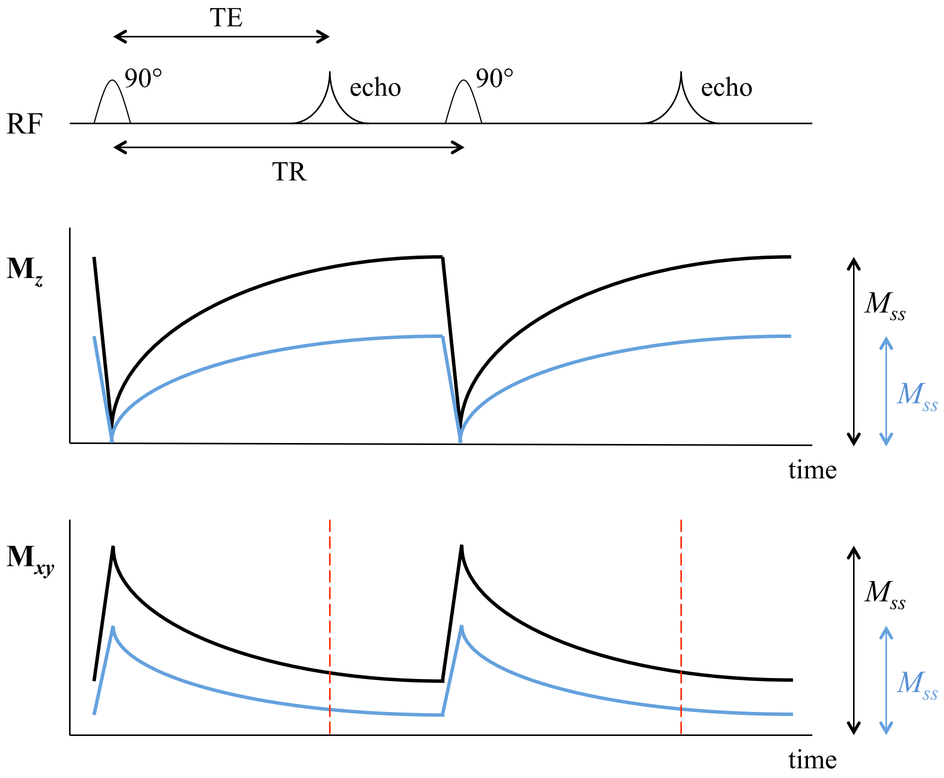

Figure 2.3: Gradient echo pulse sequence (top) and timecourses of the longitudinal magnetisation $\mathbf{M}_z$ (middle) and transverse magnetisation $\mathbf{M}_{xy}$ (bottom). The blue line represents spins with a longer T_1 than those shown in black. Because a 90° pulse is being used, the maximum longitudinal steady state magnetisation M_{ss} is the same as the maximum transverse steady state magnetisation. The red dashed lines indicate when the signal readouts occur, and the image contrast is determined by the difference in transverse magnetisation between spin species (blue and black) at this time.

are used. A gradient echo sequence is sensitive only to the *apparent* transverse relaxation time, T_2^*.

In a spin echo sequence, a 180° pulse is added between the excitation pulse and the readout. This acts to bring the dephased transverse magnetisation components back into phase, known as refocussing. By doing so the dephasing effects of an inhomogeneous field are 'cancelled out', and the underlying T_2 contrast may be recovered. The 180° refocussing pulse is played out at time TE/2 in order to maximise the signal at the readout time TE, as shown in figure 2.4.

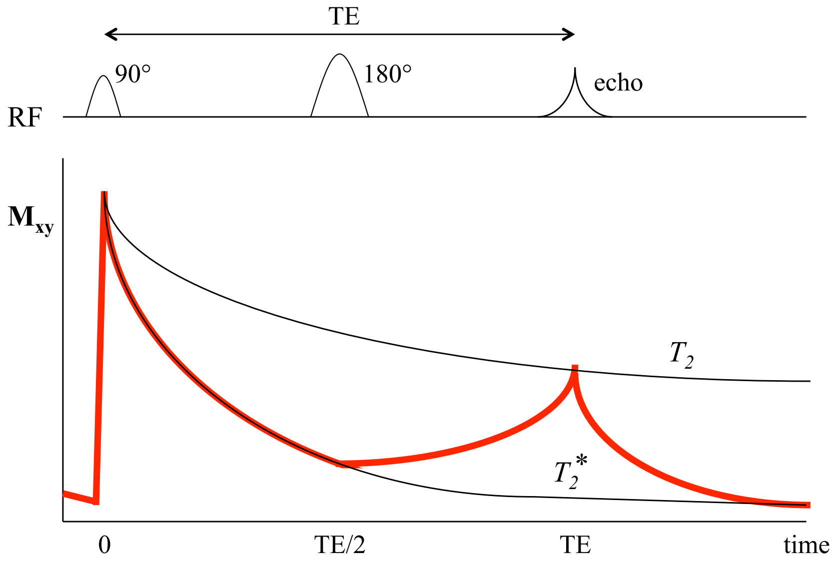

Figure 2.4: Spin echo pulse sequence (top) and transverse magnetisation timecourse (red line, bottom). The magnetisation decays with time constant T_2^* until a 180° pulse refocusses it at the echo time (TE). The intrinsic T_2 signal loss is inevitable and cannot be recovered.

2.1.5 Image Formation

The key innovation in moving from NMR spectroscopy to MR imaging was the application of additional magnetic field gradients to spatially encode signal information. This concept was first demonstrated by Paul Lauterbur and Peter Mansfield, for which they shared the Nobel Prize in Physiology or Medicine in 2003.

Magnetic field gradients change the magnitude (but *not* the direction) of the static field as a function of space. This causes the resonant frequency of spins to vary across the sample (see equation 2.1), providing information on the location as well as the state of the spins. In order to create a 3-dimensional image, spatial information has to be encoded in all 3 directions. This is done by applying gradients along different directions at specific times during the pulse sequence.

2.1.5.1 Slice Selection

The first step in most sequences is to excite spins away from their equilibrium magnetisation, as described in section 2.1.2. By applying a z-gradient during this excitation, the Larmor frequency varies with z, but the RF pulse is applied over a much smaller range of frequencies. Only those spins whose resonant frequencies match the applied RF pulse become excited. In this way, only a thin slice is excited (the thickness of which is determined by the bandwidth of the RF pulse and the strength of the applied gradient), reducing the imaging problem to 2 dimensions.

2.1.5.2 Frequency and Phase Encoding

In order to get information on the x-y positions of the spins, gradients are again used to alter the temporal characteristics of the signals. In frequency encoding, an x-gradient is applied continuously during data acquisition so that the Larmor frequency of the spins is directly dependent on their x-position within the scanner (figure 2.5(a)). In phase encoding, a y-gradient is briefly played out in order to alter the relative phases of spins according to their y-position, and then turned off again so that their frequencies remain unaffected (figure

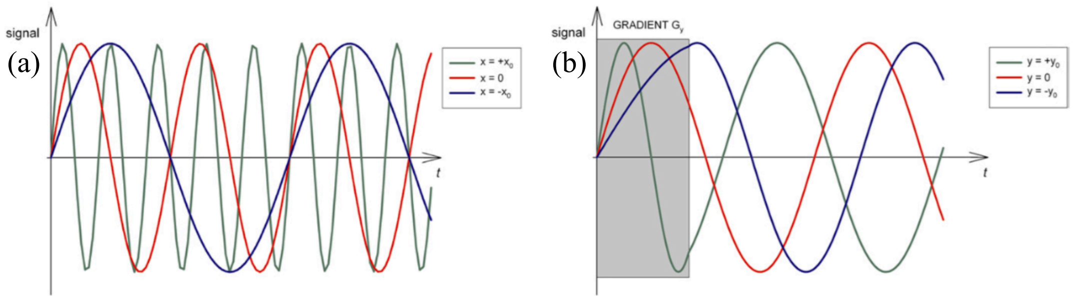

Figure 2.5: Schematic showing how frequency encoding (a) and phase encoding (b) are applied. In frequency encoding, an x-gradient is applied throughout. In phase encoding, a short y-gradient is applied immediately before image acquisition.
© *IOP Publishing. Reproduced with permission. All rights reserved.* [8]

2.5(b)). As the phase and frequency of a signal are independent properties, it is straightforward to combine these two forms of encoding, such that both x and y co-ordinates may be recovered from a single 2D signal readout.

2.1.5.3 k-Space

While the above discussion on frequency and phase encoding makes sense for point sources, imaging becomes a little more complex when dealing with large (real) objects. Mathematically, the intensity I of a slice of thickness Δz depends on the proton density ρ according to

$$I(x,y) = \int_{-\Delta z/2}^{+\Delta z/2} \rho(x,y,z)\,\mathrm{d}z \tag{2.5}$$

and the signal measured during an MRI experiment can be written

$$S(t) = \iint_{\text{slice}} I(x,y)e^{-i\phi}\,\mathrm{d}x\,\mathrm{d}y. \tag{2.6}$$

Here ϕ is the total accumulated phase of the proton spins

$$\phi = \gamma \int_0^t \big(G_x(\tau)x + G_y(\tau)y\big)\,\mathrm{d}\tau \tag{2.7}$$

where G_x and G_y are the magnitudes of the gradient fields applied along x and y respectively. By defining the new variables

$$k_x = \frac{\gamma}{2\pi}\int_0^t G_x(\tau)\,\mathrm{d}\tau \quad \text{and} \quad k_y = \frac{\gamma}{2\pi}\int_0^t G_y(\tau)\,\mathrm{d}\tau$$

it becomes clear that the signal is simply the Fourier transform of the intensity we are interested in,

$$S(k_x, k_y) = \iint_{\text{slice}} I(x, y) e^{-i2\pi(k_x x + k_y y)}\, \mathrm{d}x\, \mathrm{d}y, \tag{2.8}$$

so

$$S(k_x, k_y) = \mathrm{FT}[I(x, y)] \quad \text{and} \quad I(x, y) = \mathrm{FT}^{-1}[S(k_x, k_y)].$$

The aim of any readout method is to sample k-space as efficiently as possible. Echo-planar imaging (EPI) is one common approach, and is shown in figure 2.6. Its speed makes it particularly well-suited to functional MRI where high temporal resolution is a priority; however it can suffer from significant artefacts as a result.

2.2 MR Contrast

For an image to be of any use at all, it must contain some form of contrast. The simplest MR contrast mechanism is to make use of the inherent differences in T_1 and T_2 properties of different types of tissue to produce T_1- or T_2-weighted images, respectively (see section 2.1.4). The remainder of this chapter deals with alternative mechanisms for introducing contrast into MR images, with a

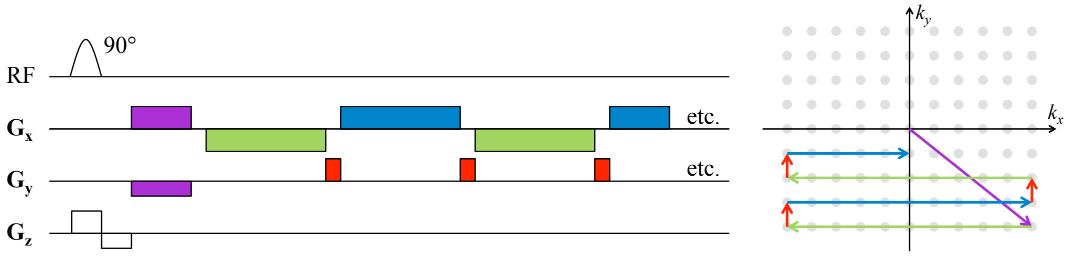

Figure 2.6: Schematic diagram of an EPI readout. On the left is the pulse sequence, on the right the corresponding trajectory through k-space.

particular focus on functional contrasts: methods which are sensitive to the haemodynamic changes that accompany neuronal activation. The existence of such functional contrast mechanisms, alongside the flexibility to choose suitable tissue contrasts, is what sets MRI apart from other imaging modalities such as computed tomography (CT), single photon emission computed tomography (SPECT) or positron emission tomography (PET).

2.2.1 BOLD Contrast

The Blood Oxygen Level Dependent (BOLD) signal is probably the most well known functional contrast in MR imaging. First discovered by Ogawa *et al.* in 1990 it provides a contrast sensitive to the oxygenation of blood, capable of indirectly imaging local neural activity [9].

The physical origin of the BOLD contrast is the difference in properties between diamagnetic oxyhaemoglobin (oxy-Hb) and paramagnetic deoxyhaemoglobin (dHb). Higher concentrations of dHb lead to an increased dephasing of nearby magnetic moments, shortening T_2^*. This leads to a reduction in the observed MR signal during a simple T_2^*-weighted GRE sequence. Conversely, high blood oxygenation leads to low concentrations of dHb, long T_2^* and increased MR signal.

Functional MRI (fMRI) studies make use of the BOLD contrast to localise sites of neuronal activation [10, 11]. When a region of the brain is ‘activated’, typically in response to an external stimulus, neurons fire at increased rates and require more oxygen and glucose to fulfil their increased energy need. (For more details on neuronal metabolism see section 3.1.) To meet this higher demand, arterioles dilate to increase local cerebral blood flow (CBF) and blood volume (CBV) in order to supply fresh, oxygenated blood at a faster rate. In the healthy brain the vasculature actually overcompensates for the increased

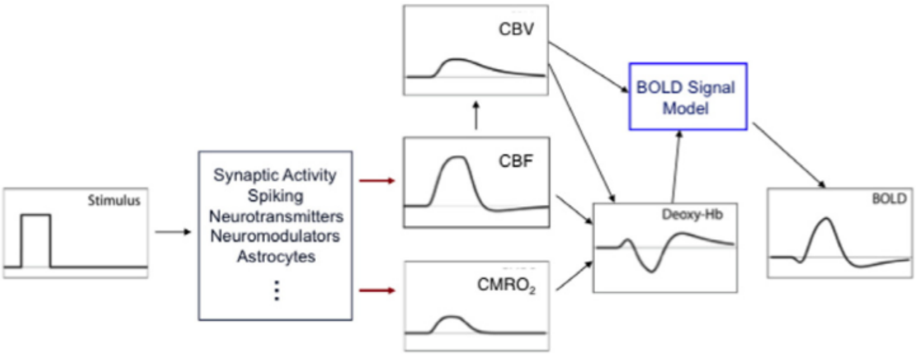

Figure 2.7: The sequence of physiological processes that take place during neuronal activation. Concomitant changes in CBV, CBF and CMRO$_2$ lead to the typical BOLD haemodynamic response function, which includes the well-known post-stimulus undershoot and the still somewhat controversial initial dip.
© *Elsevier. Reproduced with permission. All rights reserved.* [12]

demand, resulting in a *higher* oxy-Hb to dHb ratio in active regions which in turn leads to longer T_2^* and higher BOLD signal.

Thus it is the mismatch between oxygen supply (via CBF and CBV) and demand (the cerebral metabolic rate of oxygen consumption, CMRO$_2$) which leads to an observable BOLD signal. The BOLD signal modulation that is observed after presentation of a short or instantaneous stimulus is known as the haemodynamic response function and is shown in figure 2.7.

2.2.2 Arterial Spin Labelling

Arterial Spin Labelling (ASL) allows for the direct imaging of the flow of blood through the brain without the need for an exogenous tracer. The basic principle is to use magnetic fields and RF pulses to selectively label spins in a slab of the brain; the blood flowing out of this slab into unlabelled brain matter can then be tracked for as long as the label persists. Subtraction of a labelled image from a control, where blood has not been tagged, yields an image of those spins that have moved from the labelling site to the imaging region. This makes ASL sensitive to both cerebral blood flow (CBF) and perfusion. Strictly speaking, perfusion specifically refers to the delivery of fresh blood to the capillary bed, from where oxygen and nutrients can pass into the surrounding cells. In practice the terms CBF and perfusion are used interchangeably, and both are quoted in units of ml blood/100 g brain tissue/minute. Note that both of these measures are defined as rates rather than fluxes, meaning that they are independent of voxel volume.

Many different labelling schemes have been implemented to acquire ASL images, some of which are shown in figure 2.8. They fall into two main categories: pulsed ASL, in which well-defined volumes of blood are targeted, and continuous ASL, in which all the blood flowing into the brain through the vertebral and carotid arteries is tagged continuously. These methods are discussed below in some detail, but all sequences follow the same basic design: there is a tagging period, followed by an inflow delay time and then the readout. Alternate acquisitions (TRs) apply the control condition during the tagging period. The inflow delay time allows for tagged spins to travel down the vascular tree; short delay times result in angiography images of primarily arterial blood, and longer times are more sensitive to capillary flow and tissue perfusion. This delay time may also be used to apply any background suppression or selective saturation pulses.

The actual ASL signal is the tag-control difference, which is only 0.5–1.5% of the total MR signal [13], giving it an inherently reduced SNR compared to most other imaging methods. Despite these SNR issues, using ASL to measure blood flow has significant advantages over the use of intravenous tracers with PET, SPECT, CT or MRI. ASL is both noninvasive and able to make multiple repeated local measurements over the course of a single scan, whilst significantly increasing subject comfort.

The ASL label decays with a time constant equal to T_1 of arterial blood, which is on the order of 1 second, making it possible to take a new image every

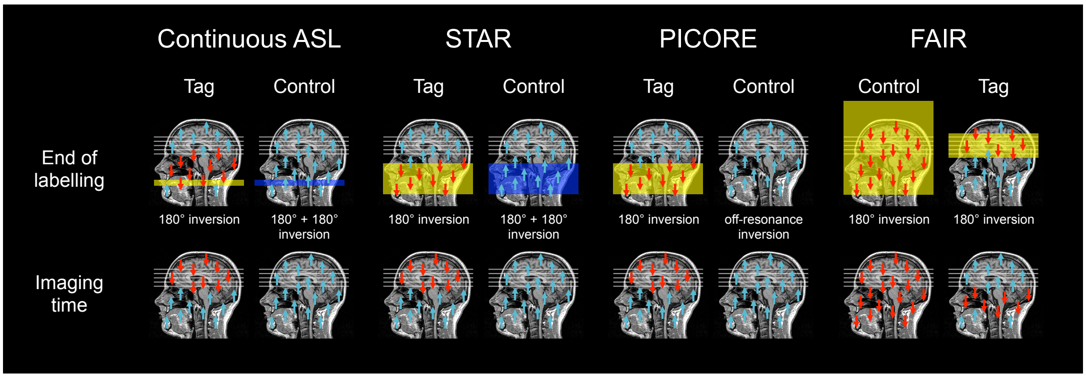

Figure 2.8: Schematic diagram of the most common ASL methods: continuous tagging, STAR, PICORE and FAIR. Arrows represent proton spins, where blue spins are aligned with the external field $\mathbf{B}_0$ and red spins have been inverted to be anti-aligned. The magnetisation of static tissue is not shown. The top row shows the state of spins at the end of the labelling period; for continuous tagging this can last 2–4 s, for the pulsed techniques only on the order of 50 ms. The bottom row shows where the tagged spins may be located at the time of image acquisition, typically 1–2 s after the end of the labelling period.

few seconds. While the relatively short-lived magnetic label leads to several significant benefits of ASL over other techniques for measuring CBF, it also puts an intrinsic limitation on the time period during which the blood can be traced. This can make it difficult to image slow CBF, for example in patients with significant collateral flow following a stroke or in certain cerebrovascular diseases. Nonetheless, the technique is starting to make the transition from research into clinical settings [14].

2.2.2.1 Continuous ASL

In Continuous ASL (CASL), all blood flowing through a particular slice (typically in the neck) is inverted during the tagged condition. As the blood travels into the imaging slice it will reduce the signal compared to the non-tagged situation; subtraction of the tag and control images will yield a qualitative map of the perfusion of the imaged slice. Conceptually this is a very simple method, however in practice most scanners are not capable of creating the long, continuous

RF excitation required.

2.2.2.2 Pulsed ASL

Whilst continuous arterial tagging creates a bolus of inverted blood that is well defined in time, pulsed techniques produce a bolus with good spatial definition. Pulsed ASL (PASL) also has the advantage that it is much easier to implement on standard clinical scanners as no additional hardware is required. It also has a lower rate of power deposition due to the less frequent application of RF pulses which is useful on ultra-high field scanners, where sequence protocols are SAR-limited for safety reasons.

STAR

Signal Targeting with Alternating Radio frequency (STAR) applies an inversion to a slab proximal to the imaging region [15]. If quantitative images are required, it is necessary to carefully control for the effects of magnetisation transfer by also applying an inversion slab to the control image. This may be done by locating the control inversion slab above rather than below the imaging slice, at an equal distance as to the tagging inversion slab, such that the two are symmetric about the imaging plane. Alternatively, it is possible to apply two 180° pulses in the same location as the 180° tagging pulse, each at half of the labelling power.

PICORE

Proximal Inversion with a Control for Off-Resonance Effects (PICORE) is a variant of STAR which allows for quantitative perfusion imaging using only a single slab-selective inversion pulse [16]. The method for acquiring tagged images is identical to STAR, but an off-resonance inversion pulse is played out during the control condition. This has the same frequency offset to the imaging slice as the tag but it is applied without an accompanying slab selective gradient. This method has the advantage of not tagging venous blood during control image acquisition.

FAIR

In a Flow-sensitive Alternating Inversion Recovery (FAIR) sequence the tag image is acquired by applying a non-selective inversion pulse to the entire field of view of the RF coil [17]. A second control image is obtained in which slice-selective gradients are added such that only a slab of slightly larger dimensions than the imaging volume is inverted. Only signal from those spins that flow into the imaging volume during the delay time remain after subtraction of the two images. This signal difference is proportional to CBF, although precise quantification would require knowledge of blood transit times and T_1 of blood as well as sequence timing parameters.

If the imaging volume does not extend to the top of the head, this technique will be sensitive to venous as well as arterial blood. However, an advantage of FAIR over other pulsed imaging techniques is that it is less sensitive to static signal artefacts due to $\mathbf{B}_1$ inhomogeneity (which typically worsens towards the edges of the RF coil), making it better suited to ultra-high field perfusion experiments at 7T or above [18].

Quantification with QUIPSS

All three commonly employed methods of pulsed ASL are capable of producing qualitative maps of CBF. In theory they can also produce quantitative information on flow increases upon activation, but this relies on the assumption that tagged blood flows immediately into the imaging slice, and neglects the fact that the tagged bolus flowing into the imaging slice will have a spatially varying amount of T_1 decay, which may be altered during a state of activation. Two methods proposed by Wong *et al.* called Quantitative Imaging of Perfusion using a Single Subtraction (QUIPSS) I and II allow for the direct acquisition of quantitative information by the application of additional saturation pulses during the tagging procedure [19]. The methods can be used in conjunction with STAR, PICORE or FAIR tagging.

The full equation for the magnetisation difference between tag and control images acquired using any quantitative method of pulsed ASL (in which a good control image has been acquired) is [20]

$$\Delta M(t) = \begin{cases} 0 & 0 < t < \delta t \\ 2M_{0b} f(t - \delta t) \alpha e^{-t/T_{1b}} q(t) & \delta t < t < \tau + \delta t \\ 2M_{0b} f(\tau) \alpha e^{-t/T_{1b}} q(t) & \tau + \delta t < t \end{cases} \tag{2.9}$$

where $\Delta M(t)$ is the signal difference between tag and control images, M_{0b} is the equilibrium magnetisation of arterial blood, f the blood flow, t the imaging time (measured from the start of tagging), δt the time required for tagged blood to arrive in the imaging slice, τ the tag duration, α the tagging efficiency and T_{1b} the longitudinal relaxation time of arterial blood. $q(t)$ is a correction term which accounts for both the reduction in signal due to outflow of tagged spins from the imaging slice and the difference in T_1 of spins between arterial blood and tissue. See Figure 2.9 for a schematic of how the signal difference ΔM changes over time within a single voxel.

It is the appearance of $(t - \delta t)$ and τ in equation 2.9 that makes quantification of CBF difficult, as values of both δt and τ vary not only between subjects and with different tagging geometries, but also across a single slice according to the exact distribution of blood vessels and flow velocities within the brain. QUIPSS I and II both remove the dependence of ΔM on δt and τ by applying saturation

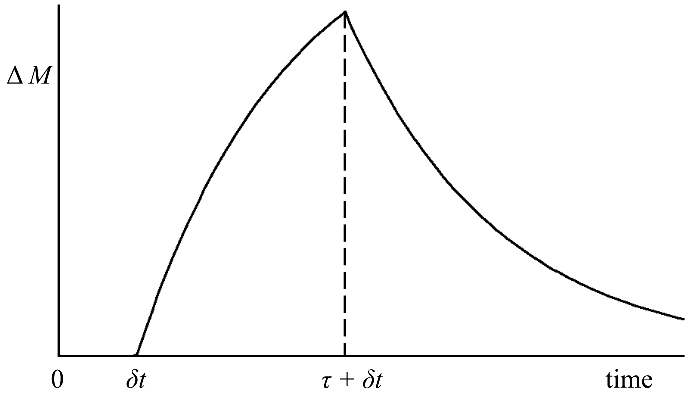

Figure 2.9: The ASL signal, ΔM, over time in an image slice. The tag is applied at time $t = 0$ and reaches the imaging slice at time δt. τ is the duration of the tag. Qualitatively the shape of this graph looks very similar for both pulsed and continuous ASL schemes.

pulses to the imaging slice (QUIPSS I) or the tagging volume (QUIPSS II) at time TI_1, before imaging at time TI_2. Only QUIPSS II can be extended for use with multi-slice imaging, which is why it has found much greater application than its sister method.

By applying a saturation pulse the tag becomes well defined in time. Provided that conditions (i) $\delta t < \mathrm{TI}_1 < \tau$ and (ii) $\mathrm{TI}_1 + \delta t < \mathrm{TI}_2 < \tau + \delta t$ are satisfied, the tagging bolus will have a well-defined time-width of TI_1 and will have completely entered the imaging slice by imaging time TI_2. Then the difference between tag and control signals will be

$$\Delta M(\mathrm{TI}_2) = 2M_{0b} f \mathrm{TI}_1 e^{-\mathrm{TI}_2/T_{1b}} q(\mathrm{TI}_2) \tag{2.10}$$

which is independent of the unknown parameters δt and τ. Thus relative changes in CBF between baseline and activated states can be immediately quantified without the assumption of equal delay times between the two states.

2.2.2.3 Pseudo-Continuous ASL

Pseudo-Continuous ASL (PCASL) combines the advantages of pulsed and continuous ASL by applying a string of many short pulses, each around 1 ms in duration [21]. From the reference frame of a proton spin these pulses appear continuous, as the relaxation rate of blood is much slower than the frequency of the applied pulses, resulting in a very similar trajectory of magnetisation between CASL and PCASL schemes [22]. The most significant benefits of using the PCASL method are that it can be easily implemented on standard clinical scanners, SNR is increased compared to PASL techniques and the stronger gradients played out during RF pulses greatly reduce magnetisation transfer effects compared to CASL. A disadvantage of PCASL is that any resonance offsets will affect the tagging efficiency (in CASL they cause a slight spatial shift of the tagging plane, which is not significant for the majority of planes).

2.2.2.4 Velocity-Selective ASL

Velocity-Selective ASL (VSASL) tags blood which is flowing at or above a chosen cutoff velocity (V_c) and acquires signal from blood flowing below V_c, imaging only that blood which has decelerated through V_c during the image preparation time [23]. Control images are acquired without applying the initial $V > V_c$ tag, but again only blood with $V < V_c$ is imaged. Total VSASL signal is proportional to CBF, and as only arterial blood decelerates significantly through the increasingly branched vasculature tree, the method is sensitive primarily to arterial blood.

A major advantage of VSASL over conventional ASL is that the signal is generated and imaged in the same location. This makes it suitable for imaging pathologically slow or collateral CBF, as it is not necessary to wait for labelled spins to travel into the labelling plane. It can also easily provide whole-brain coverage with consistent sensitivity to perfusion signal. However, the sequences used will inevitably introduce a certain amount of diffusion weighting, which can lead to artefacts, and the cutoff velocity V_c must be carefully chosen to truly measure perfusion [23]. Because only a subset of blood spins are tagged, the SNR is even further reduced compared to other ASL techniques.

2.2.2.5 Background Suppression

The addition of saturation and/or inversion pulses to suppress background tissue signal has been implemented in all flavours of ASL [24]. The idea is to reduce the signal magnitude from the tissue whilst maintaining the contrast in blood signal between tag and control conditions. In this way the blood signal in the subtracted images should remain the same, but the noise introduced by background signal fluctuations will be reduced, increasing the SNR.

The most common implementation of background suppression is to play out an initial saturation pulse to the imaging volume, followed by one or more inversion pulses, carefully timed such that tissue signal will be zero at the time of imaging. This allows for the suppression of tissue with one T_1 value per inversion pulse, although the tissue signal will only be nulled at a single timepoint; thus, background suppression is most effective for single-shot readouts. The initial saturation of the imaging volume helps to reduce sensitivity to any differences in magnetisation between tag and control conditions.

One caveat with background suppression is that the signal in the unsubtracted timecourse will be more heavily blood-weighted, so that any extracted BOLD contrast will have higher intravascular contributions than is normally the case. In applications where only CBF is of interest, background suppression pulses should always be added to ASL sequences [14]. Even for dual ASL/BOLD experiments, the modest reduction in BOLD signal from background suppression is outweighed by the significant increase in ASL SNR [25].

2.2.3 Simultaneous ASL and BOLD Acquisition

It is often desirable to be able to measure both blood flow (via ASL) and BOLD signal at the same time. Examples of past applications include investigations into aspects of neurovascular coupling [26, 27] and providing inputs into BOLD signal models such as the Davis model (see section 3.3).

Because ASL is a subtraction technique and BOLD is not, it is relatively straightforward to obtain both contrasts from a single set of data by subtracting or averaging consecutive images, respectively. Typically an intermediate echo time of 20–25 ms is chosen for these experiments at 3 T [1, 26, 28], as a compromise between optimal ASL echo time (as short as possible) and optimal BOLD echo time (35 ms at 3 T).

2.2.3.1 Dual Echo

In order to improve the contrast-to-noise ratio (CNR) of both ASL and BOLD data, it is possible to acquire images at two different echo times in quick succession within a single TR. The most common approach is to create two echoes after every excitation, as shown in figure 2.10. This 'dual echo' method has been widely used in calibrated MRI experiments in recent years [2,3]. Although dual echo ASL data benefit from shorter echo times, higher slices will have even longer effective post-label delay times, as the total readout time for each slice is increased compared to the single echo case.

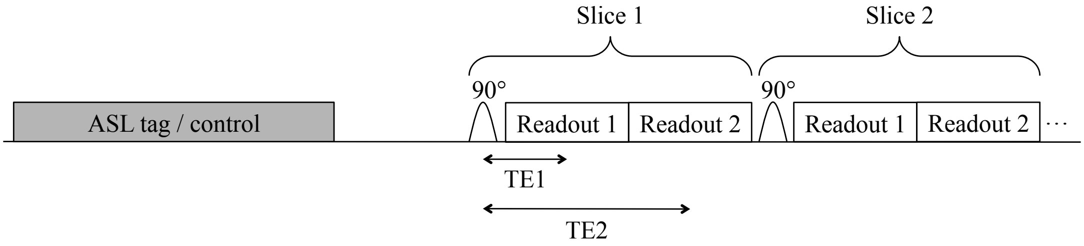

Figure 2.10: Schematic of a dual echo sequence. The ASL tagging period is followed by a delay time, then each slice-selective excitation is followed by two 2D readouts. The first readout, with echo time TE1, is primarily sensitive to ASL; the second, with TE2, is more sensitive to BOLD.

2.2.3.2 Double Excitation

In the 'double excitation' readout, ASL data is acquired first from all slices, then each slice is re-excited for a second readout. A sequence diagram for one TR is shown in figure 2.11. The two echo times can be set completely independently. This method has several advantages compared to the dual echo readout. The ASL data has a higher CNR and is more consistent across the brain, as the slices are acquired at more similar effective post-label delay times. Because all BOLD data is acquired at the very end of the TR, it will contain less ASL tag/control signal contamination. One disadvantage is that the total readout time is increased as the time between excitation and BOLD readout is no longer being used to acquire ASL data, leading to longer scan times or smaller brain coverage. There is also a reduction in BOLD CNR due to the double excitation of each slice, although this can be mitigated by reducing the excitation flip angle from 90° to 60°. It has been shown, both through simulation and experiment, that the double excitation approach significantly increases ASL CNR compared to a dual echo sequence, with only a minimal effect on BOLD CNR [29].

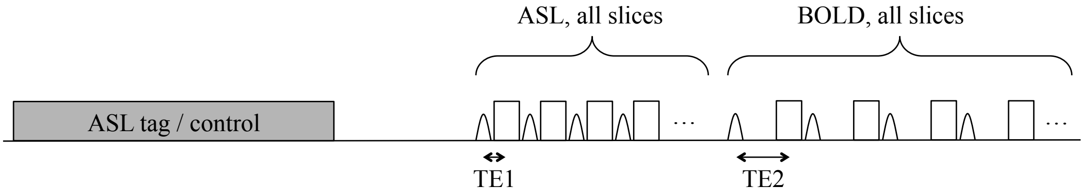

Figure 2.11: Schematic of a double excitation sequence. The ASL tagging period is followed by a delay time, and all slices are read out with a short echo time TE1. Then, each slice is excited for a second time, and BOLD-sensitive images are formed at a later echo time TE2. Flip angles less than 90° are commonly used to preserve signal for the the second excitation.

2.2.4 Diffusion Weighted Imaging

Thermal energy leads to vibrational motion in all particles. When many particles are packed closely together, this motion will result in collisions between them and a ‘random walk’ over time. Diffusion is the macroscopic mixing of particles arising from this motion which was first accurately quantified by Einstein [30], although it had previously been described empirically by many others.

It is the fine structure within the brain that makes diffusion imaging so powerful. When molecules are enclosed by a boundary, such as a cell wall, their motion is restricted. This affects the apparent diffusion coefficient (ADC, or D in equations) defined as $D = \lambda_x^2/2t$ where λ_x is the average distance travelled along the (arbitrarily chosen) x-direction by a molecule in time t. When particles are restricted to a certain volume, this puts an upper limit on the value of λ_x that can be observed, reducing the ADC as compared to the case of ‘free’ or unrestricted diffusion.

Figure 2.12 shows how a simple spin echo sequence can be modified to introduce diffusion weighting. The first additional gradient encodes the position of the spins by altering their phase as a function of position in one dimension. The second gradient reverses this encoding, such that a stationary spin will have acquired no overall phase by the end of the second diffusion gradient. However

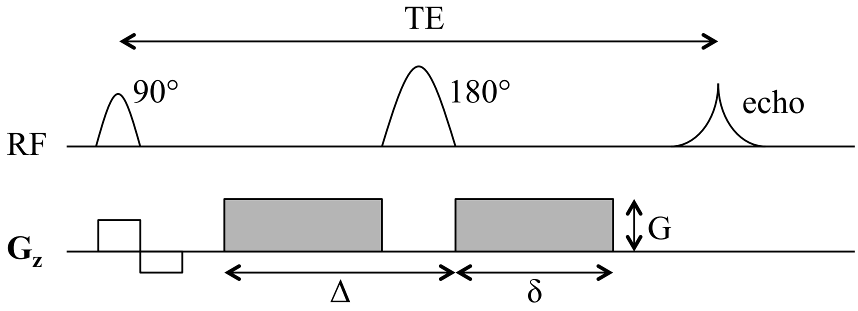

Figure 2.12: Diffusion sensitive pulse sequence. The dark grey gradients added to the basic spin echo sequence encode and decode the position of spins within the sample. G is the amplitude of the gradients, δ their duration and Δ the time between gradient onsets. TE is the echo time.

any spins that have moved during the acquisition will have acquired a non-zero phase, which will act to decrease the overall signal observed at time TE. The magnitude of this signal reduction depends on the ADC and the so-called 'b-value' according to $S = S_0\, e^{-bD}$.

The b-value is defined as $b = \gamma^2 \mathrm{G}^2 \delta^2(\Delta - \delta/3)$, where γ is the gyromagnetic ratio, G is the amplitude of the diffusion gradients, δ is the duration of each diffusion gradient and Δ is the time between the onsets of the first and the second diffusion gradients. Importantly, $b \propto \mathrm{G}^2$, so changing the b-value independently of other parameters (such as T_1 or T_2 weighting) is simple. Then the ADC can be calculated by $D = -\ln(S/S_0)/b$.

2.2.4.1 Intravoxel Incoherent Motion

A diffusion weighted sequence such as that shown in Figure 2.12 is in theory sensitive to any motion within a given voxel, and not exclusively to diffusion, an observation first made by Le Bihan *et al.* [31]. Intravoxel Incoherent Motion (IVIM) falls into two categories: motion due to diffusion and motion due to perfusion. The latter is only present in living tissue and can be considered as incoherent motion due to the microcirculation of blood in the capillary network.

There are approximately 5700 capillaries in each cubic millimetre of the cortex [32], a large enough number that statistical methods may be applied and any directionality of the vessels assumed to average out across a voxel.

An IVIM experiment consists of applying a diffusion weighted sequence with a range of b-values, including very low values less than $\sim$100 s/mm^2. The MR signal will be attenuated by both diffusion and perfusion according to

$$S = S_0 \big\{ (1 - f_v)\, e^{-bD} + f_v\, e^{-bD^*} \big\} \tag{2.11}$$

where the first term describes the regular ADC (D) and the second term quantifies the perfusion contribution by fitting the blood volume fraction (f_v) and the pseudo-diffusion coefficient (D^*). The product of f_v and D^* is closely related to classical perfusion, albeit in different units [33].

3

Metabolic Imaging

The ability to non-invasively image structures inside the human body using x-rays, CT or structural MRI has undoubtedly been one of the greatest advances in medicine of the 20th century. Pathologies that cause structural changes such as bone fractures, cancers and kidney stones to name but a few, are now routinely diagnosed and monitored without the need for risky exploratory surgery.

However, there are also a number of diseases that are more difficult to identify using these traditional imaging techniques. Some cancer tumours including metastases may be small in size but metabolically highly active. These tumours are often very aggressive, diverting blood supplies to fulfil their own needs and expanding rapidly into surrounding tissue, yet they can be difficult to spot on structural medical scans. By creating contrasts that are sensitive to the metabolic rate of glucose or oxygen consumption, certain pathologies become much easier to identify. These methods are also being used to study normal tissue function throughout the body, but especially within the brain which has always been one of the most difficult organs to access and investigate.

This chapter is a review of the methods currently capable of imaging cerebral metabolism. First a brief introduction into the underlying physiology is given, then a range of metabolic imaging techniques are described.

3.1 Physiology

Brain tissue consists primarily of neurons – cells which can receive and transmit information in the form of electrical impulses – and an array of supporting (glial) cells including astrocytes and oligodendrocytes. Neurons connect to one another via dendrites, and transmit information along axons (see figure 3.1).

Neurons use active ion pumps in order to maintain both electrical and concentration gradients between the cell and its surroundings. During neuronal activation a large number of Na^+ ion channels open up leading to a sudden influx in sodium ions into the neuron. This is immediately followed by an ‘action potential’, a wave of depolarisation that propagates along the axon towards a synapse where neurotransmitter chemicals will be released. These in turn diffuse across the gap and bind to receptors on the membrane of another neuron, where they may trigger another action potential, thus further spreading the signal across the brain.

Neuronal signalling itself (the action potential) occurs along concentration gradients and thus does not require any external energy sources. However, energy in the form of adenosine triphosphate (ATP) *is* required to restore the non-equilibrium concentration gradients between the cells and their surroundings. Because the brain does not have a local energy store, ATP must be created in situ to match the energy demand of the neural cells. Briefly, ATP may be generated via either aerobic or anaerobic glycolysis:

$$\begin{array}{lcll} \text{1 glucose} & \rightarrow & \text{2 ATP} & \text{(anaerobic)} \\ \text{1 glucose} + 6\ O_2 & \rightarrow & \text{36 ATP} & \text{(aerobic)} \end{array}$$

where aerobic glycolysis makes use of the Krebs cycle and the electron transport chain in order to produce an additional 34 ATP molecules compared to the anaerobic process [6]. Clearly, aerobic glycolysis is more efficient in the production

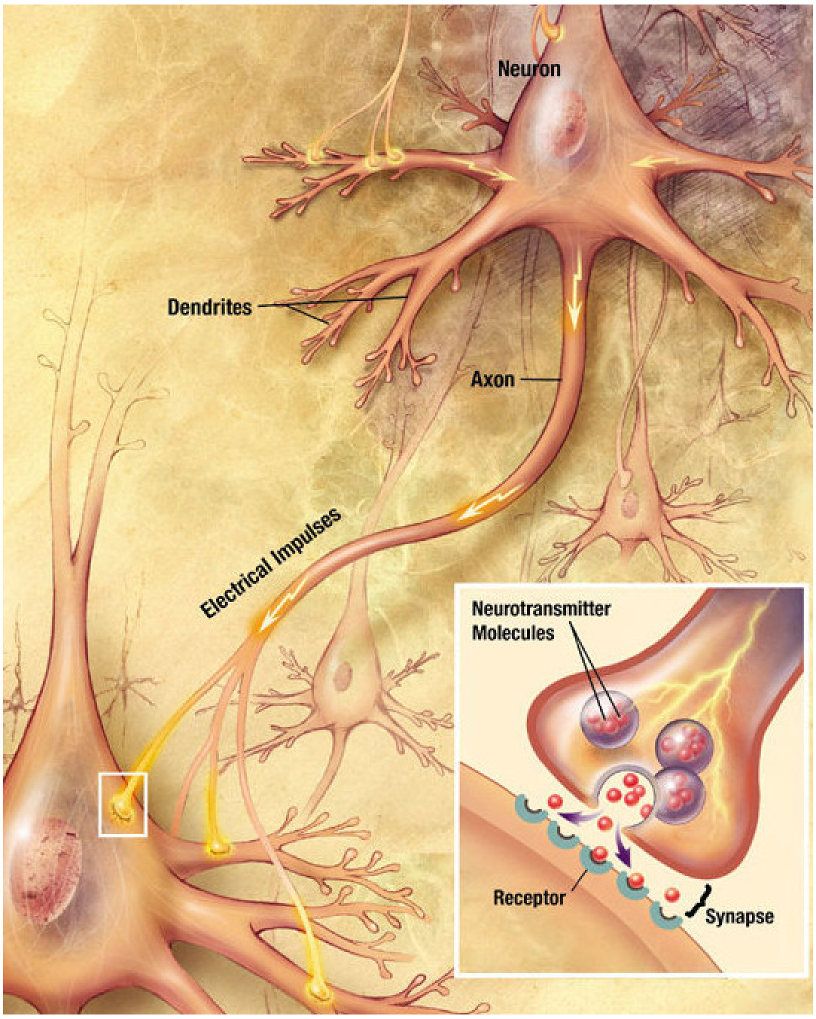

Figure 3.1: Interacting neurons. Neurons typically consist of a cell body (containing cytoplasm, a nucleus and various organelles), one or more axons (capable of transmitting electrical signals between brain regions) and a large number of dendrites. The inset shows a synapse, the junction between two neurons where information is transmitted in the form of chemical diffusion rather than electrical impulses. [34]

of ATP from glucose; however it is also about 100 times slower than anaerobic glycolysis and, of course, requires the necessary supply of oxygen molecules.

By far the majority – an estimated 74% [35] – of metabolic activity in the brain relates directly to the energy demands of neurons following the transmission of electrical signals, with the remainder supporting the surrounding glial cells and maintaining the required levels of proteins and neurotransmitters. Thus the consumption of both glucose and of oxygen are closely associated with the production of ATP and with the rate of signalling between neurons in the brain.

The only source of glucose and oxygen in the brain is the blood supply, hence local blood flow is tightly coupled to metabolic demand. Glucose moves from capillaries into nearby cells via simple diffusion. In the healthy brain, about 10% of glucose is extracted from arterial blood in order to maintain normal function [6].

Oxygen enters the bloodstream via the tiny capillaries lining the lungs, where it binds to haemoglobin molecules, forming oxyhaemoglobin. Haemoglobin has a very high oxygen carrying capacity, about 70 times that of blood plasma. Once the haemoglobin is saturated, further oxygen molecules are dissolved in the plasma, which can immediately diffuse out of thin-walled capillaries into surrounding tissue. As the concentration of dissolved oxygen diminishes and it is replaced with CO_2 (a waste product of aerobic glycolysis), haemoglobin molecules gradually release the oxygen bound to them and in their place may bind CO_2 molecules for transportation. This is known as the Bohr effect, and ensures the efficient transportation and release of oxygen throughout the body. Typical oxygen extraction fractions (OEFs) in the brain are on the order of 40% at rest [36].

3.2 PET

Positron emission tomography (PET) is a form of medical imaging that relies on the use of radioactive tracers. Usually a radioactive isotope is incorporated into a biologically active molecule which is injected into the subject; over time the isotope decays, emitting a slow stream of positrons. Whenever a positron meets an electron they annihilate, producing two gamma rays which may be detected by sensors in the PET scanner.

The intensity and location of the signals depends on the spatial distribution of the active molecule to which the radionuclide has been bound. For example, some compounds are chosen because they are known to remain in the blood stream for a long time; others can be metabolised by tissue, or will bind to the sites of specific pathologies. Ultimately the resolution of the resulting images is limited by several factors including the quality and geometry of the sensing components of the scanner, and the distance travelled by the positrons before annihilation. The latter is a more fundamental limit, and is typically on the order of 1 mm, although it varies with the type of tracer used. Finally, depending on the half-life of the isotope, it may be necessary to inject the tracer an hour or more prior to imaging, in order to allow sufficient time for the tracer to accumulate at the sites of interest.

3.2.1 FDG

The most commonly used PET tracer is fluorodeoxyglucose (FDG), which accounts for upwards of 90% of all PET scans carried out around the world today. It is an analog of glucose, where a hydroxyl group (O-H) has been replaced with radioactive fluorine-18. After injection into the bloodstream, FDG is taken up by cells in the same way as naturally occurring glucose, where it remains until after it has decayed. Therefore, regional FDG uptake in healthy tissue is indicative of the relative glucose consumption and thus of ATP production. In addition, it has been repeatedly demonstrated that malignant tumours have higher rates of anaerobic metabolism than expected, resulting in a higher localised rate of glucose consumption for a given rate of ATP production than in surrounding healthy tissue [37]. For this reason FDG PET is particularly sensitive to both the staging of existing tumours and the identification of metastases throughout the body.

In addition to the favourable metabolic pathways open to FDG, there are also several practical advantages over alternative radiotracers. Fluorine-18 has a half-life of 110 minutes, significantly longer than other beta-emitting isotopes such as carbon-11 (20 minutes), nitrogen-13 (10 minutes) and oxygen-15 (2 minutes) [38]. Its long half-life allows FDG to be produced off-site and delivered to hospital sites on a regular basis, without the requirement for a cyclotron being nearby.

3.2.2 Triple Oxygen

It is also possible to use radioactive oxygen-15 to measure the metabolic rate of oxygen consumption in the brain. However, because oxygen may exist in several forms around the body (primarily as O_2 or H_2O), and oxygen dissolved in blood plasma is only partially extracted during circulation around the brain, the creation of quantitative maps of oxygen metabolism is somewhat more complex than measuring the analogous rate of glucose metabolism using FDG.

A typical PET OEF scan consists of three separate acquisitions [39,40]. First, oxygen-15 is inhaled continuously for approximately 20 minutes. After a steady state between oxygen delivery, cerebral consumption and radioactive decay has been reached, 10 minutes of data are collected for analysis. During the metabolic process, oxygen is converted into water within tissue, so total radioactive decay becomes a function of dissolved oxygen-15 concentration (C^{O_2}) and oxygen-15 labelled water concentration (C^{H_2O}). Mathematically, one may write

$$\begin{aligned} \mathrm{PET} = (\mathrm{CBV} - \mathrm{OEF} \cdot \mathrm{CBV}_v) \int C_{art}^{O_2}(t)\,\mathrm{d}t + \mathrm{CBF} \cdot \int C_{art}^{H_2O}(t) * e^{-kt}\,\mathrm{d}t \\ + \mathrm{CBF} \cdot \mathrm{OEF} \cdot \int C_{art}^{O_2}(t) * e^{-kt}\,\mathrm{d}t \end{aligned} \tag{3.1}$$

where PET is the total decay-corrected activity over the course of the acquisition in counts per 100 g tissue; CBV is the total blood volume; and CBV_v is the deoxygenated (venous) blood volume, estimated as $0.835 \cdot \mathrm{CBV}$ [40]. The subscript *art* refers to the arterial concentrations, $*$ denotes a convolution and k is defined as CBF/λ, where λ is the brain:blood partition coefficient in ml water/100 g tissue.

From equation 3.1 it is possible to calculate OEF, provided all the other terms in the equation are known. The total PET activity is recorded by the scanner and the arterial concentrations may be measured from blood samples taken from an arterial line during the course of the experiment. This leaves CBF and CBV to be determined, both of which may be expected to vary spatially across the brain.

In order to measure CBF, a second 20-minute PET scan is performed using oxygen-15 labelled water as a tracer, injected into the vein of the subject. CBF may be calculated by solving the following equation:

$$\mathrm{PET} = \mathrm{CBF} \cdot \int C_{art}(t) * e^{-kt}\,\mathrm{d}t \tag{3.2}$$

where PET is the local tissue activity recorded by the PET scanner and C_{art} is the measured concentration of the tracer in arterial blood during the acquisition.

Similarly, CBV may be quantified by carrying out a third scan, this time with oxygen-15 labelled carbon monoxide as the tracer. This scan is typically shorter, with 1 minute of inhalation followed by a 5-minute acquisition. As carbon monoxide binds directly to haemoglobin and does not exchange oxygen molecules with the tissue, CBV may be calculated directly from

$$\mathrm{PET} = \mathrm{CBV} \cdot D \cdot \int C_{art}(t)\,\mathrm{d}t \tag{3.3}$$

without any convolution or dependence on CBF. Here D is the density of brain tissue in g/ml, the value of which may be assumed from the literature. Finally, once CBF, CBV and OEF are known, $\mathrm{CMRO_2}$ can be easily calculated as

$$\mathrm{CMRO_2} = \mathrm{OEF} \cdot \mathrm{CBF} \cdot \mathrm{C}_a\mathrm{O}_2 \tag{3.4}$$

where $\mathrm{C}_a\mathrm{O}_2$ is the total oxygen content of arterial blood, a further quantity which may be measured from the blood samples taken during the scan.

This method is capable of providing a wide range of physiological and metabolic information with a relatively small number of assumptions. However, because oxygen-15 has a half life of only 123 s [38], the existence of an on-site medical cyclotron is a prerequisite to the procedure. Very few centres have both the facilities and the staff expertise to carry out these scans.

An additional disadvantage is that each examination requires three separate scans with a significant total radiation dose, limiting the number of repeat scans that may be carried out. Whilst this tends not to be a problem for clinical populations, it does place a limit on what can be investigated in a research environment, including the potential for long-term investigations into metabolic changes during healthy ageing versus conditions such as dementia.

3.3 MRI

As discussed in section 2.2.1, the BOLD response is strongly dependent on physiological parameters such as CBF, CBV and $CMRO_2$, and thus contains information which is of great clinical interest. However, the brain's fine control over haemodynamic responses may be impaired in certain diseased states, disrupting the balance of physiological responses and sometimes even leading to decreased BOLD signals upon activation [41]. It is currently not possible to reliably differentiate between underlying causes for abnormal BOLD signals - for example, an unusually low signal change in response to a stimulus could be due to decreased neuronal activation, impaired vascular reactivity, a lack of fresh oxygenated blood at the site of activation, or a lowered rate of oxidative metabolism, each of which may point to a different specific pathology with distinct recommended treatment plans.

One promising method for the quantification of physiological parameters is that of gas-calibrated BOLD imaging, which uses increased concentrations of carbon dioxide (CO_2) [42] or of oxygen [43] to induce changes in CBF, CBV, OEF and BOLD signal without an accompanying change in $CMRO_2$ [44, 45]. This allows for the calculation of a calibration parameter specific to the subject and scanning session which can then be used to infer relative changes in $CMRO_2$ during a functional task. Recently the hyperoxic and hypercapnic regimes have been combined within a single session to allow for the calculation of baseline values for oxygen consumption and OEF, as well as baseline CBF, CBV and arterial arrival time [1, 2]. This method is capable of measuring voxelwise absolute physiological parameters, information which until recently was only obtainable using PET scans.

3.3.1 The Davis Model

The BOLD signal changes with the transverse relaxation rate, R_2^*, according to

$$\frac{\Delta\mathrm{BOLD}}{\mathrm{BOLD}_0} = e^{-\mathrm{TE}\cdot\Delta R_2^*} - 1 \approx -\mathrm{TE}\cdot\Delta R_2^* \tag{3.5}$$

for small changes in relaxivity. R_2^* is defined as $1/T_2^*$ and is related to blood volume and the concentration of dHb in venous blood, $[\mathrm{dHb}]_v$, by

$$R_2^* = A\cdot\mathrm{CBV}\cdot[\mathrm{dHb}]_v^\beta \tag{3.6}$$

where A is a proportionality constant (dependent on field strength and sample properties) [46]. β is a fitting parameter that is approximately 1 for large vessels and 2 for capillaries.

Substituting equation 3.6 into equation 3.5 gives

$$\frac{\Delta\mathrm{BOLD}}{\mathrm{BOLD}_0} = M\left\{1 - \left(\frac{\mathrm{CBV}}{\mathrm{CBV}_0}\right)\left(\frac{[\mathrm{dHb}]_v}{[\mathrm{dHb}]_{v0}}\right)^\beta\right\} \tag{3.7}$$

where M has been defined as $A\cdot\mathrm{TE}\cdot\mathrm{CBV}_0\cdot[\mathrm{dHb}]_{v0}^\beta$ and represents the maximum increase in BOLD signal that could theoretically be achieved if all dHb were removed from the vasculature. Subscripts of 0 refer to a baseline, normocapnic state.

From Fick's principle of conservation it can be shown that when the arterial concentration of dHb is negligible, the steady state venous dHb concentration is given by

$$[\mathrm{dHb}]_v = \frac{1}{4}\frac{\mathrm{CMRO}_2}{\mathrm{CBF}} \tag{3.8}$$

where the factor of 4 indicates that each molecule of haemoglobin can carry 4 molecules of O_2 [47]. It has also been shown that there is a tight coupling between blood flow and volume changes, allowing us to rewrite CBV in terms of the more easily measured CBF:

$$\left(\frac{\mathrm{CBV}}{\mathrm{CBV}_0}\right) = \left(\frac{\mathrm{CBF}}{\mathrm{CBF}_0}\right)^{\alpha}. \tag{3.9}$$

The Grubb coefficient α was originally measured as 0.38 [48]. This value was obtained from the total blood pool in anaesthetised monkeys and can at best be expected to hold for healthy adults, limiting the applicability of this method within the general population. As the BOLD signal is limited largely to venous blood with significant dHb content, this value is likely an over-estimate when used within the calibrated BOLD framework. More recent work by Chen and Pike using MR methods have quantified α as 0.23 during neuronal activation [49] and 0.18 during CO_2 modulation [50], both of which are significantly lower than the classical value.

Substituting equations 3.8 and 3.9 into equation 3.7 yields the final expression of the Davis model [42]

$$\frac{\Delta\mathrm{BOLD}}{\mathrm{BOLD}_0} = M\left\{1 - \left(\frac{\mathrm{CMRO}_2}{\mathrm{CMRO}_2|_0}\right)^{\beta}\left(\frac{\mathrm{CBF}}{\mathrm{CBF}_0}\right)^{\alpha-\beta}\right\}. \tag{3.10}$$

By first exposing the subject to a stimulus which induces a change in blood flow without a concomitant change in oxygen metabolism, such as mild hypercapnia, it is possible to ‘calibrate’ an experiment by calculating a value of M which will be specific to the subject and the particular scanning session. This M value can then be used with subsequent time courses for the BOLD and ASL signals in order to quantify the relative change in CMRO_2 induced by a cognitive task.

3.3.2 The Hyperoxia Model

Chiarelli *et al.* developed an alternative calibrated BOLD methodology which uses hyperoxia instead of hypercapnia to calculate M [43]. Advantages of using oxygen are that it is more easily tolerated, especially within the patient population, and is more widely available in a clinical setting. Whereas a hypercapnic stimulus increases venous oxygenation by inducing an increase in CBF, hyperoxia acts directly to increase arterial and venous oxygen saturation, which in turn decrease $[\mathrm{dHb}]_v$.

Because hyperoxia can have a mild vasoconstrictive effect (primarily through hyperventilation driving down the $\mathrm{P}_a\mathrm{CO}_2$), it is necessary to adapt equation 3.7 to include contributions to the total venous dHb concentration $[\mathrm{dHb}]_v^{total}$ arising directly from the increased arterial oxygen saturation $[\mathrm{dHb}]_v^{ho}$ and from any changes in blood flow $\Delta[\mathrm{dHb}]_v^{flow}$:

$$\frac{\Delta\mathrm{BOLD}}{\mathrm{BOLD}_0} = M\left\{1 - \left(\frac{\mathrm{CBV}}{\mathrm{CBV}_0}\right)\left(\frac{[\mathrm{dHb}]_v^{ho}}{[\mathrm{dHb}]_{v0}} + \frac{\Delta[\mathrm{dHb}]_v^{flow}}{[\mathrm{dHb}]_{v0}}\right)^{\beta}\right\}. \tag{3.11}$$

Equation 3.9 is still valid, as is equation 3.8 when $[\mathrm{dHb}]_v$ is replaced with $[\mathrm{dHb}]_{v0} + \Delta[\mathrm{dHb}]_v^{flow}$ (describing only the change in venous dHb induced by variations in blood flow). This leads to

$$\frac{\Delta\mathrm{BOLD}}{\mathrm{BOLD}_0} = M\left\{1 - \left(\frac{\mathrm{CBF}}{\mathrm{CBF}_0}\right)^{\alpha}\left(\frac{[\mathrm{dHb}]_v^{ho}}{[\mathrm{dHb}]_{v0}} + \frac{\mathrm{CBF}_0}{\mathrm{CBF}} - 1\right)^{\beta}\right\}, \tag{3.12}$$

the full equation describing change in BOLD signal to a hyperoxic stimulus. The ratio $[\mathrm{dHb}]_v^{ho}/[\mathrm{dHb}]_{v0}$ may be calculated from measurements of end-tidal oxygen monitoring during the experiment (see figure 3.2 for details).

$$\begin{array}{lll}
\mathrm{F_{ET}O_2} & & \\
\downarrow & \mathrm{P}_a\mathrm{O_2} = \mathrm{F_{ET}O_2}\cdot\mathrm{P_{atm}} - \mathrm{P_{A-a}} & \\
\mathrm{P}_a\mathrm{O_2} & & \\
\downarrow & \mathrm{S}_a\mathrm{O_2} = \left[\dfrac{23400}{(\mathrm{P}_a\mathrm{O_2})^3 + 150\cdot\mathrm{P}_a\mathrm{O_2}} + 1\right]^{-1} & \text{Severinghaus equation} \\
\mathrm{S}_a\mathrm{O_2} & & \\
\downarrow & \mathrm{C}_a\mathrm{O_2} = \phi[\mathrm{Hb}]\mathrm{S}_a\mathrm{O_2} + \varepsilon\cdot\mathrm{P}_a\mathrm{O_2} & \\
\mathrm{C}_a\mathrm{O_2} & & \\
\downarrow & \mathrm{C}_v\mathrm{O_2} = \mathrm{C}_a\mathrm{O_2} - \mathrm{OEF_0}\cdot\dfrac{\mathrm{CBF_0}}{\mathrm{CBF}}\cdot\mathrm{C}_a\mathrm{O_2}|_0 & \star \\
\mathrm{C}_v\mathrm{O_2} & & \\
\downarrow & \mathrm{S}_v\mathrm{O_2} = \dfrac{\mathrm{C}_v\mathrm{O_2} - \varepsilon\cdot\mathrm{P}_v\mathrm{O_2}}{\phi[\mathrm{Hb}]} \quad \text{where} \quad \mathrm{P}_v\mathrm{O_2} \approx 0 & \\
\mathrm{S}_v\mathrm{O_2} & & \\
\downarrow & [\mathrm{dHb}]_v = (1 - \mathrm{S}_v\mathrm{O_2})[\mathrm{Hb}] & \\
[\mathrm{dHb}]_v & &
\end{array}$$

Figure 3.2: The sequence of steps by which an end-tidal measurement of the oxygen fraction ($F_{ET}O_2$) may be used to calculate the arterial partial pressure of oxygen (P_aO_2), arterial oxygen saturation (S_aO_2), arterial oxygen content (C_aO_2), venous oxygen content (C_vO_2) and finally the venous deoxygenated haemoglobin concentration ($[dHb]_v$). Atmospheric pressure (P_{atm}) may be measured or assumed and the arterial–alveolar pressure gradient (P_{A-a}) may be estimated from the age of the subject [51]. Other constants represent the oxygen carrying capacity of haemoglobin (ϕ = 1.34 ml O_2/g_{Hb}), the solubility coefficient of oxygen in blood (ε = 0.0031 ml O_2/dl_{blood}/mmHg) and the blood haemoglobin concentration ([Hb], which may be measured from a blood sample). The partial pressure of oxygen in venous blood plasma (P_vO_2) is assumed to be negligible, even during hypercapnia, as all oxygen is bound within red blood cells. The step marked with a $\star$ is derived from the assumption of constant $CMRO_2$ during normoxic and hyperoxic states (see equation 3.14), and requires the additional assumption of a typical value for baseline oxygen extraction fraction (OEF_0). Chiarelli *et al.* [43] assumed an OEF_0 of 0.3 for healthy young adults, and neglected the small change in flow induced by hyperoxia, simplifying this expression to $C_vO_2 = C_aO_2 - 0.3 \cdot C_aO_2|_0$.

3.3.3 Dual-Gas Calibration

To summarise: we now have two expressions (see equations 3.10 and 3.12), valid under hypercapnic and hyperoxic regimes respectively, which describe the BOLD signal change as a function of CBF, $\mathrm{CMRO_2}$, $[\mathrm{dHb}]_v$ and the maximal BOLD signal change M. In order to estimate M using hyperoxia it is necessary to assume a value for resting OEF; conversely, if M were known *a priori*, it would be possible to use equation 3.12 to determine OEF. By making use of the fact that the calibration parameter M appearing in equations 3.10 and 3.12 should be identical, one can apply both hypercapnic and hyperoxic stimuli in a single scan session in order to calculate a value of OEF on a voxelwise basis.

The Oxford Model

The simplest means of combining the two basic models is to first carry out a hypercapnia experiment (where $\mathrm{CMRO_2}$ is assumed to remain constant) to determine M, and then expose the subject to hyperoxia in order to calculate the $[\mathrm{dHb}]_v$ ratio (hyperoxic/normoxic) from which a value for the OEF can be calculated [1].

Referring to figure 3.2 and substituting the equation $\star$ into the expressions for $\mathrm{S_vO_2}$ and $[\mathrm{dHb}]_v^{ho}$ we obtain the following expression for $\mathrm{OEF_0}$:

$$\mathrm{OEF_0} = \left\{ \frac{\phi[\mathrm{Hb}]}{\mathrm{C_aO_2}|_0} \left(\frac{[\mathrm{dHb}]_v^{ho}}{[\mathrm{dHb}]_{v0}} - 1 \right) + \frac{\mathrm{C_aO_2}}{\mathrm{C_aO_2}|_0} - \frac{[\mathrm{dHb}]_v^{ho}}{[\mathrm{dHb}]_{v0}} \right\} \left(1 - \frac{[\mathrm{dHb}]_v^{ho}}{[\mathrm{dHb}]_{v0}} \right)^{-1} \tag{3.13}$$

where no flow change to hyperoxia has been assumed, $[\mathrm{dHb}]_v^{ho}/[\mathrm{dHb}]_{v0}$ can be calculated from equation 3.12 and $\mathrm{C_aO_2}$ at normoxia and hyperoxia can be determined directly from measurements of the oxygen content of expired gases.

It is then possible to calculate the resting $\mathrm{CMRO_2}$ via

$$\mathrm{CMRO_2} = \mathrm{OEF_0} \cdot \mathrm{CBF_0} \cdot \mathrm{C_aO_2}|_0 \tag{3.14}$$

which may be done on a voxelwise basis to create fully quantitative maps of resting oxygen metabolism. This describes the analysis approach that was used throughout this thesis.

The Montreal Model

Using the same principles as the Oxford model, this version has two subtle differences. Firstly, the Davis and Chiarelli models are combined into a single ‘generalised calibration model’ which takes into account potentially concomitant changes in $\mathrm{P_aO_2}$ and CBF [52]. Thus equation 3.13 becomes

$$\mathrm{OEF_0} = \left\{ \frac{\phi[\mathrm{Hb}]}{\mathrm{C_aO_2}|_0} \left(\frac{[\mathrm{dHb}]_v^{ho}}{[\mathrm{dHb}]_{v0}} - 1 \right) + \frac{\mathrm{C_aO_2}}{\mathrm{C_aO_2}|_0} - \frac{[\mathrm{dHb}]_v^{ho}}{[\mathrm{dHb}]_{v0}} \right\} \left(\frac{\mathrm{CBF_0}}{\mathrm{CBF}} - \frac{[\mathrm{dHb}]_v^{ho}}{[\mathrm{dHb}]_{v0}} \right)^{-1} . \tag{3.15}$$

This model can be applied to simultaneous modulations of oxygen and $\mathrm{CO_2}$, such as using carbogen gas (5–10% $\mathrm{CO_2}$ with balance oxygen) as a stimulus. It has been suggested that carbogen produces more reliable M values than pure hypercapnic or hyperoxic stimuli [52], although it is also associated with lower subject tolerability.

The second difference between the Oxford and the Montreal approaches is that the latter solves for M and $\mathrm{OEF_0}$ simultaneously following two or more distinct respiratory manipulations [2]. This acts to reduce the accumulation of errors in the OEF estimate.

The Cardiff Model

Wise *et al.* applied the generalised calibration model to a more complex respiratory design, in which step changes in $P_{ET}O_2$ and $P_{ET}CO_2$ were overlaid and a Bayesian analysis method was used [3]. This further allowed $(\alpha - \beta)$ to be estimated directly from the data, reducing the number of assumed variables by one.

3.4 NIRS

Near-infrared spectroscopy (NIRS) makes use of the differing optical properties of oxygenated and deoxygenated haemoglobin (oxy-Hb and dHb, respectively) to measure relative changes in the volume or oxygenation of blood. The absorption spectra of oxy-Hb and dHb diverge at approximately 550 nm and then cross at 810 nm, in the middle of the near-infrared (NIR) range, as shown in figure 3.3. By applying two wavelengths of incident light, one above and one below 810 nm, it is possible to determine the relative volumes of oxy-Hb and dHb close to the sensor.

NIRS devices are relatively small, cheap and portable, certainly compared to the medical scanners which have been discussed above. Clinically they have been applied to monitor tissue oxygenation during surgical interventions [53, 54] and in the days following intracranial haemorrhage [55, 56]. In both cases clinicians are looking only for relative changes in NIRS signals over time.

In the research setting, functional NIRS is a growing field [57]. The emergence of wireless devices and the lack of any ionising radiation are both advantages over traditional brain scanners. Disadvantages of NIRS are that the signals can only penetrate approximately 4 cm into the brain, providing limited coverage, and that it is difficult to make the method truly quantitative as the absorption and geometric properties of intermediate tissues like skin, hair and bone would have to be measured and carefully corrected for.

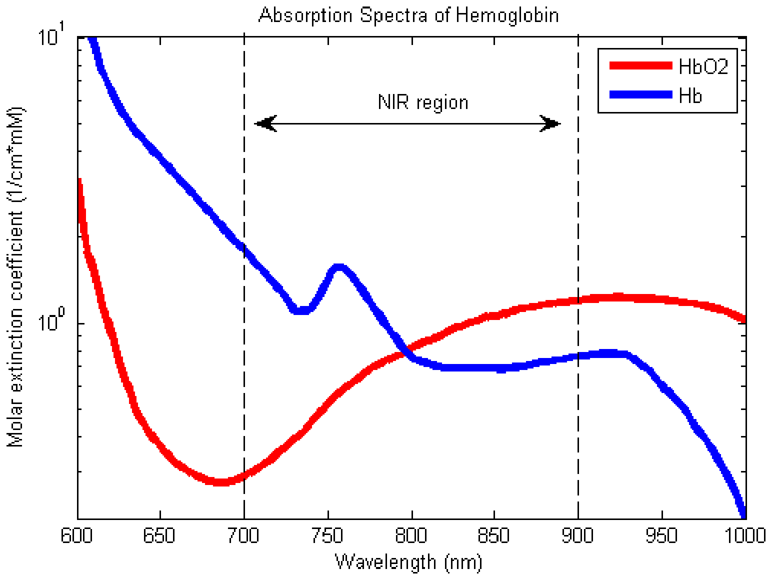

Figure 3.3: Graph showing the absorption spectra of oxygenated (red) and deoxygenated (blue) haemoglobin as a function of wavelength. [58]

4

Field Dependence of the Davis Model

4.1 Introduction

Gas-calibrated functional MRI (fMRI) has emerged as a promising tool to non-invasively measure stimulus-evoked changes in $CMRO_2$ [42,59]. Not only is this more directly physiologically relevant than measuring only the BOLD signal, but it has also been shown to be more consistent between subjects and between scanning sessions [60].

Calibrated fMRI relies on a simple model of the BOLD signal known as the Davis model [42]. This was originally applied at a field strength of 1.5 T, but has benefitted greatly from the SNR improvements brought by the transition to 3 T scanners in recent years. Now, with the emergence of 7 T research systems, there is an interest in extending the method to even higher field strengths. It is obvious that as a physiological parameter $CMRO_2$ should not be affected by the field strength at which it is measured. However, what is less clear is how the translation to different field strengths may affect the accuracy of the underlying Davis model.

Simulations of the calibrated fMRI experiment suggest that the method is feasible at all three field strengths, so long as the Davis model parameters are adjusted to reflect the altered BOLD sensitivity [61, 62]. It has also been predicted that systematic error may be increased at 7 T compared with lower field strengths [62]. Experimental confirmation of these findings has so far not been performed.

The aim of this study was to carry out a direct comparison of the hypercapnia-calibrated fMRI method at 1.5, 3 and 7 T, in order to test the level of agreement in the measured estimates of relative $\mathrm{CMRO_2}$ across field strengths. Detailed simulations of the BOLD signal were performed to predict general trends in the calibration parameter M across field strengths, and to provide a basis for interpreting the experimental results. Implicitly this study was also an investigation into the robustness of the Davis model itself, and how well it translates across field strengths.

4.2 Theory

The Davis model (equation 4.1) describes the extravascular BOLD signal as a function of changes in CBF and $\mathrm{CMRO_2}$ [42,59]. Changes in CBF are related to changes in CBV via the Grubb exponent α [48]. This physiological interpretation of α was retained and was therefore set independent of field strength as 0.2 [44, 49]. The BOLD signal is related to underlying changes in susceptibility via the exponent β, which varies with vessel size and also with field strength.

$$\frac{\Delta\mathrm{BOLD}}{\mathrm{BOLD_0}} = M\left\{1 - \left(\frac{\mathrm{CMRO_2}}{\mathrm{CMRO_2}|_0}\right)^{\beta}\left(\frac{\mathrm{CBF}}{\mathrm{CBF_0}}\right)^{\alpha-\beta}\right\} \tag{4.1}$$

The calibration parameter M is defined as $A{\cdot}\mathrm{TE}{\cdot}\mathrm{CBV_0}{\cdot}[\mathrm{dHb}]_{v0}^{\beta}$ or, equivalently, as the maximum theoretically possible BOLD signal change. Because this is expected to vary with tissue type, physiology and local field, it is necessary to measure M during each scan session. This is most commonly achieved by applying an isometabolic stimulus, such as mild hypercapnia, during which CMRO_2 is assumed to remain constant (see section 3.3.1).

The definition of M also describes a dependence on the BOLD echo time. Since many different values of TE have been used throughout the literature it is often instructive to be able to scale the calibration parameter to the optimal BOLD echo time for each field strength, which in this study were considered to be 50/35/25 ms at 1.5/3/7 T, respectively [63]. To do this A was assumed to have no dependence on TE, and the experimentally acquired M was multiplied by the ratio (optimal TE/actual TE).

4.3 Methods

4.3.1 BOLD Signal Simulations

A detailed BOLD signal model [64] was used to simulate the calibrated BOLD experiments in order to investigate both the general trends and the specific effects of physiology on M values at the three field strengths. In order to extend the original model to 1.5 and 7 T, some small modifications were made. Due to the limited relaxometry literature performed to date at 7 T, it was not possible to describe R_2^* as a function of haematocrit. Thus the empirical measurements of blood R_2^* at 3 T as a function of oxygenation and haematocrit [65] were replaced with the results of a multi-field relaxometry experiment with fixed haematocrit [66]. The quadratic dependence of R_2^* on oxygenation was retained, i.e. $R_2^* = C_1 + C_2(1-Y)^2$, where C_1 and C_2 are field strength specific constants and Y is the fractional blood oxygenation.

For the simulations, an ideal physiology was assumed with a haematocrit of 0.44 [67] and a resting OEF of 0.4 [36]. Hypercapnia was simulated as a 30% increase in CBF with no change in $CMRO_2$. A range of resting total CBV values were considered (0.03, 0.05 and 0.07) corresponding to the population mean ± 2 standard deviations as measured by Perlmutter *et al.* [68]. BOLD signals were simulated at the experimental echo times of 50/17/17 ms for 1.5/3/7 T, and then linearly scaled to the field-optimised values for comparison purposes.

4.3.2 MRI Parameters

Subjects were scanned on 1.5 T Avanto, 3 T Verio and 7 T systems (Siemens Healthcare, Erlangen, Germany) with 12-channel (1.5 T) and 32-channel (3 and 7 T) head coils. Scans were carried out on separate days to minimise the effects of fatigue and habituation. Because specific absorption rate (SAR) was anticipated to be a limiting factor on sequence design at 7 T, a pulsed (rather than pseudo-continuous) ASL sequence was implemented to measure CBF [14]. Flow-sensitive alternating inversion recovery (FAIR) was chosen to minimise the effects of B_1 inhomogeneity [18], and the QUIPSS II scheme was used to improve quantification of perfusion.

A single echo at 17 ms provided sufficient signal-to-noise ratio (SNR) for both CBF and BOLD analysis at 3 and 7 T. A dual echo version of the same sequence was implemented at 1.5 T with echoes at 17 and 50 ms to ensure sufficient BOLD contrast. All other imaging parameters were kept constant across scanners. Six slices were acquired (limited by SAR at 7 T) with an EPI readout and were placed axially to cover the motor cortex. For consistency across scanners, no acceleration methods (such as parallel imaging or partial Fourier) were used. Bandwidth was set to 3004 Hz/Px, inversion times were TI_1 = 700 ms and TI_2 = 1800 ms, and repetition time was 3 s. Note that in pulsed ASL the bolus duration is fixed by TI_1 and the effective post-labelling delay (PLD) is given by $TI_2 - TI_1$ [14], so 1100 ms in this experiment. It is common to use shorter PLDs in pulsed ASL compared to (pseudo-)continuous implementations to compensate for the reduced SNR inherent in pulsed ASL. Although this may result in incomplete delivery of tagged blood to the imaging slices, it is also more suited to gas-calibrated experiments, where arterial arrival times are shortened during hypercapnia. Voxel size was $4.1 \times 4.1 \times 5.0$ mm^3 with a 1 mm slice gap in order that the SNR of ASL data at 1.5 T did not become prohibitively low. FAIR labelling used a 60 mm selective and a 260 mm non-selective slab at all field strengths.

4.3.3 Functional and Respiratory Tasks

A bilateral finger tapping motor task was chosen to easily allow a consistent implementation across scanner suites. Subjects were given audio cues over the intercom systems and were instructed to perform 4 blocks of self-paced finger tapping (48 s ON, 48 s OFF). This was followed by 2 blocks of hypercapnia (3 min duration, each followed by 2 mins of air), as shown in figure 4.1. Subjects were instructed to perform the motor task at a fast but comfortable rate, and these instructions were repeated prior to each scan session. Performance of the task was monitored from the control room and all subjects were observed to fully cooperate.

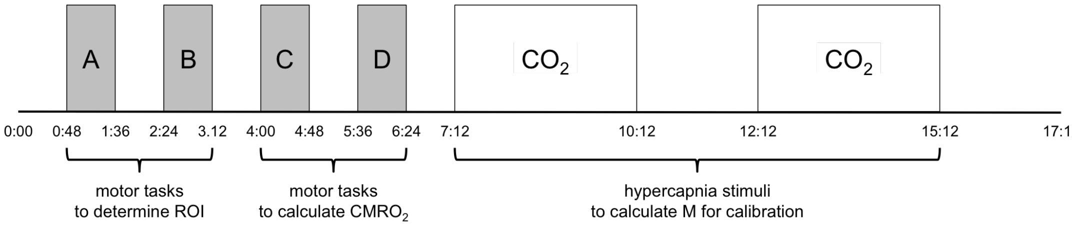

Figure 4.1: Diagram showing timing of stimuli.

Gas delivery and sampling was achieved through a nasal cannula (dual Nare, Flexicare, Mountain Ash, UK) in conjunction with a CO_2 gas analyser (CO2 100C Biopac Systems, Goleta, CA, USA). A 10% CO_2/21% O_2 gas mixture with balance nitrogen was delivered, which mixed with room air at a ratio of approximately 1:1, resulting in a 5% CO_2 stimulus. In order to minimise subject awareness of the hypercapnia stimulus, medical air (21% O_2 with balance nitrogen) was delivered during periods of air breathing, including during the motor tasks.

4.3.4 Data Analysis

Data were analysed using the FMRIB Software Library (FSL) and the fMRI Expert Analysis Tool (FEAT) [69]. Preprocessing consisted of motion correction [70], brain extraction [71] and fieldmap correction [72]. Highpass filters of 10 and 300 s were applied to ASL and BOLD timecourses respectively, and no spatial smoothing was applied. The following contrasts were input as part of a general linear model within FEAT: (1) tag-control signal, modelled as a square on/off shape, which describes baseline perfusion; (2) BOLD response to motor tasks A+B, with a haemodynamic response function modelled as a gamma convolution with mean lag 6 s, standard deviation 3 s; (3) BOLD response to motor tasks C+D, as above; (4) BOLD response to hypercapnia, modelled with a gamma convolution with mean lag 42 s, standard deviation 30 s to account for the delay between switching to the CO_2 mixture and the cerebrovascular response to increased arterial partial pressure of CO_2 in the brain; (5-7) blood flow responses to motor tasks A+B, C+D and hypercapnia, modelled as interactions between contrasts (1) and the three BOLD responses, respectively. In this context, the term ‘interaction’ refers to the fitting of the product of two existing contrasts, and may be modelled in FEAT simply by checking the relevant tick box. To avoid circular analysis [73], data from motor tasks A+B were used to create a region of interest (ROI), and only data acquired during motor tasks C+D were analysed to quantify response to motor stimuli (see figure 4.1). Other combinations of block-wise analysis were investigated (e.g. A+D for ROI definition, B+C for data analysis), and this choice was found to have no impact on the results.

Two methods were used to create motor ROIs. First, a ‘BOLD only’ ROI was defined as the 40% of brain voxels with the highest uncorrected voxel-wise z-stats in response to motor tasks (A+B only, see figure 4.1). This cutoff was used in place of setting a z-stat threshold directly as it was more consistent between subjects and particularly across field strengths. Similarly, a grey matter (GM) mask was created from the 40% of brain voxels with the most significant baseline tag-control signal difference. Multiplication of the BOLD ROI and GM mask produced a ‘BOLD/GM’ motor ROI. The creation of ‘CBF only’ and ‘BOLD/CBF overlap’ ROIs was not possible due to the low SNR of ASL data, particularly at 1.5 T.

Further analysis was performed on coefficient of parameter estimate (COPE) outputs of the FEAT analysis in MATLAB (MathWorks, Natick, MA, USA), which represent the estimated effect sizes of each of the contrasts described above. BOLD signal responses were normalised with respect to the mean signal over the entire timecourse, and CBF responses were normalised to the baseline perfusion signal, as output by the tag-control COPE. Voxels with a BOLD response to either motor or hypercapnia stimuli < 0 or > 0.10, or a CBF response < 1 (no change) or > 3 (+200% relative to baseline), were assumed to be noise or to contain significant fractions of white matter or cerebrospinal fluid, and were excluded from further analysis. Mean values within the remaining voxels for BOLD and CBF responses to motor tasks (C+D) and to hypercapnia were used to calculate M and relative $CMRO_2$ on a per subject basis, according to equation 4.1, with the assumption that mild hypercapnia does not alter $CMRO_2$. The Grubb exponent α was set at 0.2 for all field strengths [44,49], and β values of 1.5/1.3/1.0 were used at 1.5/3/7 T respectively [42,74,75]. Finally, M values at 3 and 7 T were scaled to optimal echo times for comparison purposes.

Relative changes in $CMRO_2$ induced by the motor tasks were compared across field strengths using the one sample paired t-test, where the null hypothesis that measured $CMRO_2$ changes are independent of field strength was rejected if $p < 0.05$. Bland-Altman diagrams were used to investigate any systematic biases between field strengths. ASL image SNR was calculated from a single resting tag-control subtracted timepoint, as the mean ASL signal within the BOLD/GM ROI divided by the standard deviation in a non-brain ROI. In order to avoid unfair bias, noisy voxels were not excluded from the BOLD/GM ROI for this calculation.

4.4 Results

4.4.1 BOLD Signal Simulations

Simulations of hypercapnia calibration using a CBV of 0.05 and the actual experimental TEs used predicted M values of 0.085 at 1.5 T, 0.076 at 3 T and 0.191 at 7 T. When scaled to the optimal TE values, M was predicted to be 0.085 at 1.5 T, 0.156 at 3 T and 0.281 at 7 T. These optimal values are plotted in figure 4.2 as crosses; circles and triangles represent the predicted M values for ± 2 standard deviations for physiological CBV values respectively. The simulations predict that variation in resting CBV leads to a greater range of M values at higher magnetic field strengths. Similar increases in the range of M values with field strength were observed when the range of baseline total OEF

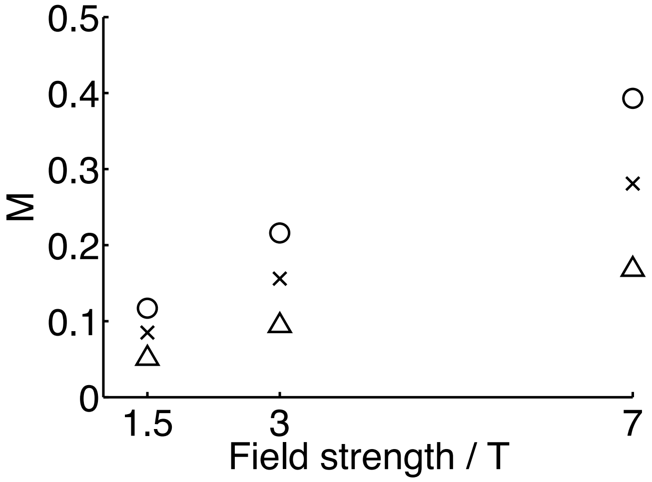

Figure 4.2: Simulated M values produced using the detailed BOLD signal model. Triangles, crosses and circles represent the predicted M values for individuals with a blood volume fraction of 0.03, 0.05 and 0.07 respectively.

was investigated (data not shown).

4.4.2 Experiment

Ten consenting subjects (3 female, mean age 29 ± 6 years) were successfully scanned on 1.5, 3 and 7 T systems. Examples of fractional BOLD and CBF responses to motor tasks are shown in figure 4.3. Group average responses to hypercapnia and motor tasks are summarised in table 4.1. End-tidal CO_2 levels were monitored throughout the course of the experiments; however, the equipment performed poorly and the resultant traces were deemed unreliable, and thus are not reported here. Although unconfirmed, there is no reason to believe that end-tidal CO_2 modulations were inconsistent between the three scan suites. The BOLD response appears smallest at 3 T because of the shorter than usual echo time (TE = 17 ms), whereas the echo times used at 1.5 and 7 T were close to the field-strength-optimised values. Nevertheless, the BOLD signal at this shorter echo time of 17 ms at 3 T was easily sufficient for this analysis; hence a second echo was not acquired. Changes in CBF are consistent between 3 and

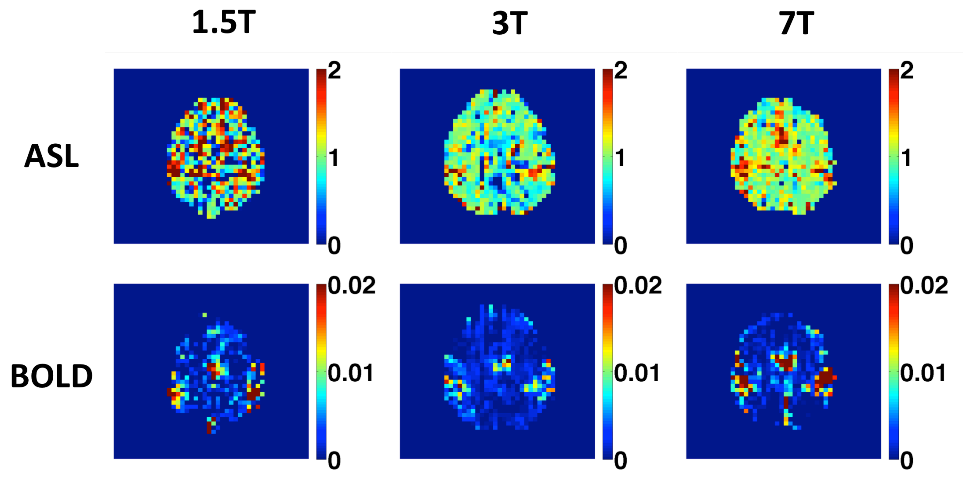

Figure 4.3: ASL and BOLD responses to motor tasks for one representative subject. ASL units are normalised to baseline, as are BOLD signal increases. Note that no smoothing has been applied.

Table 4.1: Summary of experimental results, given as mean ± standard deviation. CBF and CMRO$_2$ have been normalised to baseline values (no change = 1), and ΔBOLD and M are given as fractional changes with respect to baseline (no change = 0). Optimal TE is 50/35/25 ms at 1.5/3/7 T respectively.

		1.5 T	**3 T**	**7 T**
BOLD only ROI	ΔBOLD to CO$_2$	0.017 ± 0.005	0.010 ± 0.002	0.017 ± 0.006
	ΔBOLD to motor	0.012 ± 0.003	0.007 ± 0.002	0.014 ± 0.004
	CBF to CO$_2$	1.34 ± 0.05	1.24 ± 0.05	1.24 ± 0.07
	CBF to motor	1.58 ± 0.08	1.41 ± 0.05	1.42 ± 0.07
	M	0.055 ± 0.015	0.051 ± 0.011	0.115 ± 0.044
	M at optimal TE	0.055 ± 0.015	0.105 ± 0.023	0.169 ± 0.064
	CMRO$_2$ to motor	1.26 ± 0.08	1.19 ± 0.06	1.13 ± 0.07
	Voxels analysed	118 ± 41	197 ± 61	204 ± 88
BOLD/GM ROI	ΔBOLD to CO$_2$	0.018 ± 0.005	0.009 ± 0.002	0.016 ± 0.006
	ΔBOLD to motor	0.013 ± 0.003	0.006 ± 0.001	0.014 ± 0.004
	CBF to CO$_2$	1.20 ± 0.05	1.13 ± 0.03	1.12 ± 0.03
	CBF to motor	1.47 ± 0.08	1.31 ± 0.05	1.33 ± 0.05
	M	0.088 ± 0.024	0.072 ± 0.012	0.186 ± 0.079
	M at optimal TE	0.088 ± 0.024	0.149 ± 0.026	0.274 ± 0.116
	CMRO$_2$ to motor	1.25 ± 0.07	1.17 ± 0.05	1.15 ± 0.04
	Voxels analysed	61 ± 23	95 ± 35	94 ± 44

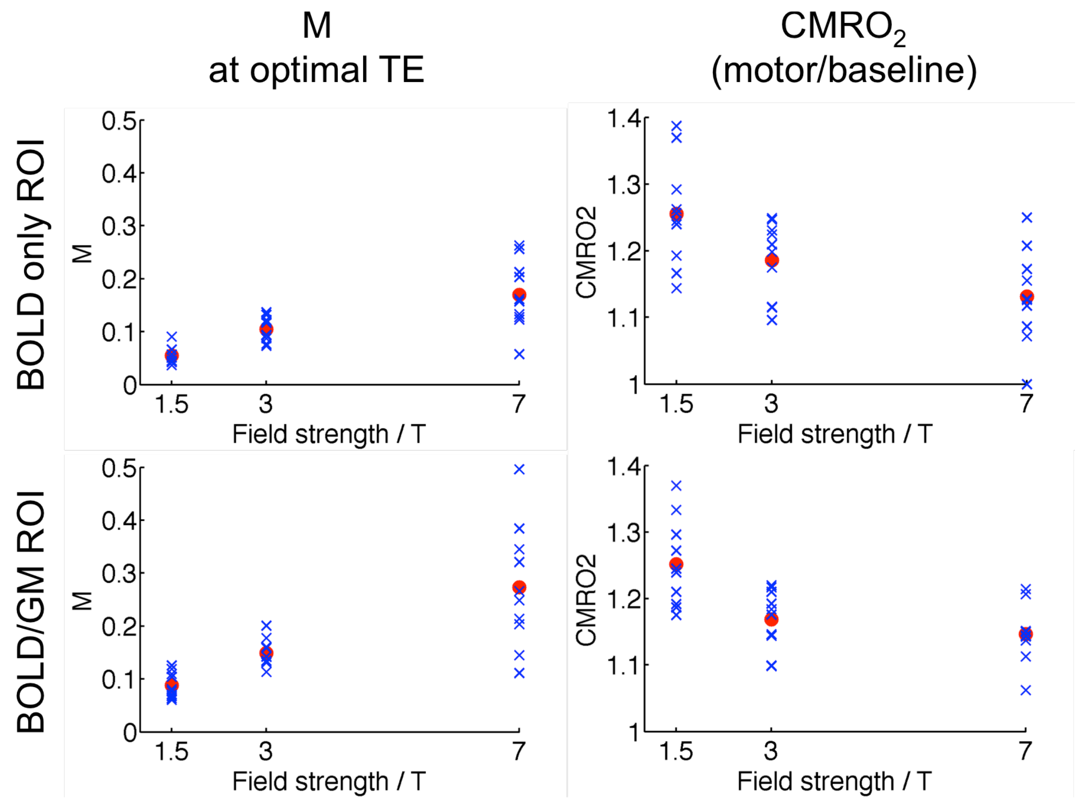

Figure 4.4: M and relative CMRO$_2$ as a function of field strength. Individual subjects are marked by blue crosses, group means by red circles.

7 T but are substantially higher at 1.5 T for both stimuli and both ROIs.

Figure 4.4 shows how M and relative CMRO$_2$ to motor tasks vary with field strength, where each blue cross represents an individual subject, and group means are indicated by red circles. The BOLD/GM ROI produces consistently higher M estimates than the BOLD only ROI. There is a much larger standard deviation in M values at 7 T than at 1.5 or 3 T; however this variability does not propagate to CMRO$_2$, where the largest inter-subject standard deviation is seen at 1.5 T, regardless of the ROI used.

One sample paired t-tests were carried out to determine whether relative CMRO$_2$ changes were consistent between field strengths. For the BOLD/GM ROI analysis, 1.5 T and 3 T results were shown to be inconsistent ($p = 0.022$). Similarly, the null hypothesis was rejected when comparing 1.5 T and 7 T ($p <$

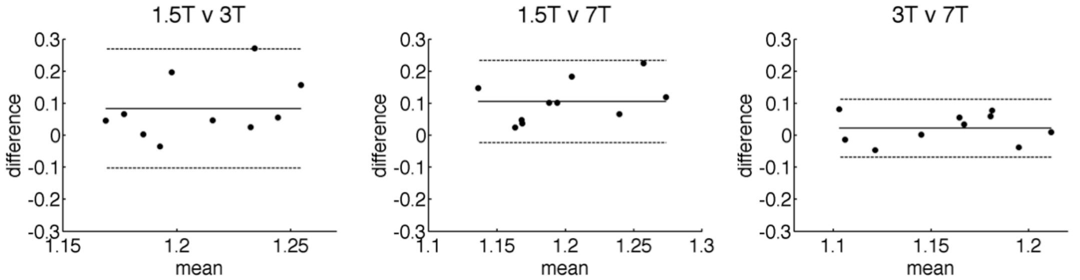

Figure 4.5: Bland-Altman plots comparing relative $CMRO_2$ to motor tasks (BOLD/GM ROI) at different fields. In all diagrams, mean differences are shown as solid lines and 95% confidence intervals as dashed lines.

0.001). However, 3 T and 7 T did not yield significantly different results ($p = 0.166$). When considering relative $CMRO_2$ in the BOLD only ROI, only 1.5 T vs. 7 T reached statistical significance ($p = 0.001$).

The Bland-Altman diagrams in figure 4.5 show graphically that the relative $CMRO_2$ to motor tasks as estimated by the Davis model at 3 and 7 T are in good agreement. However, they are consistently higher when carried out at 1.5 T, compared with either 3 or 7 T, by an average of approximately 10% (using the BOLD/GM ROI).

CBF responses to motor tasks (figure 4.6) and hypercapnia (data not shown) had a significantly broader distribution at 1.5 T than at 3 or 7 T. After applying voxel exclusion criteria (illustrated by solid red lines in figure 4.6), the mean of the remaining voxels (indicated by the dashed lines) was larger at 1.5 T than at higher fields. For illustrative purposes figure 4.6 includes data from all 10 subjects, but the same trends were seen at the single subject level.

Finally, figure 4.7 shows how the SNR of resting ASL data increases with field strength. This is generally considered to be the limiting factor on the accuracy of calibrated BOLD methods, as the ASL signal – the difference between tag and control images – is always substantially smaller than the directly measured BOLD signal.

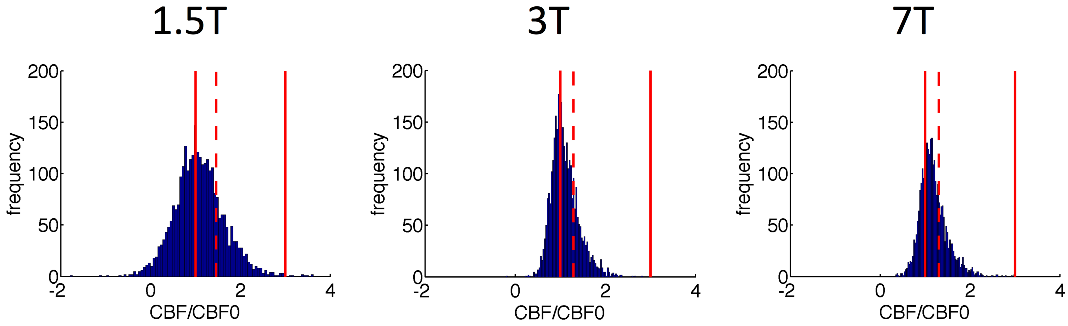

Figure 4.6: Histograms of voxel-wise blood flow response to motor tasks (C+D only), pooled from all 10 subjects' BOLD/GM ROIs. Solid red lines indicate cutoff conditions beyond which voxels were excluded from further analysis; dashed red lines indicate means of remaining voxels.

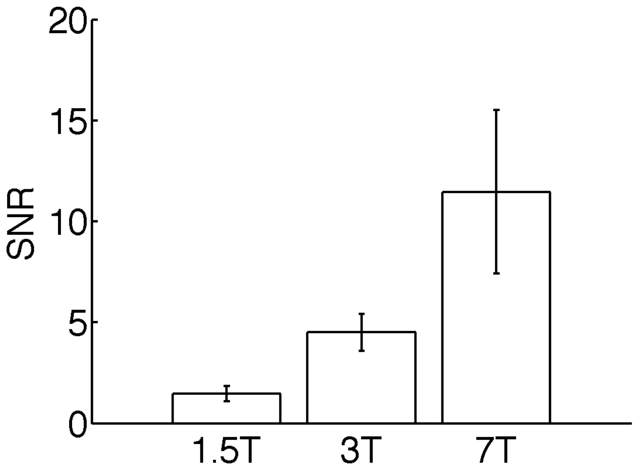

Figure 4.7: Signal-to-noise ratios of subtracted ASL images (tag–control) at different field strengths during the baseline condition. Signal was measured in motor regions, defined by BOLD/GM ROIs (prior to the removal of noisy voxels). Error bars show ± one standard deviation.

4.5 Discussion

4.5.1 Main Findings

The relative changes in CBF and $CMRO_2$ in response to a motor task observed in this study are broadly in line with those reported in the literature. For example, Donahue *et al.* reported a CBF increase of 46 ± 11% and a $CMRO_2$ increase of 12 ± 13% at 3 T [76]; Kastrup *et al.* reported a CBF increase of 71 ± 9% and a $CMRO_2$ increase of 16 ± 9% at 1.5 T [77]; Petr *et al.* reported a group average CBF increase of 47.2% at 3 T [78]; Stefanovic *et al.* reported a CBF change of 45.6 ± 0.57% at 1.5 T [79]; and Vilela *et al.* reported a CBF change of 62 ± 7% at 3 T [80]. All of these studies also used pulsed ASL techniques.

Estimates of M were observed to increase roughly linearly with field strength (figure 4.4), consistent with the results of the detailed BOLD signal model simulations (figure 4.2). M values at 7 T were found to have the largest standard deviation, despite the predicted improvements in SNR (table 4.1). Simulations indicate that variations in the underlying cerebral physiology (such as CBV and OEF) will result in a broader range of M values as magnetic field increases. This suggests that the increase in the standard deviation of M at higher fields is due to differences in physiology across the subject group, rather than an increase in random noise. This ability of M to control for physiological variability is an important characteristic of the Davis model, meaning that this variability is not propagated through to estimates of $CMRO_2$ change.

Intra-subject $CMRO_2$ was consistent between 3 and 7 T, which is encouraging for research centres investing in ultra-high field scanners. Future studies at these high fields could make use of the improved SNR to image at a higher resolution than has been possible until now. Changes in $CMRO_2$ measured at

1.5 T were consistently greater than those at 3 and 7 T (figures 4.4 and 4.5). It is hypothesised that this is an artefact of the lower SNR of 1.5 T scanners (see figure 4.7) combined with the voxel inclusion criteria for ROI analysis, which together artificially increase the average CBF response of the remaining voxels for analysis at 1.5 T as compared to 3 and 7 T. As figure 4.6 shows, the distribution of motor responses is much broader at 1.5 T than at higher field strengths, elevating the mean of remaining voxels.

The exclusion of approximately 50% of voxels from further analysis within the BOLD/GM ROI at 1.5 T is a cause for concern. In experiments carried out at either 3 or 7 T, ROIs are typically defined from voxels that exhibit positive BOLD and ASL responses (either in absolute terms or those with the highest z-stats) to tasks, and there is no need to define an additional 'GM' criterion. Unfortunately due to the poor SNR of pulsed ASL data, especially at 1.5 T, this was not viable in the current study and it was necessary to rely only on BOLD and resting ASL data for ROI determination. Figure 4.6 highlights the difficulties of using pulsed ASL at 1.5 T, demonstrating that the high level of noise can introduce significant biases during analysis, and that these results should be interpreted with caution.

4.5.2 ROI Selection

The large physiological and inherent scanner noise present in functional data, especially in ASL, presents a challenge. Increasing voxel size helps to increase SNR, but at the cost of lower specificity and greater partial voluming within voxels. This can make it difficult to create accurate GM masks, as many voxels will contain a mix of tissue types. In addition, the small number of slices and large voxels acquired in the current study made accurate co-registration of functional to structural data impossible. As a surrogate, good tag-control contrast in resting ASL data (i.e. high baseline perfusion) was used to define GM voxels [52].

The choice of ROI – in this case, BOLD only versus BOLD/GM – had a significant impact on the ensuing estimates of M. Values calculated within the BOLD only motor ROI were comparable with results from previous studies at 3 T, at which the majority of calibrated fMRI studies have been carried out (see table 4.2). M values in the BOLD/GM ROI were larger, but were in closer agreement with the predictions of the simulations. This is likely a reflection on the assumptions of the detailed BOLD signal model used for simulations. In contrast the method used to create the BOLD only ROI intentionally followed the analysis procedure from past studies rather than matching modelling assumptions. Recent studies at 7 T have taken greater care to extract only GM voxels for analysis, with methods and resulting M values more similar to the current BOLD/GM ROI. Studies at 3 T have also recommended defining ROIs based on mapping stimulus evoked changes in CBF, which have been shown to result in greater reproducibility of $CMRO_2$ estimates across sessions [88]. Defining the ROI in this manner is also likely to more closely align with the assumptions of the detailed BOLD signal model. However, the ability to apply this technique in the current study was limited by the SNR of the ASL measurements, particularly at 1.5 T.

Because of the wide distribution of CBF changes within both ROIs, it was necessary to exclude some further voxels from later analysis. Thresholds were applied to include only those voxels with relative changes in CBF between 1 and 3 (in response to motor or hypercapnia stimuli) in order to remove voxels that were deemed unacceptably noisy or containing an insufficient fraction of grey matter. However, as the remaining voxels do not even approximate a normal distribution (see figure 4.6), neither the mean nor median values truly capture

Table 4.2: Comparison of M values in the current study with those in the literature. All studies used hypercapnia for calibration unless indicated otherwise. Note that all M values and errors have been linearly scaled to the optimal echo times of 50/35/25 ms for 1.5/3/7 T respectively.

Field	Study	ROI	M (at optimal TE)
1.5 T	**Current study (BOLD only ROI)**	**motor**	**0.055 ± 0.015**
	Davis *et al.* [42]	visual	0.056 ± 0.017
	Stefanovic *et al.* [79]	motor	0.061 ± 0.011
	Stefanovic *et al.* [81]	motor	0.072 ± 0.010
	Current study (BOLD/GM ROI)	**motor**	**0.088 ± 0.024**
	Kastrup *et al.* [77]	motor	0.113 ± 0.038
	Hoge *et al.* [47]	visual (single)	0.15 ± 0.06
	Hoge *et al.* [47]	visual (graded)	0.22 ± 0.03
3 T	Chiarelli *et al.* [82]	motor	0.047 ± 0.038
	Chen and Parrish [83]	motor	0.056 ± 0.015
	Ances *et al.* [84]	visual	0.067 ± 0.002
	Chiarelli *et al.* [43]	motor	0.069 ± 0.006 (oxygen)
	Mark *et al.* [28]	motor	0.081 ± 0.011
	Ances *et al.* [85]	visual	0.085 ± 0.006
	Current study (BOLD only ROI)	**motor**	**0.105 ± 0.023**
	Gauthier *et al.* [86]	visual	0.111 (carbogen)
	Lin *et al.* [87]	visual	0.123 ± 0.003
	Leontiev and Buxton [88]	visual	0.130 ± 0.069
	Perthen *et al.* [89]	visual	0.141 ± 0.013
	Current study (BOLD/GM ROI)	**motor**	**0.149 ± 0.026**
7 T	**Current study (BOLD only ROI)**	**motor**	**0.169 ± 0.064**
	Current study (BOLD/GM ROI)	**motor**	**0.274 ± 0.116**
	Driver *et al.* [75]	motor	0.28 ± 0.02 (oxygen)
	Hall *et al.* [90]	motor	0.29 ± 0.04
	Krieger *et al.* [60]	motor	0.309 ± 0.031 (carbogen)

the overall flow response in the ROI. Nonetheless convention was followed and mean values were used for further analysis, but this caused noticeably higher apparent blood flow responses at 1.5 T as compared to 3 and 7 T (see table 4.1).

The results of this study suggest that the Davis model is reassuringly insensitive to field strength, provided that the value for β is adjusted appropriately [42,74,75]. The observation that choice of ROI has a large effect on M but only a minimal impact on $CMRO_2$ is a reflection of the power of the model in regressing out potentially confounding parameters. By combining all auxiliary parameters into one calibration constant, M, the model becomes very wide-ranging and remains relatively insensitive to residual factors, at least within healthy tissue.

4.5.3 Limitations

The primary question that this study sought to answer was whether the translation of calibrated fMRI from 3 to 7 T would alter the estimated changes in $CMRO_2$ during a functional task. In an attempt to remove confounding factors from this comparison, scan parameters were kept constant wherever possible. This included implementing the same pulse sequence (FAIR) with the same readout (single echo EPI at 17 ms). Unfortunately the use of a single echo was not feasible at 1.5 T, where the optimal BOLD echo time is much longer (50 ms or more), so it was necessary to modify the sequence and add a second echo at this lower field strength. As a result of these choices, readouts were acquired at close to optimal BOLD echo times at 1.5 T (50 ms, optimal is 50 ms) and 7 T (17 ms, optimal is 25 ms), whereas the 3 T BOLD signal was extracted from the 17 ms echo despite a longer optimal TE of 35 ms. This discrepancy led to a lower experimental BOLD response at 3 T (see table 4.1), and may have negatively impacted the BOLD SNR at this field strength. The lower BOLD value was accounted for by the linear scaling of M value to the optimal echo time, although of course this cannot recover the lost SNR.

SNR is inherently lower at 1.5 T compared with higher field strengths. This problem has been amplified in this study by the use of a pulsed ASL sequence and a 12-channel head coil. In comparison to (pseudo-)continuous ASL, pulsed ASL is more sensitive to changes in flow velocity during motor tasks and gas challenges, as shortened arterial arrival times during stimulation may lead to differing volumes of tagged blood arriving at the imaging planes. Furthermore, the increased intravascular contribution to the BOLD signal at lower field strengths may further contribute to the $CMRO_2$ discrepancy; in the absence of large vessels, approximately 57% of all signal at 1.5 T is of intravascular origin, compared to about 36% at 3 T and a negligible contribution at 7 T [91].

Another consequence of the use of a pulsed ASL sequence is the potential for underestimating flow responses during hypercapnia. Tancredi *et al.* [92] have reported that although pulsed and pseudo-continuous methods show good agreement in baseline perfusion and focal activation responses, the global nature of the CBF increase during hypercapnia appears to lead to an underestimation in flow response when pulsed ASL is used. This may have led to an overestimation in M values and thus in relative $CMRO_2$ estimates during motor tasks. However, this issue would have impacted all fields equally, and thus is not expected to affect the conclusions of this study.

In order to implement the same protocol on all three scanners, it was necessary to make several compromises in terms of sequence design and choice of parameters. It is important to bear in mind that SNR at 1.5 and 3 T could be improved by implementing a pseudo-continuous ASL sequence; similarly the intrinsically greater SNR at 7 T could be utilised by increasing the resolution, which would also reduce physiological noise [93]. However, the primary aim of this work was to fairly compare the outcomes of the Davis model as a function of field strength only, by keeping as many other variables constant as possible.

4.6 Conclusions

Changes in $CMRO_2$ during a motor task, as calculated by the Davis model, were found to be consistent between 3 and 7 T and were also in close agreement with the results of theoretical simulations. This is encouraging for future studies of calibrated fMRI at ultra-high fields, and supports the continued use of this simple signal model. The lower SNR at 1.5 T may present problems for the calibrated fMRI method, which relies heavily on ASL data. In this study the $CMRO_2$ results were consistently over-estimated at 1.5 T, although this may be a result of the sub-optimal pulsed ASL sequence used. Voxel exclusion criteria and methods for ROI creation for post-processing are important and should be carefully considered and clearly stated in future studies, as they can have a significant impact on results.

5

Echo Time Dependence of Calibration Parameter M

5.1 Introduction

The calculation of M as an intermediate calibration constant is key to all flavours of the calibrated fMRI technique (see section 3.3 for details). M is a physiological parameter that will vary depending on the type of tissue, field strength, voxel size and physiology (including resting blood volume, haematocrit and oxygen extraction fraction). Its value also depends on scanning parameters such as the echo time, as this affects the size of the measured BOLD signal. It is commonly assumed that M is directly proportional to TE, allowing for experimental values to be linearly scaled for comparisons between studies [86], as was done in Chapter 4. However, this has never been experimentally verified, and it is not known if other factors contributing to M may have some additional, non-linear dependence on TE. This work aims to test the hypothesis that M varies linearly with TE.

5.2 Theory

The BOLD signal itself is sensitive to changes in the effective transverse relaxation rate, R_2^*, according to

$$\frac{\Delta\mathrm{BOLD}}{\mathrm{BOLD}_0} = e^{-\mathrm{TE}\cdot\Delta R_2^*} - 1 \approx -\mathrm{TE}\cdot\Delta R_2^*. \tag{5.1}$$

This makes it particularly sensitive to the presence of deoxygenated (paramagnetic) haemoglobin in the blood. It should be noted that equation 5.1 assumes negligible intravascular signal contribution, allowing the BOLD signal to be described by a simple, monoexponential expression, despite findings that intravascular spins contribute a significant fraction of observed BOLD signal changes (approximately 2/3 at 1.5 T [94] and 1/3 at 3 T [91]).

Neurological stimuli result in localised increases in blood flow and/or increases in CMRO$_2$, both of which affect R_2^* and thus the measured BOLD signal. This relationship may be described by the following equation [47]:

$$\frac{\Delta\mathrm{BOLD}}{\mathrm{BOLD}_0} = M\left\{1 - \left(\frac{\mathrm{CMRO}_2}{\mathrm{CMRO}_2|_0}\right)^{\beta}\left(\frac{\mathrm{CBF}}{\mathrm{CBF}_0}\right)^{\alpha-\beta}\right\} \tag{5.2}$$

where α is the Grubb coefficient relating changes in blood flow to blood volume, and β is a fitting parameter relating R_2^* to vessel size. In the specific case of a hypercapnic stimulus, CMRO$_2$ is assumed to remain unchanged. M is defined as $A\cdot\mathrm{TE}\cdot\mathrm{CBV}_0\cdot[\mathrm{dHb}]_{v0}^{\beta}$, where the baseline cerebral blood volume CBV$_0$, baseline venous deoxyhaemoglobin concentration $[\mathrm{dHb}]_{v0}$ and proportionality constant A are expected to be independent of echo time. Thus, M is predicted to be directly proportional to TE.

Equation 5.2 has been derived using a number of assumptions, including negligible deoxyhaemoglobin concentration in arterial blood, a consistent flow-volume coupling as first described by Grubb *et al.* [48], and the semi-empirical description of R_2^* as a function of CBV and deoxyhaemoglobin concentration [46, 47]. It is also based on equation 5.1, which assumes no intravascular signal contribution, as mentioned above.

The aim of this work was to investigate whether experimentally acquired BOLD signal change and M vary in direct proportion with TE as predicted by the theory outlined above. In addition, the validity of the negligible intravascular signal assumption was explored by acquiring data with and without the use of flow crushing gradients to suppress signal from fast-flowing spins.

5.3 Methods

A pseudo-continuous ASL sequence was implemented on a 3 T Siemens Verio scanner with a 32-channel head coil, with a multi-slice, multi-echo EPI readout. 6 slices were acquired with 5 echoes per slice, at 20/35/49/64/78 ms respectively, with GRAPPA acceleration factor of 3, tag duration 1.4 s, post-label delay 1.8 s and TR of 4 s. In-plane resolution was 3.4×3.4 mm, with 5 mm slice thickness and a distance factor of 50%.

In order to investigate the effects of intravascular spins on the BOLD signal and thus on M, the sequence was designed with the option of adding bipolar flow crushing gradients immediately before the first readout. Where used, these were set to have a cutoff velocity of 1.9 cm/s. Where flow crushers were not used, they were replaced by a short, empty event block within the sequence; in this way, all echoes were acquired at the same echo times with crushers turned on and off. Higher SNR would have been achieved for the ASL with a TE shorter than 20 ms, however this would not have allowed for the flow crushing gradients to be incorporated, and thus not enabled us to answer the key question on intravascular signal contribution.

Ethical approval was granted for this study by the Oxfordshire Research Ethics Committee, and 8 healthy volunteers (5 female; mean age 24 ± 2 years) were scanned after giving informed consent. The imaging protocol consisted of two 3-minute periods of hypercapnia (delivering a gas mixture of 10% CO_2, 21% O_2 and balance nitrogen) interleaved with three 2-minute periods of baseline (breathing medical air; 21% O_2, balance nitrogen), resulting in a single scan time of 12 minutes. Both gas mixtures were delivered through a nasal cannula (dual Nare, Flexicare, Mountain Ash, UK) and thus mixed with room air, resulting in a CO_2 stimulus of approximately 4% [95]. This protocol was run twice on every subject, both with and without flow crushing gradients.

5.3.1 Data Analysis

Post-processing was performed using the FMRIB Software Library (FSL) and MATLAB (MathWorks, Natick, MA, USA). After motion correction [70] and brain extraction [71], highpass filtering was applied with a cutoff value of 10 s for ASL data (first echo only) and 300 s for BOLD (all 5 echoes). No spatial smoothing was applied. A general linear model was used to calculate voxelwise flow responses to hypercapnia from the first echo, and BOLD responses from all echoes. R_2^* maps were created from time-averaged signals at all 5 echo times for both crushed and non-crushed acquisitions. Monoexponential signal decay was assumed.

A grey matter ROI was created for each scan from voxels with significant tag-control (resting) ASL signal and a significant BOLD response to hypercapnia in at least 3 of the 5 BOLD echoes, where ‘significant’ was defined as the 40% of brain voxels with the highest z-statistics for the relevant contrast. The first condition was used because good tag-control contrast during ASL is indicative of high perfusion voxels with relatively short mean bolus arrival times, which are likely to contain high fractions of grey matter. The additional condition on BOLD response was included to avoid introducing a bias by selection based on one contrast only. Setting a percentile rather than absolute z-statistic threshold ensured ROIs of similar sizes across subjects and scans. This method also avoided the need to register to higher resolution structural images, which would invariably have introduced some smoothing and a reduction in spatial specificity. To emulate the more typical situation in which only one short-TE ASL and one longer-TE BOLD acquisition are acquired, the analysis was repeated with a separate grey matter ROI created for each BOLD TE.

Relative change in CBF was calculated on a voxelwise basis, assuming tagging efficiencies of 92% during normocapnia and 83% during hypercapnia [1]. In order to remove excessively noisy data, voxels were excluded from ROI analysis if the CBF response to hypercapnia was negative or greater than 200%, or if the BOLD response was negative or greater than 15%. A regional M-value was then calculated from mean CBF and BOLD responses within the remaining voxels (see equation 5.2), using $\alpha = 0.18$ (as measured by Chen and Pike [44] in a human MRI study investigating the venous response to hypercapnia) and $\beta = 1.3$ (appropriate for the field strength of 3 T as per Bulte *et al.* [74]).

5.4 Results

All scans were carried out successfully by all 8 volunteers. Mean CBF and BOLD changes to hypercapnia, with crushers on and off, are shown in table 5.1. These were calculated within the grey matter ROI for each subject. R_2^* maps from one representative subject are shown in figure 5.1. There was a small reduction in R_2^* when crushers were applied, consistent with a reduction in signal from the

Table 5.1: Mean ± standard deviation results for CBF and BOLD changes during hypercapnia. CBF changes were only measured from the first echo at 20 ms.

	crushers off	**crushers on**
CBF/CBF_0	1.39 ± 0.05	1.45 ± 0.09
% BOLD, 20 ms	2.02 ± 0.94	1.34 ± 0.39
% BOLD, 35 ms	2.83 ± 1.23	2.30 ± 0.61
% BOLD, 49 ms	3.65 ± 1.57	3.20 ± 0.79
% BOLD, 64 ms	4.33 ± 1.69	3.94 ± 0.97
% BOLD, 78 ms	4.92 ± 1.69	4.48 ± 1.02

intravascular compartment.

Figure 5.2 plots the mean grey matter M value as a function of TE for each of the 8 subjects. Figure 5.3 shows the linear fitting to the group mean BOLD and M results as a function of echo time, for the cases where crusher gradients were turned on (blue triangles) and off (red squares). The linear model proved a good fit for the data, as demonstrated by R^2 values greater than 0.98 in all cases.

Figure 5.4 shows the percentage BOLD signal change (TE = 35 ms) in response to hypercapnia in a representative subject for the cases where crushing gradients were turned off and on. The difference image demonstrates that the BOLD response is reduced throughout grey matter when the crushers are turned on, presumably because these reduced the signal contribution from small veins throughout the brain. Table 5.1 and figure 5.3(a) show the magnitude of this reduction in BOLD response within grey matter ROIs across all subjects. As a result, M values were consistently reduced when crushers were applied; for example, at the most typical BOLD echo time of 35 ms, M was measured to be 9.2 ± 4.1% (mean ± standard deviation) without crushers, and 6.7 ± 1.4% with crusher gradients turned on. y-intercepts of 3.5% (crushers off) and 1.1% (crushers on) were observed, corresponding to the theoretical M at TE = 0, which is assumed by the model to be zero (see equations 5.1 and 5.2).

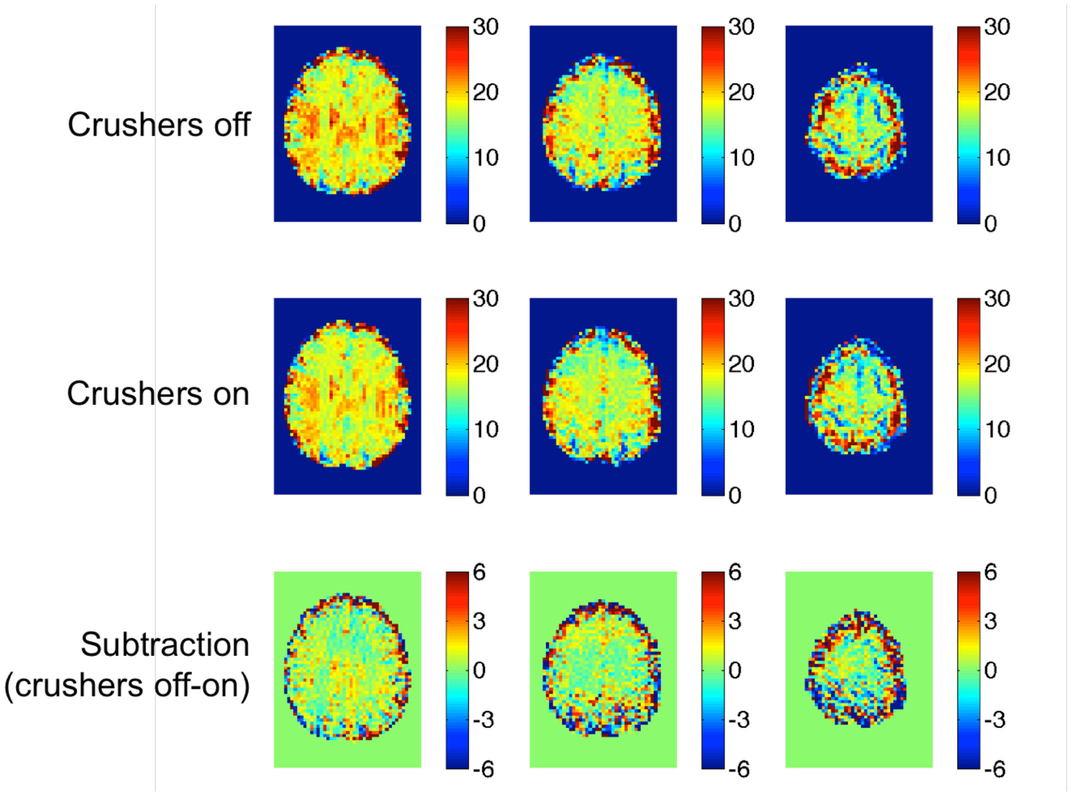

Figure 5.1: R_2^* maps for a single representative subject.

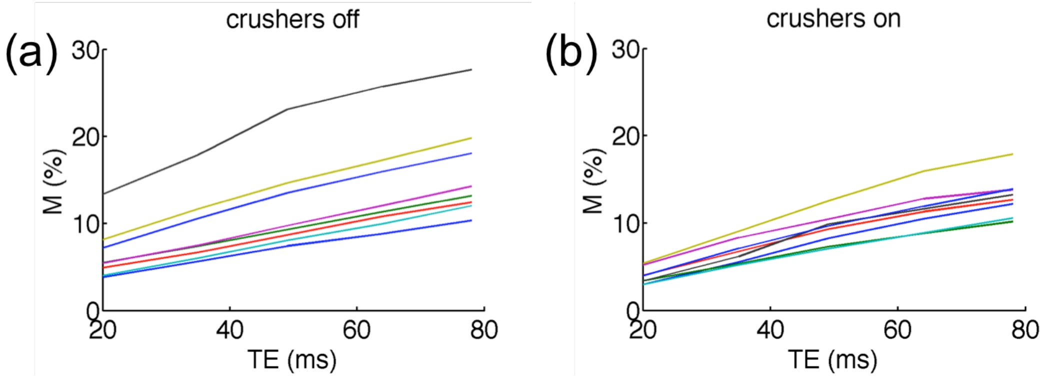

Figure 5.2: M as a function of TE, as typically measured in a calibrated fMRI experiment (a) and with intravascular crushers applied (b). Each line represents a different subject.

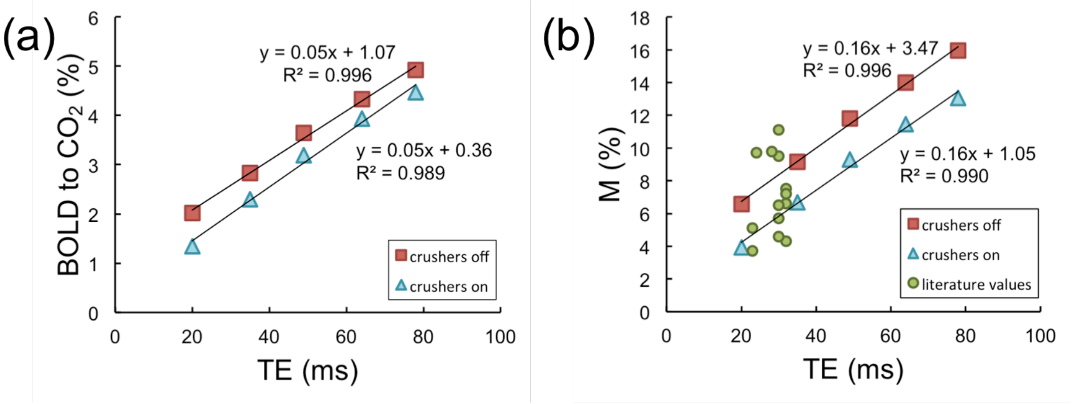

Figure 5.3: Mean BOLD response to hypercapnia (a) and mean M (b) from this study, with crushers turned on (blue triangles) and off (red squares). The results of linear fits have been added. Green circles show M results from past studies over a range of BOLD echo times.

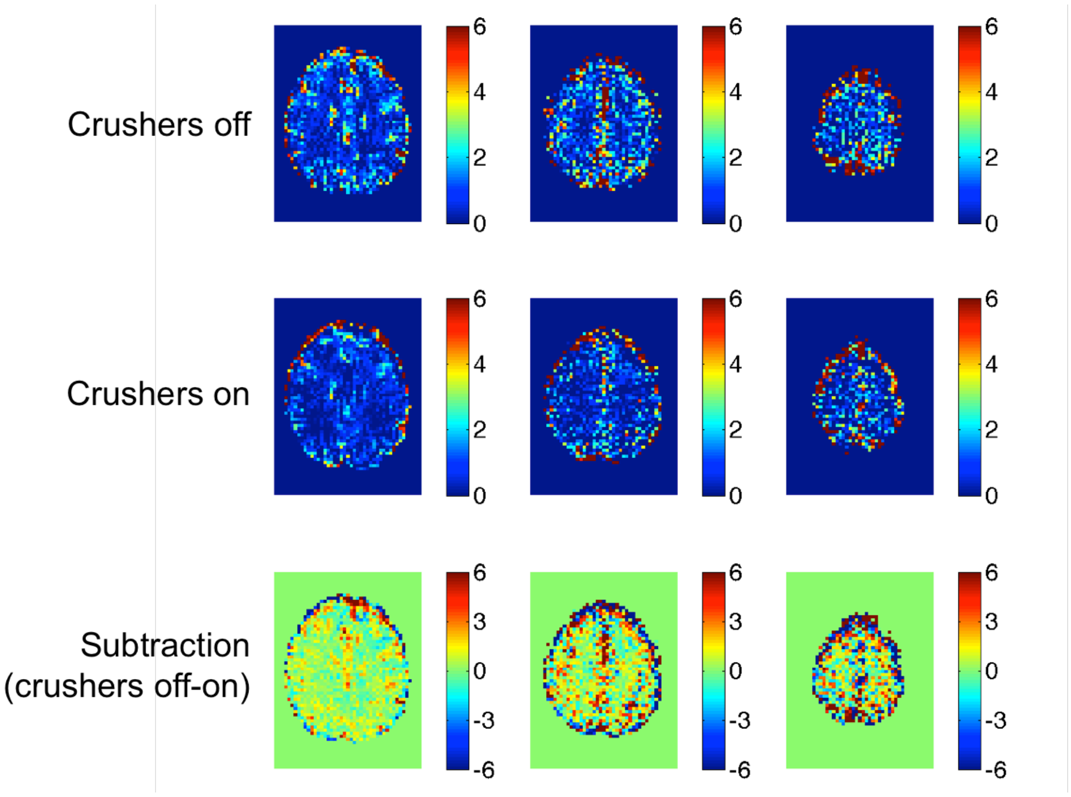

Figure 5.4: Percentage BOLD signal responses to hypercapnic stimuli in a single representative subject.

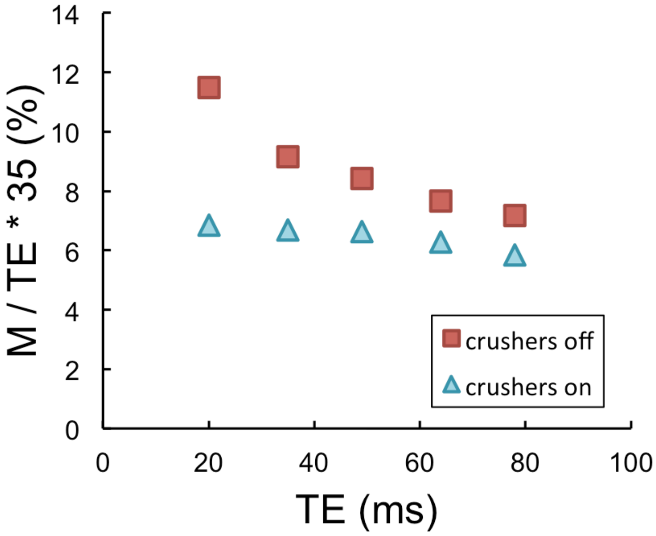

Figure 5.5: Mean M values measured with crushers on (blue triangles) and off (red squares), linearly scaled to an optimal echo time of 35 ms by assuming an intercept of zero.

Figure 5.5 shows the mean M values scaled to a TE of 35 ms, where the intercept of the linear fit has been assumed to be zero. If M were a direct linear function of TE, as predicted by equations 5.1 and 5.2, figure 5.5 would show that the normalised M was independent of TE. For the 'crushers on' situation this is very nearly the case, with small deviations visible only at very long echo times (TE $>$ 50 ms). However, when crushers are turned off it is evident that the scaled M value decreases monotonically with TE, demonstrating that M is not a purely linear function of TE with an intercept of zero as has previously been assumed.

5.5 Discussion

The green circles in figure 5.3(b) represent M values quoted in the literature, which have been taken from the following works: Ances *et al.* [84, 85], Chen and Parrish [83], Chiarelli *et al.* [43, 82], Gauthier *et al.* [86], Leontiev and Buxton [88], Lin *et al.* [87] and Perthen *et al.* [89]. M values found in this study fall well within this range.

As seen in figure 5.3(a), the BOLD signal change in response to a hypercapnic stimulus is not directly proportional to TE. The reduction in the intercept from 1.07 without crushers to 0.36 when crushers were applied suggests that the deviation from behaviour predicted by equation 5.1 is likely due to intravascular signal contamination. The crusher gradients used in this sequence had a cutoff velocity of 1.9 cm/s and were only applied in the head-foot direction; hence although they reduced the intravascular signal contribution, they will not have eliminated it completely.

The second assumption made by equation 5.1 is that the exponent is sufficiently small to allow for linearisation of the exponential. For typical BOLD responses of 3% (at TE = 35 ms), the error introduced by this linearisation in the estimation of ΔR_2^* is less than 2%. In individual voxels with larger BOLD responses – such as those containing large veins – this error will be increased. However, linearising an exponential function and extrapolating this back to zero would tend to underestimate the value of an intercept, so this effect is unlikely to have contributed to the positive BOLD intercepts observed in this study.

Having seen that the BOLD response is not a directly linear function of TE, it follows that the same is true of M. Again, the y-intercept (which represents the deviation from predicted behaviour) was reduced but not eliminated when crushers were applied. In studies where two echoes are acquired (e.g. by using a dual-echo or interleaved pulse sequence), it would be possible to estimate this intercept on a study- or subject-specific basis, which may significantly improve the accuracy of scaling M to any desired echo time.

In figure 5.5 the mean M values have been normalised to an echo time of 35 ms, assuming a linear relationship with zero intercept. This gives an idea of the errors introduced by the commonly employed linear scaling method. For the case where crushers are turned on (blue triangles), normalised M is almost a flat function of TE from 35 ms, meaning that any error in the scaling of M for typical BOLD echo times (30–50 ms) appears negligible. Even where crushers are turned off (indicated by red squares), the error introduced by the scaling is typically moderate. For example, scaling an experimental M with a BOLD TE of 49 ms to 35 ms yields an M of 8.4%, where the 'true' 35 ms M value is 9.2%. However, scaling up from a shorter experimental echo time introduces a greater error, for example from 20 ms to 35 ms would give a scaled M of 11.5% compared to the actual value of 9.2%.

One must bear in mind that the scaling of M with TE is only relevant when comparing between studies that had different BOLD echo times. Most experiments that measure M do so in order to calculate changes in or absolute values of $CMRO_2$; within a single study, the BOLD echo time chosen should not have any significant impact on these results. This is at the very heart of the calibrated MRI methodology: the parameter M by design varies with experimental conditions in such a way as to allow the conversion from BOLD signal changes to underlying changes in oxygen metabolism. However, as the current protocol did not include the performance of any neurological tasks, this data is not capable of testing the conjecture that measured $CMRO_2$ is independent of BOLD echo time. As the theory behind the Davis model considers only extravascular BOLD signal contributions, one might expect that the application of flow crushers would improve the accuracy of $CMRO_2$ estimates, although at the expense of noisier ASL data because of a prolonged initial TE.

Echo time is not the only factor affecting M value; in addition to differences in physiology (resting blood volume, mean vessel size etc.), voxel size, field inhomogeneities and scanner hardware will also affect its value. Thus one would expect a certain amount of variation in M values measured at different imaging centres, as is demonstrated by the substantial range in literature M values shown in figure 5.3(b). M values are generally scaled and quoted between studies for a coarse comparison only, and the additional error or variability introduced by assuming a linear scaling with zero intercept is likely to be small compared to these other considerations, even for the more common case where crusher gradients are not applied.

The choice of constraints used to define ROIs in functional MRI has been a controversial subject for many years. In the field of calibrated MRI, both ASL and BOLD signals are of interest, and ROIs have typically been created from voxels that are responsive to both contrasts in an attempt to avoid or minimise any biasing. In this study, significant BOLD responses to hypercapnia were required at 3 or more echo times, as well as good perfusion, in order to be labeled a 'grey matter voxel'. This resulted in the creation of a common ROI for all echoes, ensuring that any observed trends are not mere artefacts of differences in ROIs (although it should be noted that excessively noisy voxels were individually removed from these ROIs during further analysis). In order to replicate the more common experimental situation in which only one BOLD-weighted echo is acquired, the analysis was repeated with a separate grey matter ROI being created for each BOLD echo time. The trends observed were unchanged, however the average BOLD responses to hypercapnia were slightly increased (2.98 ± 1.35% with no crushers at 35 ms as compared to 2.02 ± 0.94% in main analysis), as were M values (9.5 ± 4.5% compared to 9.2 ± 4.1%). Continuing the example of a 20 ms ASL/35 ms BOLD acquisition with crusher gradients turned off, and defining a grey matter ROI based only on good resting ASL signal, an M value of 5.7 ± 2.3% was calculated. When using good BOLD response to hypercapnia at 35 ms TE as our only condition, this increases to 8.1 ± 2.8%, and by combining the two conditions one ends up with 9.5 ± 4.5%. This demonstrates the importance of choosing and reporting ROI definitions carefully.

5.6 Conclusions

M has been commonly assumed to vary in direct proportion with TE. This work shows that the relationship is indeed linear ($R^2 = 0.996$ on data points averaged across 8 subjects), but has a non-zero intercept. The value of the intercept is reduced when crusher gradients are added to the sequence, suggesting that the deviation from theory arises from the false assumption of negligible intravascular BOLD signal contribution. Where two echoes are acquired during a dual-echo or interleaved sequence it would be possible to estimate the intercept on a study- or subject-specific basis, which could significantly improve the accuracy of scaling M to a different echo time. However, in practice, the errors introduced by the assumption of a zero intercept are relatively small between typical BOLD echo times of 30–50 ms. In general one should not put undue weight on agreements or disagreements in M values between different studies, especially when the echo times or ROIs used differ significantly, regardless of which scaling method is used.

5.7 Implications for Field Strength Study

In Chapter 4, simple linear scaling was used to convert experimental M values collected at 17 ms to optimal M values at 35 ms (at 3 T). The work shown in this chapter suggests that this will likely have introduced a scaling bias, tending to overestimate predicted M values for the optimal echo times. Unfortunately the 3 T data was acquired with a single echo only, so it is not possible to rescale the M values without making additional assumptions. If a value for the gradient $\Delta M/\Delta\mathrm{TE}$ were to be assumed, one could estimate the y-intercept (or vice versa) and perform an improved scaling on the M value. The results for assuming a gradient of 0.16 from the data collected in the current study are shown in table 5.2. The gradient was chosen to be fixed because it appears more stable between subjects than the y-intercept according to figure 5.2(a). The newly scaled M values still fall comfortably within the literature range (see table 4.2), and do not affect the calculated changes in CMRO$_2$. As such all the conclusions drawn from the data in Chapter 4 still remain valid.

Table 5.2: 3 T results from Chapter 4, newly scaled according to $y = mx +$ intercept, where $m = 0.16$ %/ms (see figure 5.3(b)) or 1.6 /s.

	BOLD only ROI	**BOLD/GM ROI**
experimental M (17 ms)	0.051	0.072
simple scaled M (35 ms)	**0.105**	**0.149**
assumed gradient $\Delta M/\Delta\mathrm{TE}$	1.6	1.6
estimated y-intercept	0.024	0.045
newly scaled M (35 ms)	**0.080**	**0.101**

6

A Direct Comparison between Gas-Calibrated MRI and Triple Oxygen PET

6.1 Introduction

Oxygen extraction fraction (OEF) directly relates tissue perfusion with local oxygen consumption, and as such is a valuable marker for the health of brain tissue. It has proved an extremely useful tool in the imaging of cerebral ischaemia following stroke [96, 97] and traumatic brain injury [39], as well as investigating mechanisms in the healthy brain [98]. For a more thorough discussion of the history and applications of OEF imaging, see for example [99]. The gold standard method for measuring OEF is triple oxygen PET; however, as discussed in section 3.2.2, very few sites have the capability for performing this procedure. In addition, the large radiation dose limits the number of scans that can be carried out in healthy volunteers, particularly women who may bear children in the future.

Recently a new method capable of mapping resting OEF using MRI was proposed [1–3]. In this approach, two (or more) gas mixtures are administered to the subject, one with high oxygen content and one with elevated carbon dioxide. By making use of both the BOLD signal and the non-invasive, perfusion-sensitive ASL technique, the absolute OEF and total oxygen consumption in the brain may be calculated (see section 3.3.3 for full details).

Gas-calibrated MRI studies have reported plausible OEF results, for example Bulte *et al.* reported a mean of 38 ± 14% [1] and Wise *et al.* reported 47 ± 12% [3], compared to 44 ± 6% as measured by PET in a large multi-centre study [100]. However the method has yet to be validated against an independent measure of oxygen metabolism. The aim of this study was to perform a direct comparison of cerebral physiology metrics (CBF, OEF and $CMRO_2$) using gas-calibrated MRI and the gold standard triple oxygen PET method in a healthy cohort.

6.2 Methods

Ethical approval for this work was given by the National Research Ethics Service (NRES) Committee South Central (Berkshire) and the Administration of Radioactive Substances Advisory Committee (ARSAC). 15 healthy subjects were recruited (12 male, mean age 36 ± 10 years) and informed consent was given. The use of PET restricted female subjects to those without childbearing potential. The MRI protocol was carried out first in all cases to confirm the absence of any contraindications for the more invasive PET procedure. PET scans were carried out on the same day as the MRI to minimise true physiological variation between the two modalities.

6.2.1 MR Imaging

MR images were acquired on a 3 T Siemens Verio scanner (Siemens, Erlangen) with a 32-channel head coil. Resting blood flow was measured using a pseudo-continuous arterial spin labelling (PCASL) scan with multiple post-labelling delay (PLD) times, as recommended by Alsop *et al.* [14]: 3.4×3.4×6.0 mm voxels, 15 slices, TR of 4 s, TE of 14 ms, partial Fourier 6/8, tag duration of 1400 ms and PLDs of 250/500/750/1000/1250 ms, resulting in a scan time of 6:28 minutes. The labelling plane was placed halfway between contortions of the vertebral arteries, as determined by time-of-flight angiography of the neck.

For the main scan a double-excitation PCASL/BOLD sequence was implemented [29]. The resolution matched that of the resting PCASL scan, as did all other PCASL timing parameters. Because this was a functional scan, only a single PLD was used (1100 ms). Pre-saturation of the imaging volume was turned off in order to preserve BOLD contrast. Other parameters were a TR of 4s, TE of 12/33 ms for ASL/BOLD readouts, flip angle of 60°, partial Fourier off, and GRAPPA factor 2. Total imaging time was 17 minutes.

Subjects were fitted with a 2-tube nasal cannula (Dual Nare with CO2 Monitoring, Flexicare, Mountain Ash, UK) whilst lying in the scanner, through which mixtures of either medical air, 10% CO_2 in air (hypercapnia) or 100% oxygen (hyperoxia) were delivered. Gas flow was manually controlled from the scanner control room and a constant flow rate of 8 l/min was maintained. After an initial minute of air, two 2-minute blocks of hypercapnia (followed by 1 minute air) were interleaved with two 3-minute blocks of hyperoxia (each followed by 2 minutes air). Because of inevitable mixing with room air, the true inspired gas fractions were approximately 4% CO_2 during hypercapnia and 50% oxygen during hyperoxia. Gas composition was continuously monitored using a Gas

Analyzer (ADInstruments, Dunedin, New Zealand) connected to an ADInstruments Powerlab.

A 1 mm^3 MPRAGE structural image was acquired for registration purposes. Field maps and head and body coil calibration images were taken for post-processing corrections, and a HASTE image was acquired to confirm the lack of any pathology that may contra-indicate a PET procedure. The total time for which subjects were in the MR scanner was approximately 40 minutes.

6.2.2 MR Analysis

Resting ASL data were analysed using the BASIL toolbox [101]. Data collected during the gas paradigm were separated into ASL and BOLD time courses, both of which were field map corrected, motion corrected and smoothed with a 5mm Gaussian kernel. Both time courses were fully modelled in FEAT (FSL, FMRIB Centre, Oxford, UK) with 5 explanatory variables (EVs), as follows: (1) square on/off waveform representing tag/control states; (2) BOLD response to hypercapnia, modelled with a gamma convolution (mean lag 30 s, stddev 10 s); (3) flow response to hypercapnia, modelled as an interaction between contrasts 1 and 2 above; (4) BOLD response to hyperoxia, modelled with a gamma convolution (mean lag 60 s, stddev 60 s); and (5) flow response to hyperoxia, as an interaction between contrasts 1 and 4. The ASL data and model were highpass filtered with a 10 s cutoff to remove the majority of BOLD signal contribution. BOLD data and model were highpass filtered at 485 s to remove any long-term signal drift.

Flow response to hypercapnia was calculated as EV3/EV1 (short echo ASL data), and BOLD responses to hypercapnia and hyperoxia were defined by EV2 and EV4, respectively (longer echo BOLD data). OEF was calculated on a voxel-wise basis following the method described by Bulte *et al.* [1]. In the first step M was calculated from ASL and BOLD responses to hypercapnia using the expression

$$\frac{\Delta\text{BOLD}}{\text{BOLD}_0} = M\left\{1 - \left(\frac{\text{CBF}}{\text{CBF}_0}\right)^{\alpha-\beta}\right\} \tag{6.1}$$

where it was assumed that there is no change in cerebral metabolism during transient mild hypercapnia [44, 102]. α was set to 0.18, as determined by Chen and Pike using MRI with a hypercapnia stimulus [50], and β to 1.3 [74]. In a second step this M value was used in conjunction with MRI and end-tidal data during hyperoxia stimuli to estimate OEF according to

$$\frac{\Delta\text{BOLD}}{\text{BOLD}_0} = M\left\{1 - \left(\frac{[\text{dHb}]_v^{ho}}{[\text{dHb}]_{v0}}\right)^{\beta}\right\}, \tag{6.2}$$

where the concentration of deoxyhaemoglobin in the venous blood, $[\text{dHb}]_v$, is a function of resting OEF, end-tidal expired oxygen fraction, atmospheric pressure, arterial–alveolar pressure gradient and blood haemoglobin concentration (see figure 3.2 for details). Hyperoxia-induced changes in CBF were neglected due to the low SNR of temporal ASL data, but no voxels were excluded from analysis at this stage. Atmospheric pressure measurements were taken from https://www.cl.cam.ac.uk/research/dtg/weather/index-daily-text.html on the day of each experiment. The arterial–alveolar pressure gradient (A–a) depends on the age (in years) of the subject and on the inspired fraction of oxygen, and was estimated as

$$\text{A–a (normoxia)} = \frac{\text{age} + 10}{4} \tag{6.3}$$

and

$$\text{A–a (hyperoxia)} = \text{A–a (normoxia)} + 18 \tag{6.4}$$

as described in [51]. Subject-specific values of haemoglobin concentration were used in the calculation of OEF, as measured from blood samples during the PET procedure. Finally, $CMRO_2$ was calculated as

$$\mathrm{CMRO_2} = \mathrm{OEF} \cdot \mathrm{CBF} \cdot \mathrm{C}_a\mathrm{O}_2 \tag{6.5}$$

where the total oxygen content C_aO_2 was again determined from PET blood samples.

6.2.3 PET Imaging

PET imaging was performed on a General Electric Advance scanner (GE Medical Systems, Milwaukee, USA). Data were acquired during a 7200 MBq inhalation of $^{15}O_2$ (2D mode, two 5-minute frames after 10 minutes to reach steady state); during an 800 MBq $H_2{}^{15}O$ infusion (3D mode, two 5-minute frames after 10 minutes to reach steady state); and following a 1-minute 300 MBq inhalation of $C^{15}O$ (3D mode, one 5-minute frame). Arterial blood was sampled throughout. For more details on the theoretical basis of this method, refer to section 3.2.2.

As part of a parallel study, near-infrared spectrometry (NIRS) data were collected simultaneously with the PET using a NIRO 200 device (Hamamatsu Photonics, Hamamatsu, Japan). Two sensors were placed on subjects' foreheads, and OEF was calculated [103] using arterial and tissue oxygen saturations (quantified from blood samples and the NIRS device, respectively) with an assumed arterial/venous blood volume ratio of 30/70 [104].

6.2.4 PET Analysis

Corrections for attenuation, scatter, randoms and dead time were incorporated into the image reconstruction procedure [105,106]. Simultaneous PET and arterial tracer activity measurements were input into standard models [107, 108] to calculate maps of CBF, CBV, OEF and $CMRO_2$, using a brain–blood partition coefficient for water of $\rho = 0.95$ [109] and a small to large vessel haematocrit ratio of $r = 0.85$ [110]. Co-registration and 'hot spot' artefact removal were performed using the custom analysis software PETAN [111].

6.2.5 Regions of Interest

Grey matter partial volume maps were created for each subject from their high-resolution MRI structural scans using FAST [112]. These were thresholded at 50% to produce grey matter ROIs. Resting CBF images from both MRI and PET modalities were registered to structural space for each subject, and the resulting transformation matrices were then also applied to the OEF and $CMRO_2$ images. Any grey matter voxels for which OEF was less than 10% or more than 100% were excluded from the ROI for the relevant modality, as this was considered unphysiological and was likely induced by noise or partial voluming during co-registration.

For MRI results reported in native space, the high-resolution grey matter partial volume maps were registered to functional space using the inverted MRI CBF-to-structural transformation matrices. The maps were thresholded in functional space to create low-resolution grey matter ROIs of voxels containing at least 50% grey matter. To prevent outlier voxels from unduly influencing mean results, voxels with calibration constant M (representing the maximum theoretically possible increase in BOLD signal) outside the range 0–0.3, fractional flow changes to hypercapnia outside the range 0–4, or OEF outside the range 0–100% were excluded from relevant means.

To assess the correlations between MRI and PET measures of CBF, OEF and $CMRO_2$, the Pearson product-moment correlation coefficients (r) and the corresponding p-values were calculated. In addition, two-tailed paired Student's t-tests were performed to test for significant differences between the modalities. In both cases the significance level was set at $p < 0.05$.

6.3 Results

A summary of the results obtained may be found in table 6.1, and example images from two representative subjects are shown in figure 6.1. In general, MRI and PET images of CBF showed very similar features. Because ASL is limited to areas with relatively early blood arrival times, there was a greater contrast between grey and white matter in ASL compared with PET. A significant correlation was observed between grey matter CBF as measured by the two modalities (figure 6.2, Pearson coefficient $r = 0.68$, $p = 0.0071$), with no significant difference in mean values (Student's $p = 0.27$). One subject was excluded from the group analysis of CBF (subject 3, marked by $\times$ on figure 6.2) due to an abnormally high PET result.

Values of OEF as measured by MRI were unexpectedly low in this study (mean $21.4 \pm 2.0\%$ compared to 44.4 ± 6.6 for PET, $p < 0.001$). Two subjects (9 and 11) showed very small changes in both oxygen and CO_2 end-tidal measures during the MRI paradigm, resulting in very low MRI OEF estimates and CBF changes. It is hypothesised that this was due to poor cannula placement or very shallow breathing. These subjects were excluded from OEF group analysis. As displayed in figure 6.3, no correlation was observed between MRI and PET measures of OEF (Pearson coefficient $r = 0.36$, $p = 0.23$).

$CMRO_2$ was calculated from CBF and OEF according to equation 6.5 and is included here for completeness. Any subjects excluded in CBF or OEF analysis were also excluded for $CMRO_2$. No correlation was observed between the

Table 6.1: Summary of grey matter average results. Outlier results are shown in brackets and were not included in the relevant means and standard deviations. CBF is in units ml/100 g/min, $CMRO_2$ in μmol/100 g/min.

Subject	Age	Gender	PET CBF	MRI CBF	PET OEF	MRI OEF	PET $CMRO_2$	MRI $CMRO_2$
1	43	M	39.8	35.7	50.5	25.0	178.0	80.1
2	26	M	54.8	47.3	45.1	24.2	190.1	95.0
3	50	F	(85.3)	52.8	32.3	20.5	(191.4)	75.1
4	44	M	41.9	39.9	47.5	23.9	167.8	82.5
5	27	M	49.0	53.8	37.7	19.0	146.4	82.9
6	25	M	51.5	44.9	41.1	19.9	176.1	76.5
7	45	M	43.4	45.7	50.5	19.0	169.9	67.8
8	46	F	52.2	59.9	44.1	22.1	154.1	86.9
9	27	M	31.8	42.9	58.0	(17.8)	154.9	(65.1)
10	57	F	59.2	54.9	34.8	20.2	148.9	79.3
11	26	M	59.4	61.4	45.7	(17.8)	198.2	(77.8)
12	26	M	50.0	49.9	39.3	22.4	157.5	86.1
13	33	M	37.3	42.4	45.4	21.4	147.9	78.8
14	34	M	34.2	38.1	49.5	20.6	137.4	65.5
15	34	M	46.8	65.0	44.4	19.5	144.2	86.8
mean ± std	36 ± 10		46.5 ± 8.8	49.0 ± 8.8	44.4 ± 6.6	21.4 ± 2.0	162.2 ± 18.2	80.3 ± 8.0

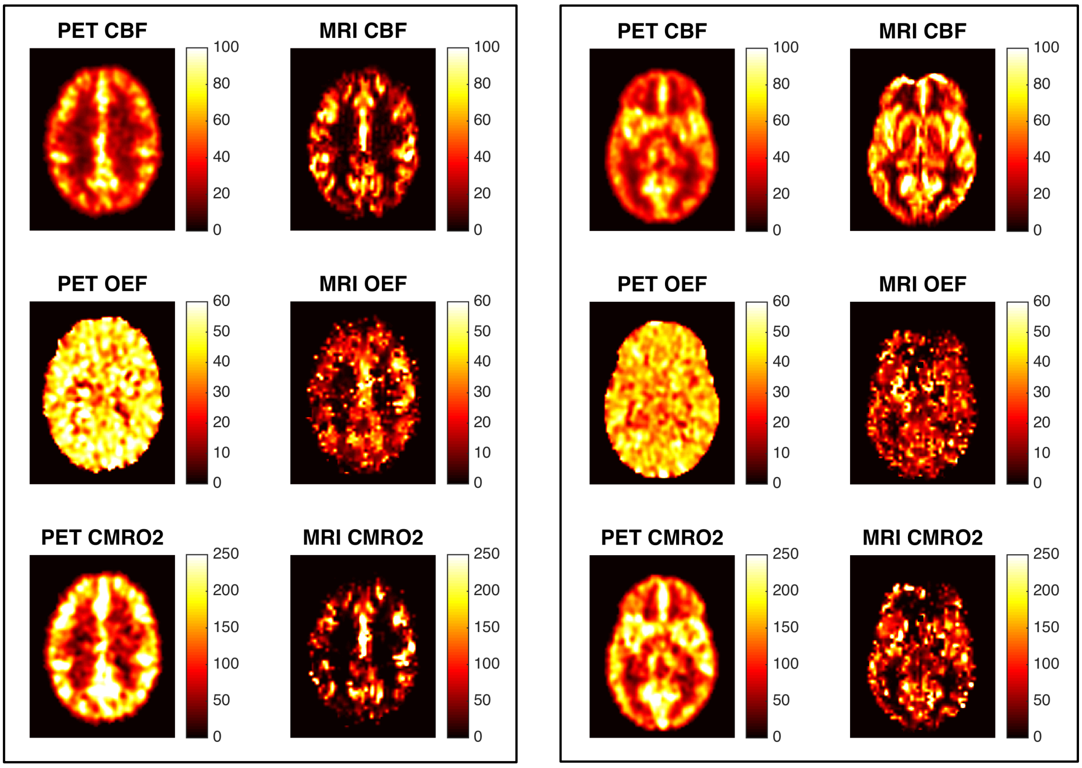

Figure 6.1: Example maps of CBF, OEF and CMRO$_2$ for both imaging modalities in 2 representative subjects (subjects 2 and 12). Units of CBF are ml/100 g/min, OEF is given as a percentage, and CMRO$_2$ is in μmol/100 g/min.

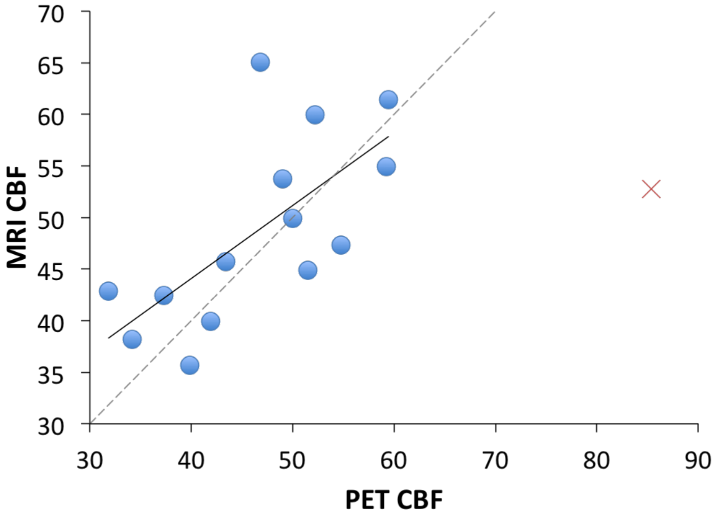

Figure 6.2: Correlation between grey matter CBF as measured by MRI and PET. The outlier (subject 3) is represented by a red cross and excluded from the fitting. The solid line is the line of best fit; for reference, the identity line is also shown (grey dashed line). Pearson coefficient $r = 0.68$, $p = 0.0071$; Student's $p = 0.27$ found for differences between MRI and PET.

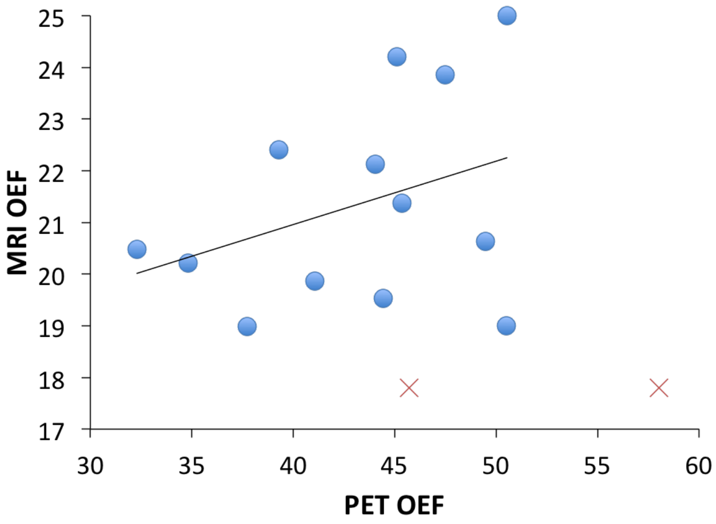

Figure 6.3: Correlation between grey matter OEF as measured by MRI and PET. Outliers (subjects 9 and 11) are shown as red crosses and excluded from the fitting. Pearson coefficient $r = 0.36$, $p = 0.23$; Student's $p < 0.001$ found for differences between MRI and PET.

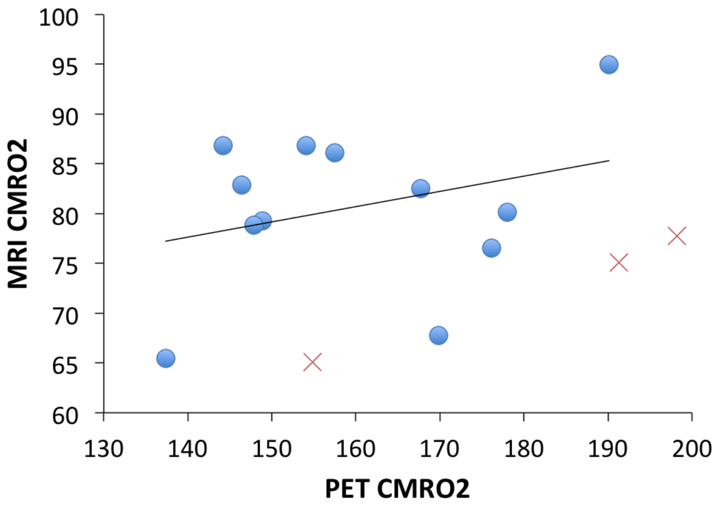

Figure 6.4: Correlation between grey matter $CMRO_2$ as measured by MRI and PET. Outliers (subjects 3, 9 and 11) are shown as red crosses and excluded from the fitting. Pearson coefficient $r = 0.30$, $p = 0.34$; Student's $p < 0.001$ found for differences between MRI and PET.

two modalities (figure 6.4, Pearson $r = 0.30$, $p = 0.34$), but MRI results were significantly lower than PET (Student's $p < 0.001$).

Table 6.2 provides additional information on intermediate results for the gas-calibrated MRI method. These are given in native (low-resolution) space, to avoid any potential registration issues. Histograms for these parameters for a single subject (subject 12) are shown in figure 6.5; figure 6.6 shows similar histograms for the same subject in structural space.

Table 6.2: Table of intermediate calibrated MRI results, given for grey matter in native MR space. Outlier results are shown in brackets and were not included in the relevant means and standard deviations. Resting CBF is in units ml/100 g/min, CBF to CO_2 is given relative to baseline with 1 equal to no change, M is given as a fraction, OEF as a percentage and $CMRO_2$ in units μmol/100 g/min.

Subject	resting CBF	CBF to CO_2	M	OEF	$CMRO_2$
1	40.1	1.76	0.051	27.3	96.6
2	52.2	1.51	0.043	25.0	110.1
3	58.7	1.38	0.051	19.4	81.0
4	41.7	1.45	0.050	26.3	100.5
5	54.5	1.38	0.043	13.2	62.8
6	48.8	1.34	0.073	18.7	79.2
7	48.3	1.41	0.050	15.6	61.0
8	68.3	1.49	0.052	22.1	103.8
9	51.4	(1.21)	(0.040)	(8.4)	(38.7)
10	59.6	1.42	0.058	18.0	80.9
11	66.0	(1.25)	(0.044)	(13.6)	(67.2)
12	57.5	1.32	0.061	22.9	102.6
13	43.9	1.41	0.033	19.3	79.7
14	41.8	1.25	0.052	18.4	65.9
15	65.0	1.38	0.051	17.2	80.0
mean ± std	53.2 ± 9.2	1.42 ± 0.12	0.051 ± 0.010	20.3 ± 4.2	84.9 ± 16.4

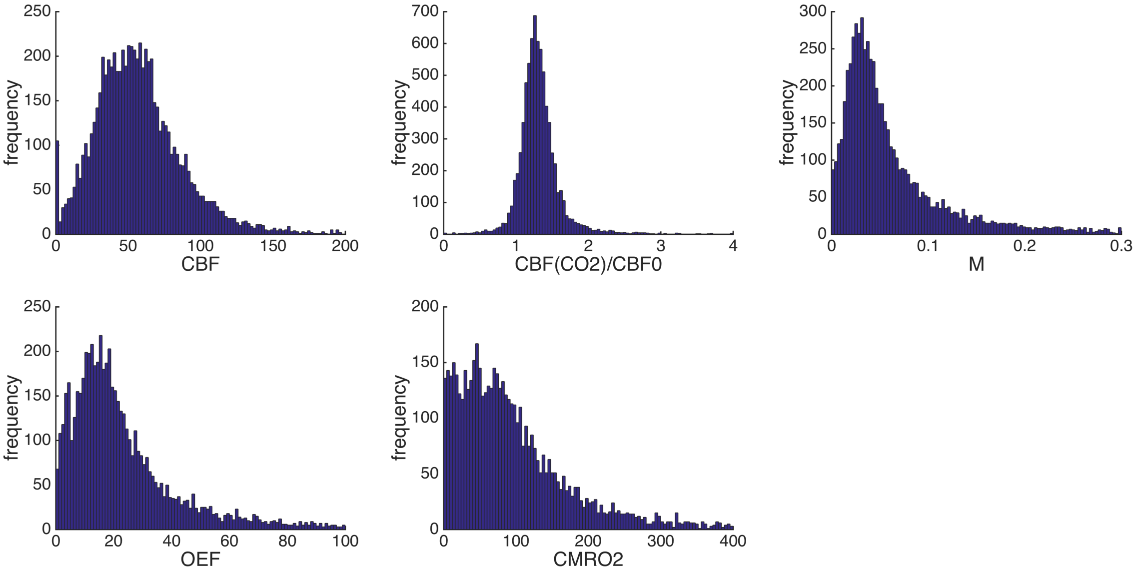

Figure 6.5: Histograms showing the distribution of resting CBF, CBF response to hypercapnia, M, OEF and $CMRO_2$ values for subject 12 within grey matter masks in native MRI space.

6.4 Discussion

Resting grey matter blood flow as measured by the two modalities (multi-PLD PCASL MRI and $H_2{}^{15}O$ PET) were significantly correlated, in good agreement with recent reports from other groups [113, 114]. However, both OEF and $CMRO_2$ were significantly underestimated by the calibrated MRI method, and failed to correlate with the gold standard PET results.

To investigate possible causes for this large discrepancy, intermediate results for the calibrated MRI model (in native MRI space) were more closely inspected. The M values observed (0.051 ± 0.010) agree fairly well with literature values, for example De Vis *et al.* recorded values of 0.043 ± 0.014 in young volunteers and 0.034 ± 0.010 in older subjects (BOLD TE = 36 ms) [115], Bulte *et al.* recorded 0.062 ± 0.010 (TE = 22 ms) [1], Gauthier *et al.* recorded 0.060 ± 0.007 (TE = 30 ms) [2] and Wise *et al.* recorded 0.069 ± 0.025 (TE = 29 ms) [3]. However, these studies reported mean OEF values between 35 and 47%, which

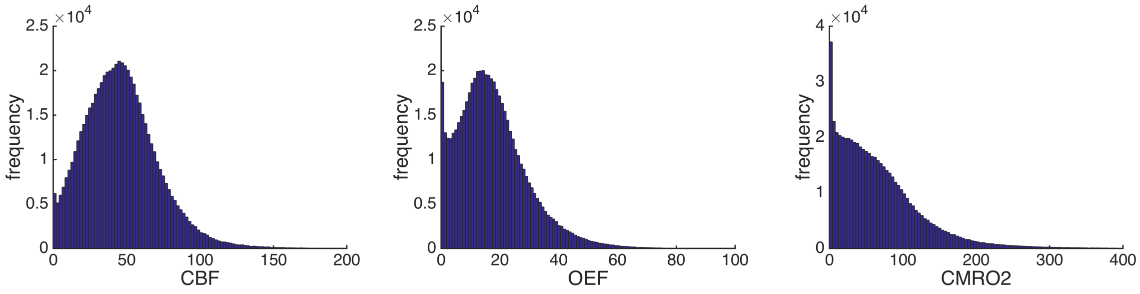

(a) MRI results, GM mask with condition $0 \leq \text{OEF} \leq 100$

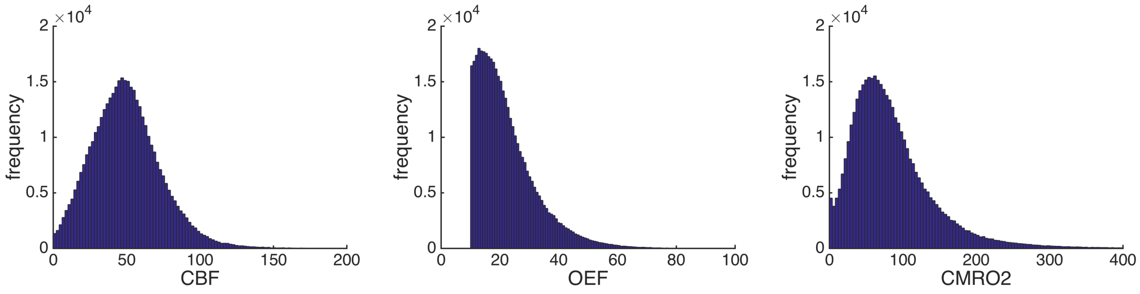

(b) MRI results, GM mask with condition $10 \leq \text{OEF} \leq 100$

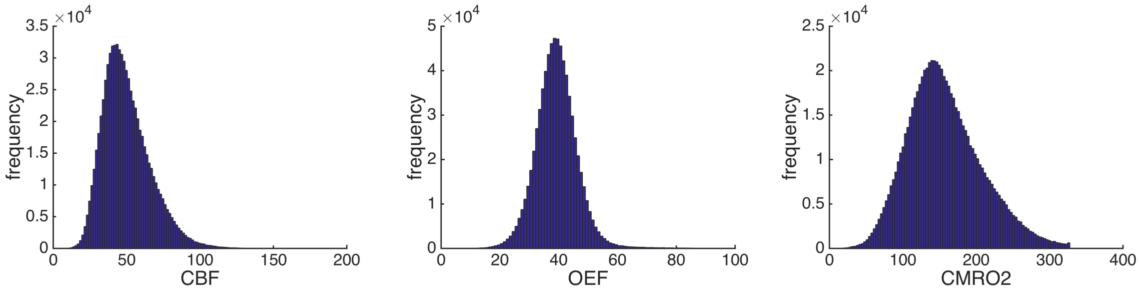

(c) PET results, GM mask with condition $0 \leq \text{OEF} \leq 100$

Figure 6.6: Histograms showing the distribution of CBF, OEF and CMRO$_2$ values for subject 12 within grey matter masks in structural space.

are clearly much higher than those observed in the current study.

Histograms in figure 6.5 show that whilst the resting CBF and CBF(CO_2)/CBF_0 distributions are broadly Gaussian in shape, the distributions for M, OEF and $CMRO_2$ are distinctly more skewed. After registration into structural space, the histograms became noticeably smoother (figure 6.6(a)), with a higher proportion of voxels at very low value. This is particularly noticeable in the histogram for $CMRO_2$, and is thought to be an artefact of partial voluming around the edges of grey matter. To prevent these voxels from artificially lowering the mean, voxels with an OEF of less than 10% were removed from the structural grey matter masks (see figure 6.6(b)). Although the resulting distributions look somewhat similar to those obtained from PET scans (figure 6.6(c)), the OEF peak in particular is clearly offset. The mean OEF for this subject is 22.4%; however, from the histogram in figure 6.6(b), the mode is actually nearer 15%.

ASL in general is known to suffer from low SNR, as it is a signal subtraction technique. The resting CBF maps were calculated after averaging more than 6 minutes of data acquisition; however ASL SNR was anticipated to be a limiting factor for the functional scan. In this study a double excitation sequence was implemented, as this has been shown to increase CNR compared to the dual echo technique [29], and background suppression was turned off to preserve BOLD contrast. Although the latter has been common practice in the past [116–118], it has recently been shown to be sub-optimal as it significantly reduces ASL SNR [25]. Furthermore, if cardiac traces were recorded during the scans, it might be possible to regress out some of the physiological noise, leading to better fits for the explanatory variables of interest (i.e. ASL and BOLD responses to respiratory stimuli).

In the calculation of OEF from MRI data, it was assumed that $CMRO_2$ is unaffected by mild hypercapnia. Although supported by several studies [44,102], this remains a point of debate, with some groups reporting decreased metabolism during hypercapnia [119]. A second assumption made in this study was that there was no change in CBF during hyperoxia. This is not strictly true; Bulte *et al.* measured a 3% reduction in CBF during 40% inspired oxygen, and a 4% reduction during 60% inspired oxygen [120]. However, as the calibrated MRI model is very sensitive to this parameter [121], and particularly as OEF was calculated on a voxelwise basis, the SNR of ASL data once again became the limiting factor. The assumption of constant CBF during periods of hyperoxia avoided the need to incorporate ratios of CBF that were considered to likely be dominated by noise. It is interesting to note that according to the error analysis carried out by De Vis *et al.* [121], an overestimation of CBF during hyperoxia actually leads to a positive error in OEF; thus this assumption is very unlikely to have caused the low OEF results that were observed.

Past studies which employed closely fitted gas masks for delivery of gases led to a significant fraction of volunteers complaining of air hunger, resulting in a relatively high dropout rate. For this study, a nasal cannula gas delivery method was chosen to improve subject comfort, and all subjects completed the scans without problem. However despite using a dual cannula, capable of delivering gas mixtures and simultaneously monitoring gas composition, the design of the cannula used in the present study caused inflowing gas to be channelled directly over the sampling port, leading to significant contamination of the respiratory trace (see figure 6.7 for an example). The contamination was most severe at periods in the breathing cycle with the lowest expiratory pressure, which unfortunately made it impossible to accurately determine end-tidal measures for the subjects. This made it difficult to know whether they reached the targeted end-tidal gas concentrations, and precluded the use of individual end-tidal time courses to model MR signal responses via the generalised linear

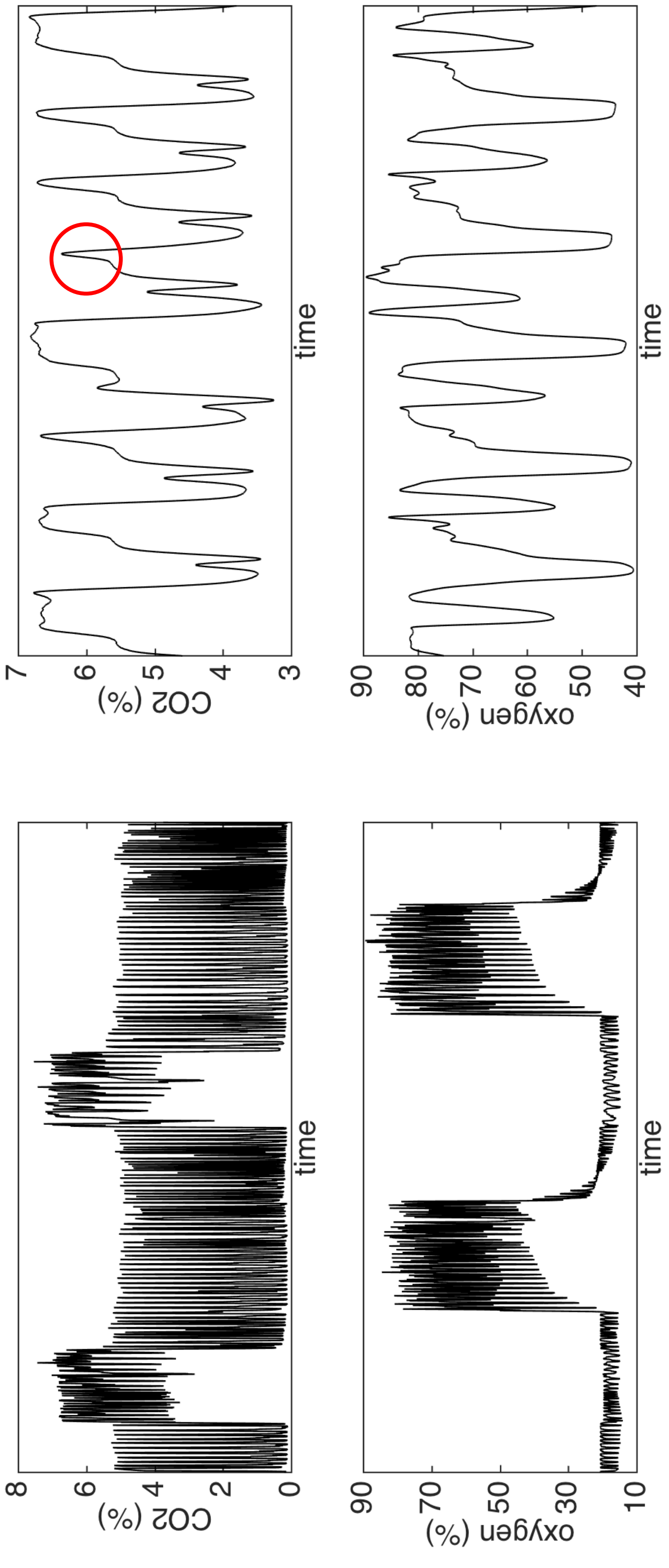

Figure 6.7: Respiratory traces as sampled from the nasal cannula during the entire functional scan (left) and just a few breaths (right). The red circle highlights the effect of contamination from the delivered gas mixture, which conceals the true end-tidal value. All traces shown are taken from subject 2.

model (as implemented in FEAT).

As discussed in section 4.5.2, the criteria for defining an ROI can have a significant impact on reported results. For a fairer comparison, both MRI and PET results were registered to structural MRI space, and an independent grey matter mask was applied, derived from the results of a separate scan. To account for imperfect registration, partial voluming effects and noise, a few additional voxel exclusion criteria were added, as described in section 6.2.5. OEF voxels less than 0 and greater than 100% were excluded as unphysiological for both modalities, in keeping with the calibrated MRI literature. Given that the population mean OEF of 44 ± 6% [100] is close to halfway between these extremes, care must be taken to ensure that signals going into the calibrated MRI model are not excessively noisy, as one would expect an entirely random distribution to yield an apparent mean OEF of 50% with these exclusion criteria. On the other hand, stricter criteria – such as including only voxels with significant ASL and BOLD responses to one or both stimuli – may provide more reliable ROI results, but exclude too many voxels to provide any useful maps. Finding a balance between these concerns is clearly an important challenge in any calibrated MRI study.

6.4.1 Comparison to Near-Infrared Spectroscopy

It is interesting to note that no correlation was found between NIRS-derived OEF and PET results [122] or MRI results (data not shown). NIRS devices are routinely and reliably used to monitor changes in S_tO_2 during interventions such as surgery [53, 54], and have been used to demonstrate that MR-derived S_aO_2, ASL and BOLD signal changes during a hypercapnic challenge correlate strongly with underlying changes in oxygen saturation [123]. However, in terms of absolute values, NIRS is strongly affected both by inter-subject variations in arterial/venous blood fractions, and by the amount of extracerebral tissue (such as skin and skull) between the sensor and brain tissue, neither of which can be easily measured. As a result, values of NIRS SO_2 and OEF should not be considered quantitative as they are susceptible to significant systematic offsets.

6.5 Conclusions

In conclusion, no significant correlation was observed between calibrated MRI and PET measures of OEF and $CMRO_2$. It is difficult to know whether this is due to shortcomings of this young MR method, poor SNR of functional ASL, or insufficient delivery of gas stimuli during the functional MRI scan. This demonstrates that significant improvements are still required for the calibrated MRI method, and that it is not yet robust enough to begin replacing PET procedures. Potential future improvements to the implementation of the MRI method include use of background suppression during the functional scan, physiological noise monitoring, and delivering gases through a closed gas mask, which may allow for individually optimised FEAT modelling as well as more robust gas delivery.

7

A Study of Methodological Considerations for Calibrated MRI

7.1 Introduction

The results presented in Chapter 6 are somewhat disappointing, and raise important questions for the calibrated MRI method. It is clear that ASL in particular suffers from low SNR, which can lead to errors when applying the calibrated MRI model, particularly when this is done on a voxelwise basis to create maps of OEF and $CMRO_2$. The follow-up study presented in this chapter was designed to look into the effects of background suppression, different gas delivery methods, use of end-tidal respiratory traces as analysis regressors, and physiological noise modelling, to elucidate their relative importance and impact upon resulting images of cerebral metabolism.

7.2 Methods

Six subjects (one female, mean age 31 ± 5 years) were scanned on a 3 T Siemens Verio scanner with a 32-channel head coil. The scan protocol was as described in section 6.2.1, with the following adaptations: (1) a sixth PLD time (1500 ms) was added for the resting ASL scan; and (2) a gas mask (8940 series, Hans Rudolph Inc., Kansas City, MO, USA) was used for delivery in place of a nasal cannula, in conjunction with a non-rebreathing manual gas delivery circuit. Gas mixtures of 10% CO_2/21% oxygen/balance nitrogen, 100% oxygen, and medical air (21% oxygen/balance nitrogen) were manually controlled to administer periods of air, stimuli of 5% inspired CO_2 and stimuli of 50% inspired oxygen. A total delivered gas flow of 25 l/min was maintained throughout, and gas composition was monitored with a smaller nasal cannula (CO2 Monitoring Adult Nasal Cannula, Flexicare, Mountain Ash, UK) connected to a Gas Analyzer and Powerlab (ADInstruments, Dunedin, New Zealand). The functional scan (ASL/BOLD double excitation with periods of hypercapnia and hyperoxia) was run twice, once with background suppression turned on, and once off. Cardiac phase and breathing were monitored and recorded throughout via a finger clip oximeter and respiratory bellows respectively (Biopac Systems, Goleta, CA, USA) for physiological noise modelling. Haemoglobin levels were measured in each subject using a Pronto-7 pulse oximeter (Masimo, Irvine, CA, USA) immediately following the scans.

Data preprocessing and basic analysis were identical to that described in section 6.2.2. Briefly, this included correcting for motion and field inhomogeneities, applying a 5 mm Gaussian smoothing kernel and a highpass filter, and calculating ASL and BOLD responses to respiratory stimuli using a general linear model (GLM) in FEAT. Physiological noise regressors were created using the

FSL PNM tool [124]. Personalised end-tidal (ET) oxygen and CO_2 traces were created for each scan from the timecourses recorded on the Powerlab, and qualitatively compared to the 'average' modelled ET traces, which consisted of the sharp-onset blocks of delivered gas stimuli convolved with a gamma function (mean lag/stddev 30/10 s for CO_2 and 60/60 s for oxygen, determined empirically with reference to subjects' respiratory traces). FEAT and MATLAB analysis was carried out on data with and without background suppression, using both modelled and personalised ET traces. The cases that were expected to yield the highest SNR (background suppression on, modelled and observed ET traces) were analysed again with the inclusion of physiological noise regressors, resulting in a total of 6 analysis variants per subject.

Grey matter ROIs were defined by thresholding the resting ASL perfusion map at the 45^{th} percentile after brain extraction, resulting in a mask containing the 55% of voxels with the highest resting CBF [125]. This avoided the need to register between low and high resolution scans. Voxels outside the ranges $0 < M < 0.3$, $0 < \text{OEF} < 100\%$ and $0 < \text{CBF}(\text{CO}_2)/\text{CBF}_0 < 4$ were excluded from the masks for being excessively noisy.

7.3 Results

All subjects completed the scans successfully, although most reported mild discomfort and air hunger due to the closely fitting masks. Measured haemoglobin concentrations were 16.4 ± 0.9 g/dL.

Group mean results for all 6 analysis variants are shown in table 7.1. Figure 7.1 displays the modelled end-tidal traces for CO_2 and oxygen in black, and the personalised traces for all 6 subjects below. Scales are not shown (all traces were normalised before being used as explanatory variables in FEAT), but end-tidal

Table 7.1: Summary of results, showing the effects of background suppression (bgs), physiological noise monitoring (PNM) and using personalised end-tidal (ET) traces within FEAT. Numbers are given as mean ± standard deviation across all 6 subjects within their respective grey matter masks. Units for resting CBF (CBF$_0$) are ml/100 g/min, CBF to CO$_2$ is given relative to baseline (no change = 1), BOLD responses are fractional compared to baseline (no change = 0), M is given as a fraction, OEF as a percentage and CMRO$_2$ is in μmol/100 g/min.

	modelled ET				**personalised ET**			
bgs off	CBF$_0$	56.8	±	6.4	CBF$_0$	56.6	±	6.5
	CBF to CO$_2$	1.66	±	0.11	CBF to CO$_2$	1.57	±	0.14
	BOLD to CO$_2$	0.022	±	0.004	BOLD to CO$_2$	0.020	±	0.005
	BOLD to O$_2$	0.012	±	0.006	BOLD to O$_2$	0.016	±	0.005
	M	0.069	±	0.006	M	0.069	±	0.007
	OEF	32.8	±	9.1	OEF	28.5	±	7.2
	CMRO$_2$	174.2	±	55.6	CMRO$_2$	150.6	±	44.5
bgs on	CBF$_0$	56.7	±	7.5	CBF$_0$	56.3	±	7.8
	CBF to CO$_2$	1.59	±	0.15	CBF to CO$_2$	1.63	±	0.26
	BOLD to CO$_2$	0.019	±	0.005	BOLD to CO$_2$	0.020	±	0.005
	BOLD to O$_2$	0.014	±	0.006	BOLD to O$_2$	0.014	±	0.004
	M	0.058	±	0.010	M	0.061	±	0.007
	OEF	25.7	±	6.4	OEF	26.6	±	6.1
	CMRO$_2$	132.3	±	23.4	CMRO$_2$	135.0	±	20.9
bgs on + PNM	CBF$_0$	56.9	±	7.4	CBF$_0$	56.3	±	7.3
	CBF to CO$_2$	1.60	±	0.15	CBF to CO$_2$	1.76	±	0.23
	BOLD to CO$_2$	0.019	±	0.005	BOLD to CO$_2$	0.026	±	0.008
	BOLD to O$_2$	0.014	±	0.005	BOLD to O$_2$	0.016	±	0.004
	M	0.059	±	0.010	M	0.069	±	0.008
	OEF	25.9	±	6.3	OEF	26.9	±	5.8
	CMRO$_2$	133.2	±	23.3	CMRO$_2$	136.6	±	18.3

CO$_2$ ranges were on the order of 1–2%, whereas for oxygen this was approximately 35–40%. The greater dynamic range for oxygen resulted in smoother traces, which more closely matched the model, compared to the CO$_2$ case. Examples of GLM fits are shown in figure 7.2. The addition of physiological noise parameters as confounds did not lead to any improvements in the quality of the fits, suggesting that scanner noise is a greater concern than physiological noise in this sequence.

Figure 7.3 shows maps of resting CBF (from the multi-PLD scan), the grey

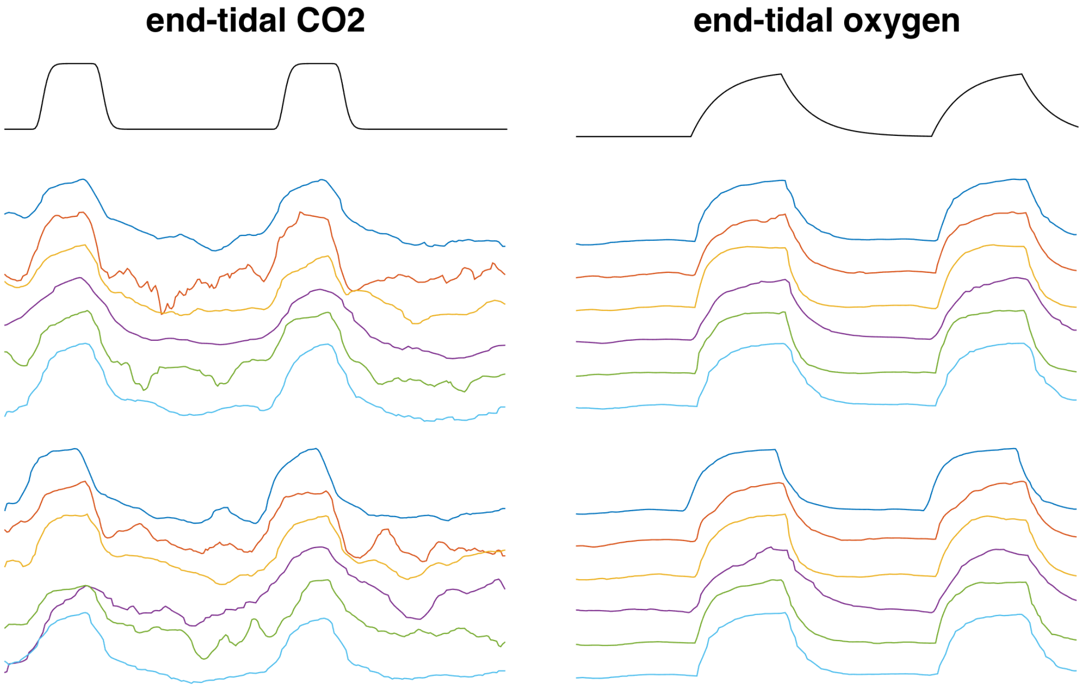

Figure 7.1: End-tidal traces for CO_2 (left) and oxygen (right). The black line shows the modelled trace, the remaining traces show end-tidals for all subjects (in order, subject 1 at the top) for the case where background suppression was turned off (top group) and on (bottom group).

matter mask, CBF and BOLD responses to respiratory challenges, M, OEF and $CMRO_2$ for a single slice in one subject. In order to visualise the effects of using background suppression and personalised end-tidal traces in the analysis, OEF maps from all subjects are shown in figure 7.4. In general, turning on background suppression resulted in smoother, less noisy images, with fewer voxels outside the physiological range (0–100% for OEF). Personalised end-tidal traces led to some visual improvement in a few of the subjects, again mostly in the form of fewer unphysiological voxels. It is interesting to note that the greatest improvements were generally observed in cases where the personalised end-tidal traces were smoothest, for example in the non-background suppressed scans for subjects 3 and 5 (yellow and green in figure 7.1).

Figure 7.5 shows histograms of CBF response to hypercapnia, M and OEF

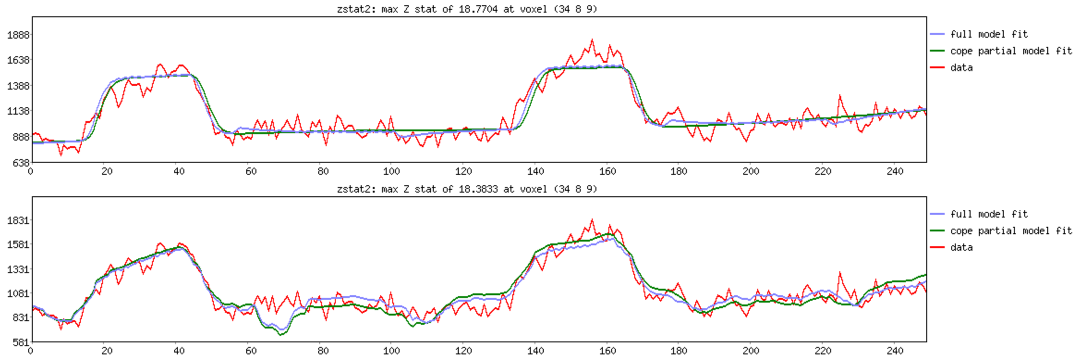

(a) BOLD response to CO_2 using modelled (top) and personalised (bottom) end-tidal time courses. (Background suppression off, no PNM)

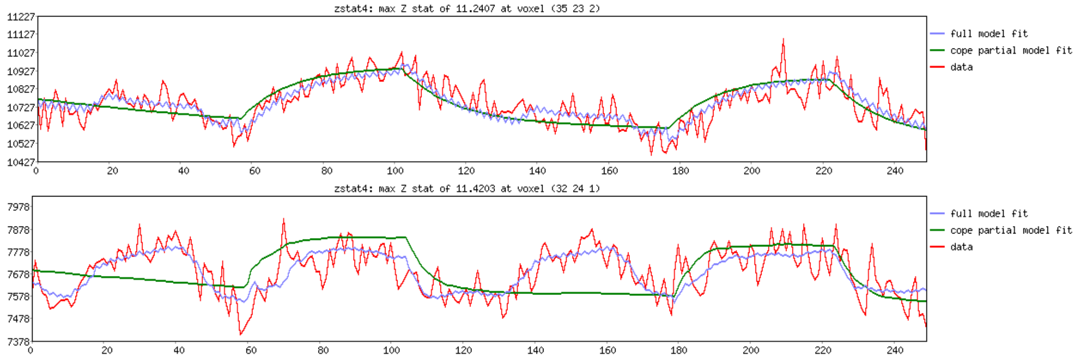

(b) BOLD response to oxygen using modelled (top) and personalised (bottom) end-tidal time courses. (Background suppression off, no PNM)

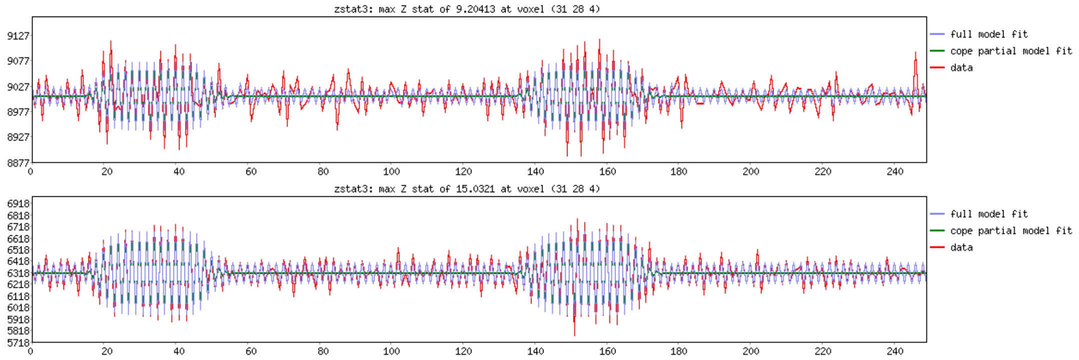

(c) ASL response to CO_2 with background suppression turned off (top) and on (bottom). (Modelled end-tidals, no PNM)

Figure 7.2: Single voxel timecourses from subject 5. The voxels shown are those with the highest z-statistics for the particular contrast. The results of fitting with a generalised linear model (GLM) using FEAT are shown in blue. Including additional explanatory variables for physiological noise modelling (PNM) had no appreciable effect on any of the fits.

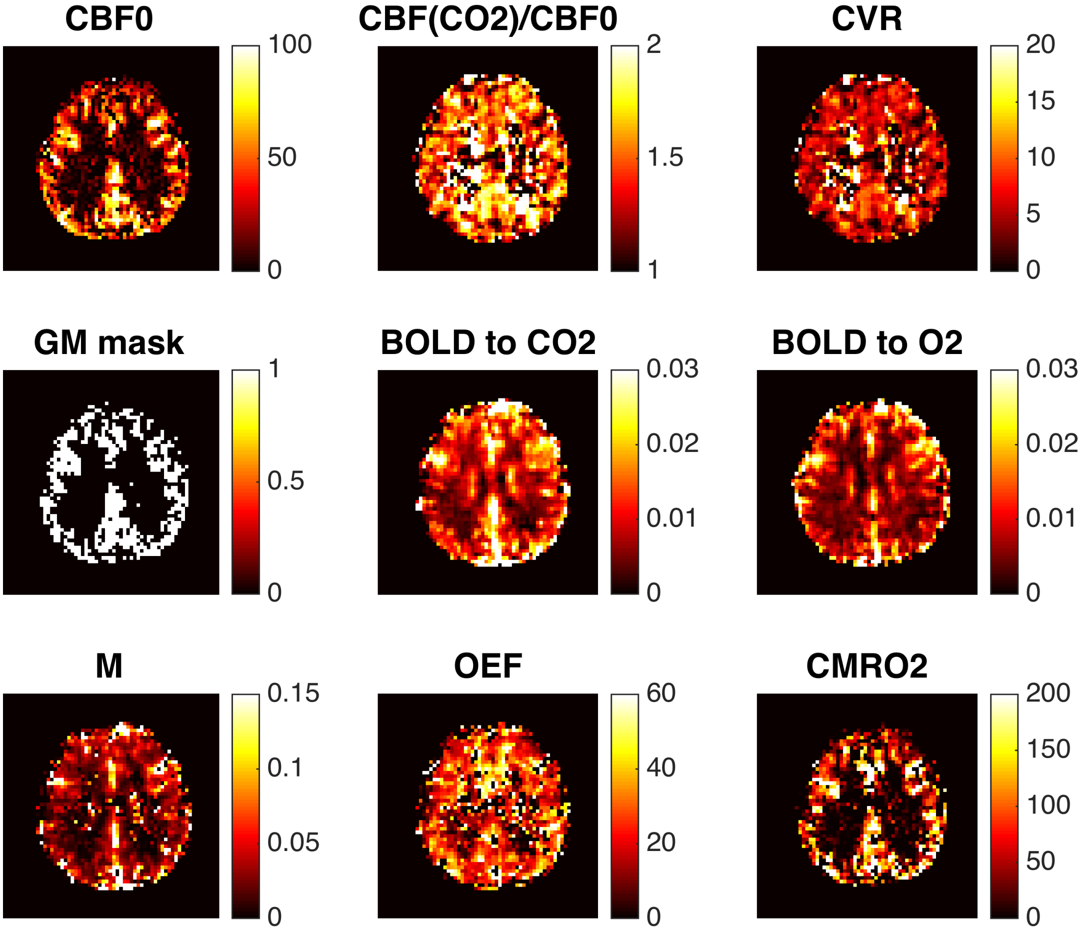

Figure 7.3: Single slice results for subject 5, shown for the case where background suppression was on, personalised end-tidal traces were used and no physiological noise modelling was applied.

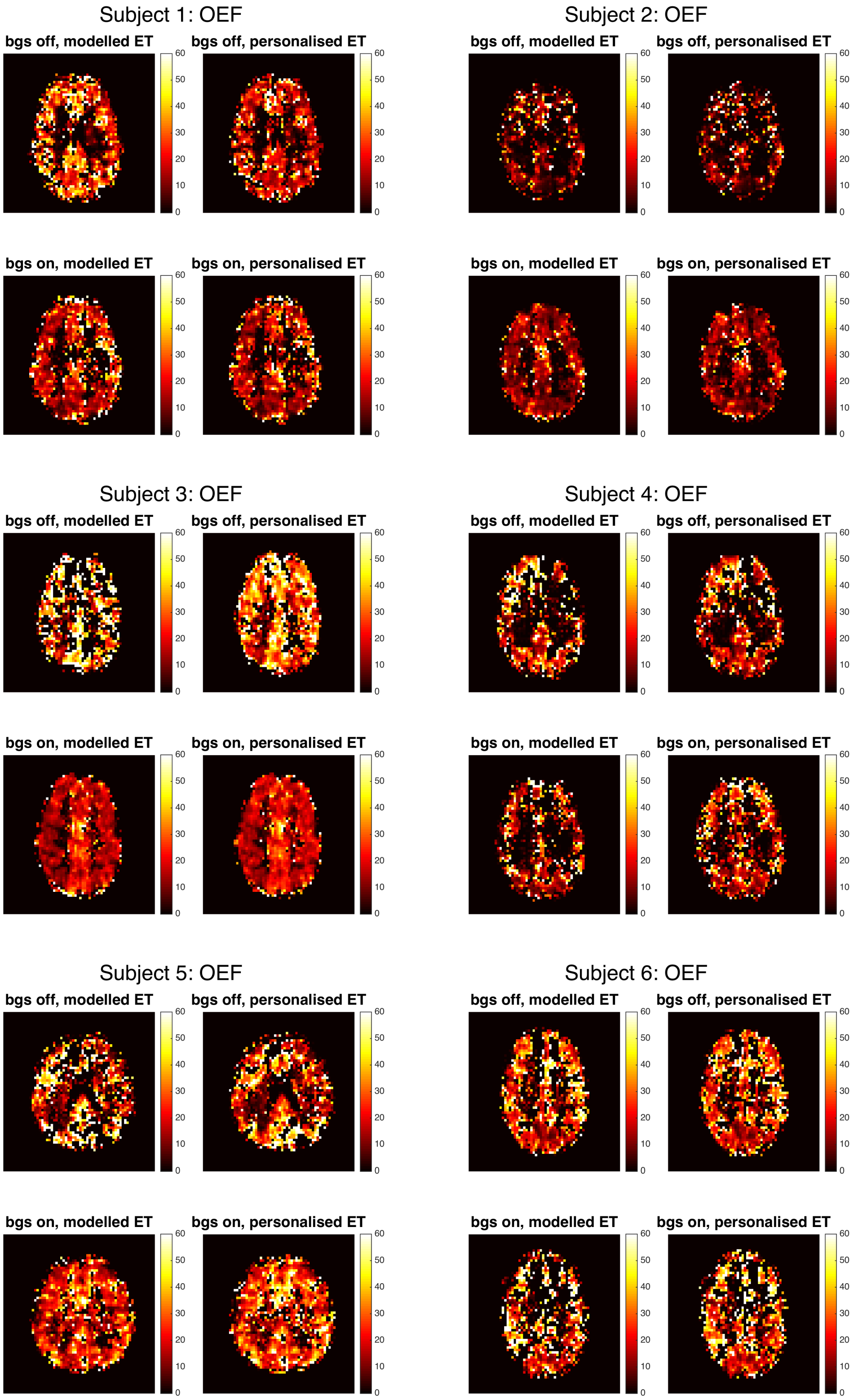

Figure 7.4: Maps of OEF for all 6 subjects, showing the effects of turning on background suppression (bgs) and using personalised end-tidal (ET) traces as inputs for the generalised linear model during analysis.

for one subject. Personalised end-tidal traces worked well with this subject (see subject 5 in figure 7.4), as demonstrated by tighter distributions of $\mathrm{CBF(CO_2)/CBF_0}$ and OEF in figure 7.5(b) compared to (a). Turning on background suppression had an even greater positive effect, further tightening the distributions (figure 7.5(c) and (d)).

7.4 Discussion

This study aimed to investigate the effects of several factors that are known or thought to affect the quality of calibrated MRI data. This includes increasing the SNR of the underlying images (here by background suppression), improving the reliability of delivering respiratory stimuli (for example using a gas mask in place of a nasal cannula) and details on how best to fit data. In the following sections, the reasoning behind several methodological choices is discussed, with respect to both the experimental setup and the analysis procedure.

7.4.1 Choice of Pulse Sequence

Calibrated MRI is unusual in that it requires the near-simultaneous collection of both ASL and BOLD data. As a subtraction technique, ASL suffers from lower SNR, and compromises are often made in order to maximise its contrast-to-noise ratio (CNR). In its earlier implementations, calibrated MRI used a standard ASL sequence with an intermediate echo time of 20–25 ms [1,28]. More recently, dual echo sequences have gained popularity, in which two readouts are acquired following every slice-selective excitation [2, 3]. Here the echo times can be adjusted such that the first readout has a short echo time for higher ASL signal, and the second echo time is optimised for best BOLD contrast. This simultaneously increases SNR of both ASL and BOLD data; however, a

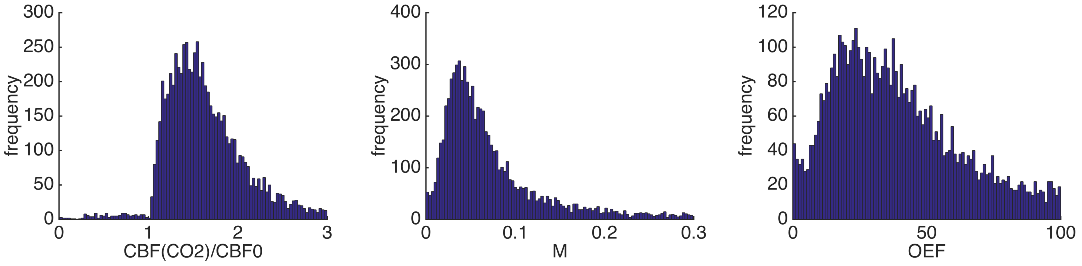

(a) background suppression off, modelled end-tidals, no PNM

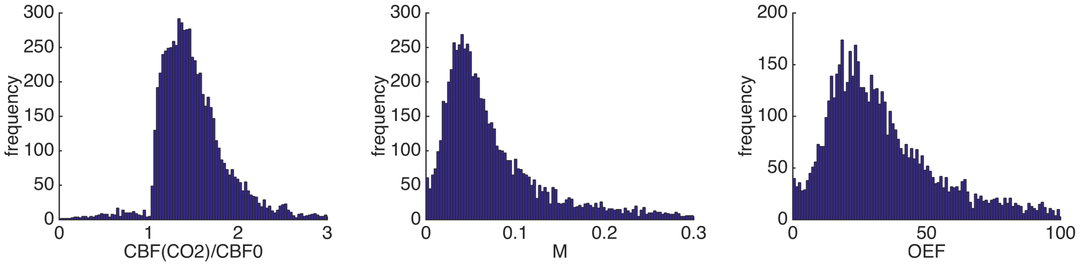

(b) background suppression off, personalised end-tidals, no PNM

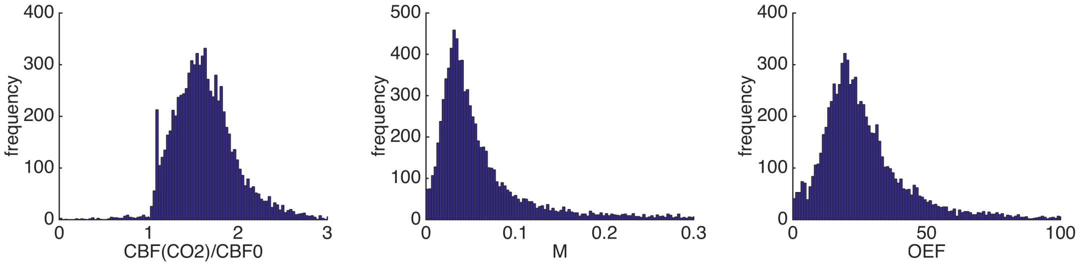

(c) background suppression on, modelled end-tidals, no PNM

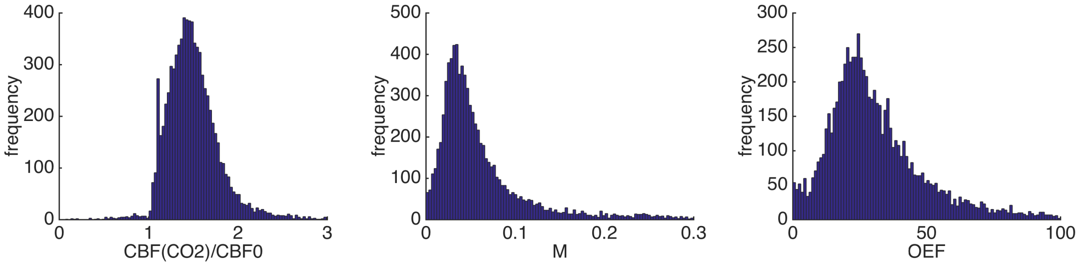

(d) background suppression on, personalised end-tidals, no PNM

Figure 7.5: Histograms showing the distribution of CBF response to hypercapnia, M and OEF values for subject 5 within grey matter.

disadvantage of the method is that the time required for each readout more than doubles. This can have a detrimental effect on ASL images for slices higher up in the brain, as the time between inversion and imaging of the spins increases for each slice. For PCASL the PLD is, by convention, defined as the time between the end of the labelling period and the excitation of the first imaging slice [14]; however, for the same PLD, a dual echo sequence will result in longer 'effective' PLDs for the higher slices than a single echo sequence.

An alternative method used for this study that combines the advantages of both techniques described above is the 'double excitation' method. Here, in each TR, all of the slices are imaged in quick succession with a short echo time (optimised for ASL), and then a second whole-brain readout is acquired (with a second set of excitation pulses and an independent echo time). This allows all the ASL data to be collected as quickly as possible, and also reduces the ASL tag/control contamination in the BOLD signal. The double excitation method has been shown to improve ASL CNR with only a small BOLD CNR penalty [29], which can be further reduced by using an ASL excitation flip angle of 60° instead of 90°. (In the current study a flip angle of 60° was used for both ASL and BOLD readouts. Future implementations of the sequence may allow for different flip angles, as there is no theoretical reason why the BOLD flip angle need be reduced from 90°.) The only disadvantage of the double excitation method is a slightly reduced slice coverage for the same TR, as the 'dead time' between excitation and BOLD readouts are no longer being filled by ASL readouts.

7.4.2 Background Suppression

Background suppression uses additional inversion pulses played out during the PLD to suppress signal from static tissue. After subtraction, the ASL signal difference arising from tagged blood should remain unaffected, but the reduction in static signal magnitude can lead to a considerable increase in SNR. The use of background suppression is always recommended in standard ASL applications [14], but as it affects tissue signal so strongly, it has generally been avoided in calibrated MRI experiments where BOLD signal is also of interest [116–118].

However, recent work by Ghariq *et al.* has demonstrated that the benefits to ASL SNR outweigh any losses in BOLD CNR [25], supporting the use of background suppression for all ASL acquisitions. Furthermore, it is expected that any negative effects on BOLD CNR will be reduced in the double excitation sequence (compared to dual echo), as there is a longer gap between the inversion and the BOLD excitation pulses.

The results of this study confirm that the use of background suppression is highly desirable. ASL timecourses were visibly less noisy, resulting in higher z-statistics after GLM fitting (see figure 7.2(c)), while BOLD contrast was not noticeably reduced. Although mean OEF values actually decreased from 32.8 ± 9.1 to $25.7 \pm 6.4\%$ with background suppression, OEF maps were typically less noisy (figure 7.4) and histograms showed narrower distributions (figure 7.5).

7.4.3 Gas Delivery Methods

The gas delivery circuit used in this study incorporated a short mixing tube, a filter, a close-fitting mask, a one-way valve for exhalation and a 1 m-long piece of tubing as a reservoir. A thin nasal cannula was worn beneath the mask for monitoring the gas composition within the mask. This led to varying degrees of leakage for different subjects, which was reduced by plugging gaps with surgical glove material. Surgical tape may also be used to ensure a tight fit.

The use of a gas mask produced fairly reliable delivery of respiratory stimuli, as monitored with a Powerlab. End-tidal timecourses were created from the recorded traces, as shown in figure 7.1. However, subjects frequently report feelings of air hunger with this setup, presumably because of the increased resistance to breathing caused by the filter. Although all volunteers successfully completed the protocol in the current study, past experience with a similar setup resulted in multiple subjects withdrawing from experiments following bench testing or during the scan itself. A further limitation is that it can be very difficult to get an adequate seal on the mask, particularly for people with petite faces or significant facial hair.

An alternative method for delivering respiratory stimuli is the use of a dual-purpose nasal cannula, capable of simultaneous delivery and sampling of gases. This was the method used in Chapter 6. It is very well-tolerated by subjects, but suffers from a few limitations. Because gases are always mixed with room air upon delivery, the highest oxygen stimulus that can be reached is approximately 50%. The quality of gas monitoring attainable depends on the precise location of the sampling port within the cannula; sometimes these are placed to be primarily sensitive to the delivered gas mixture, rather than to the exhaled gas, leading to significant contamination of respiratory traces which become very difficult to interpret (see figure 6.7). It is for this reason that a mask was chosen for the current study.

Both gas delivery methods discussed above are reasonably cheap and easy to set up, making them widely applicable and ideal for groups that do not yet have much experience with respiratory challenges. The high-end solution to delivering reliable, repeatable stimuli is to use a RespirAct (Thornhill Research, Toronto, ON, Canada), a device capable of targeting specified end-tidal values of CO_2 and oxygen simultaneously for the duration of any pre-planned paradigm. This setup uses a sealed gas mask, similar to the setup used in the present study, attached to an automated gas monitoring and blending system. It would be straightforward to use the same target paradigm both for the RespirAct delivery system and as an input for the GLM.

7.4.4 Using the Generalised Linear Model

The crux of the calibrated MRI method lies in the equations described in section 3.3. In order to calculate M and OEF, the relative changes in CBF and BOLD signal first need to be quantified. One method of doing this is to split the timecourse into periods of baseline, hyperoxia and hypercapnia, to average the signals acquired during these times, and then to divide by the baseline value. This relatively simple analysis method requires the removal of data from any transition periods, as the Davis model assumes that a steady state has already been reached and thus is not valid during these periods. It typically takes around 1 minute for a CO_2 stimulus to reach a state of equilibrium and 2 minutes for oxygen, and the same again when returning to normal air breathing. Considering the low SNR of ASL data in particular, discarding such a significant proportion of data seems particularly inefficient. It also limits the paradigms that can be used, as overlapping stimuli cannot readily be separated into multiple components e.g. simultaneous changes in oxygen and CO_2 are difficult to account for.

The current approach uses FEAT, a sophisticated analysis tool that employs a GLM in conjunction with a Bayesian fitting process, allowing complex stimulus paradigms to be modelled and estimating the response magnitudes using all data points available. It also provides voxelwise 'goodness-of-fit' information in the form of z-statistics, which can prove very useful when creating ROIs, particularly in response to functional tasks [60, 126]. Although most commonly used in the analysis of BOLD data, it is equally capable of analysing ASL signals. Full modelling of the tag/control timecourse provided better fits than analysis of

ASL data after subtraction (data not shown), presumably because the Bayesian approach benefits from the increased number of effective time points and any errors in a single noisy datapoint do not propagate to neighbouring points as they would during surround subtraction. Examples of single voxel fits as output by FEAT are shown in figure 7.2.

7.4.5 Personalised End-Tidal Traces

Given the same respiratory paradigm, healthy subjects generally produce qualitatively similar end-tidal partial pressure timecourses for CO_2 and oxygen, as may be seen in figure 7.1. However, variations do arise as a result of differences in depth and rate of breathing, both between subjects and as a result of relaxing or falling asleep during the course of a single scan. Further factors such as lung function may be expected to cause even greater variation within in clinical population. The end-tidal timecourses are assumed to be good indicators of arterial blood partial pressures, and thus be representative of the challenges experienced by subjects' cerebral tissue. However, respiratory traces can be noisy and it is not always trivial – or even possible – to extract end-tidal information from them, as discussed in Chapter 6.

This study did not demonstrate a consistent benefit from respiratory traces, with only a subset of subjects showing any improvement with the inclusion of personalised end-tidal data. The shapes of BOLD responses during hypercapnic stimuli generally more closely matched personalised end-tidal traces (see figure 7.2(a) for an example). However variations during the baseline periods, whether noise or genuine changes in end-tidal values that perhaps did not reach cerebral blood supplies, interfered with the fitting process. Personalised end-tidal oxygen traces appeared smoother and more similar to the modelled trace (compared to CO_2), resulting in similarly good fits for both modelled and personalised FEAT variants. However it is difficult to separate the relative contributions of oxygen and CO_2 fitting, as most voxels show responses to both stimuli (see figure 7.2(b)).

Future studies might benefit from using modelled timecourses for CO_2 and personalised oxygen end-tidals, as the latter introduce less artifactual variability during baseline periods. It may also be possible to extract only select parts of CO_2 end-tidal timecourses for use with FEAT, or to apply variable amount of smoothing to the two contrasts. It should be mentioned that some systems have been developed specifically to independently vary oxygen and CO_2 partial pressures (the RespirAct as mentioned above, or end-tidal forcing techniques [127]), which are able to e.g. maintain consistent partial pressures of CO_2 during periods of hyperoxia.

7.4.6 Physiological Noise Modelling

To date physiological noise modelling has mostly been applied in studies of the spinal cord or brainstem, where CSF pulsation during the cardiac cycle causes particularly large artefacts, and in conjunction with resting state fMRI to identify diverse brain networks. By identifying and removing signal fluctuations caused by respiratory- or cardiac-induced motion, the residual data should be more sensitive to genuine changes in the contrasts of interest.

In terms of the current study, adding nuisance regressors for physiological noise within FEAT led to no improvement in any of the signal fits, and very little change in ROI results (see table 7.1). This suggests that the primary source of noise in the data is of thermal and not of physiological origin. This is perhaps to be expected for ASL, which has a much lower inherent SNR than most MR contrasts, but was equally true for BOLD data in this study. It may be that the remaining signal contribution from alternating tag/control states contained a similar level of noise to that modelled by the PNM tool, negating any potential benefits.

7.4.7 Limitations

This study included only a small number of young, healthy subjects. It is thought that the potential benefits of using personalised end-tidal traces in particular would be most pronounced in subject groups whose physiology is more variable, for example in patients or across a wider range of ages. Ultimately, the decision of whether to use physiological noise modelling or recorded end-tidal traces as part of the data analysis will vary with each study, and practical considerations such as available equipment and more time-consuming data analysis may play an additional role.

7.4.8 Relevance with Respect to MRI–PET Comparison

The OEF values calculated from MRI data in Chapter 6 were extremely low, prompting concern over aspects of the methodology. The most basic analysis variant in the current study was designed to match that in the previous chapter as closely as possible, with background suppression turned off and identical modelled end-tidal traces being used within FEAT. Although different scanner suites were used, both contained Siemens Verio scanners with identical specifications. The only notable difference was the gas delivery method, whereby the cannulae used in Chapter 6 were replaced with gas masks to allow for reliable recording of end-tidal respiratory traces.

Despite taking care to match both imaging and stimulus protocols, the group mean OEF in the present study was 33 ± 9%, compared to the previous value of 20 ± 4%. It seems very improbable that there would be a true variation of this magnitude between two healthy subject groups, so it would appear that the discrepancy was driven purely by the different gas delivery methods. Based on this observation, it is recommended that in future any calibrated MRI studies employing nasal cannulae take particular care to use cannulae capable of reliably monitoring end-tidal traces, or consider using face masks to deliver respiratory stimuli instead. However, although an OEF of 33 ± 9% is in line with previous calibrated MRI results (for example 35 ± 4% [2], 38 ± 14% [1]), it is still somewhat low compared to the 35–50% typically observed by PET [100]. Further work is needed to evaluate whether this is the result of a systematic bias or a deeper underlying issue, perhaps in the assumptions upon which the calibrated MRI model is built.

7.5 Conclusions

Three methods thought to be beneficial for improving CNR and fitting of calibrated MRI data were investigated in this study: the use of background suppression, the recording of individual end-tidal timecourses to create personalised traces for analysis, and the addition of nuisance regressors for physiological noise removal. The greatest improvement was observed with background suppression, which greatly improved the quality of the ASL data acquired and had no notable detrimental effect on BOLD contrast. Personalised end-tidal traces proved useful in a subset of subjects, but did not greatly impact results; however they are expected to lead to greater improvements in subjects with atypical physiology. Finally, no improvements were observed with physiological noise modelling in this study.

8

On the Origins of the IVIM Signal

8.1 Motivation

To date, calibrated MRI techniques have been applied to investigate various aspects of the healthy human brain, both at rest and in response to a range of functional stimuli, but they have rarely been applied in cases of pathology, even within a research setting. At the time of writing, only a single study had applied the method in patients [121]. As discussed in Chapter 6 the technique has yet to be validated against the gold standard of triple oxygen PET or any other independent modality. Beyond this, one potentially limiting factor is the requirement for at least two calibration gas mixtures to be present inside the MRI scanner. However, oxygen is very widely available in a clinical environment, and the stipulation for a hypercapnic gas mixture has not prevented the utilisation of fMRI in mapping cerebrovascular reactivity in patients with a range of steno-occlusive diseases [128, 129].

A more basic limit arising in pathologies is that of long blood arrival times. The ASL signal is fundamentally limited by the T_1 decay of the blood, so that even very long post-label delay times are not able to reliably quantify very slow-moving blood. White matter perfusion is notoriously difficult to measure using ASL [130]; similarly, it is very challenging to obtain perfusion values in areas of cerebral occlusions or in the presence of collateral flow. De Vis *et al.* reported artefacts arising from delayed arrival of arterial blood in 3 out of 11 patients scanned with internal carotid artery occlusions, leading to unreliable estimates of oxygen extraction and consumption [121]. Thus the areas likely to be of greatest interest in the monitoring of oxygen metabolism are simultaneously the areas of least confidence for ASL perfusion measures.

Velocity-selective ASL was developed to overcome this limitation by creating a tagging scheme sensitive to the velocity instead of position of water molecules (see section 2.2.2.4 for more information). However, this technique suffers from even lower SNR than other flavours of ASL, at least for normal arterial arrival times.

Intravoxel incoherent motion (IVIM) is a completely independent approach to measuring blood volume and perfusion in the body. As its name suggests, it relies only on the motion of water molecules within a single voxel, and it should thus be capable of making equally valid measurements throughout the entire vascular network, including within white matter. This benefit may outweigh the method's relative disadvantages compared to ASL (functional imaging would be difficult as a full dataset is required to derive a single perfusion map), whilst still allowing for non-invasive imaging of cerebral perfusion, especially in the presence of very slow-moving blood. The aim of this chapter was to assess the viability of using IVIM to measure resting cerebral perfusion.

8.2 Introduction

Intravoxel incoherent motion was first developed by Le Bihan in the 1980s [131], and is based on the premise that both diffusion and microvascular perfusion result in motion of water molecules in all directions (at the macroscopic scale of a voxel), but at different temporal scales, with water in the capillaries moving more quickly than water in intra-cellular space. This leads to a biexponential model of diffusion signal as a function of b-value, with very low b-values (less than $\sim$100 s/mm^2) exhibiting a greater rate of signal decay due to capillary flow. In addition to the classical diffusion coefficient (D), a 'pseudo-diffusion coefficient' D^* is introduced, along with the fraction of fast-diffusing spins, f_v, which is usually interpreted as the capillary blood volume fraction in each voxel. The product $f_v\, D^*$ is then a measure of perfusion, in units of mm^2/s, which may be converted to traditional CBF units of ml blood/100 g tissue/minute via the following equation [33]:

$$\text{CBF} = \frac{6\,\lambda}{L <l>} f_v\, D^* \tag{8.1}$$

where λ is the fraction of MR-visible water, L is the total length of the capillary network and $<l>$ is the mean capillary length. Capillary lengths cannot be measured non-invasively; they have been shown to vary with age [132] and region [133] within subcortical structures, but appear to be remarkably constant across the cortex [132, 134]. However, they may be expected to vary significantly in cases of pathology. For this reason $f_v\, D^*$ values are not usually converted to traditional perfusion units. The term 'perfusion' will be used throughout this chapter with the understanding that it refers to the pattern of blood flow through the capillaries, and not specifically to the delivery of oxygen or nutrients to the tissue. This is true for both ASL and IVIM imaging.

IVIM has been used to study the liver [135–139], kidney [140–142] and pancreas [143–145] without the need for an injected tracer, which can be particularly valuable in cases where contrast agents are contraindicated. However, its application within the brain has been a subject of controversy for many years [33, 146, 147]. Results can vary significantly depending on the specific fitting algorithm that is used [148], as well as on experimental parameters such as TE [145] and the range of b-values measured [149, 150]. Concerns have also been raised about biases introduced by fitting low SNR data [151,152], and contaminating effects of CSF due to bulk motion during the cardiac cycle or simple partial voluming [153].

Despite these complications, IVIM continues to be applied in the brain as well as numerous abdominal organs. IVIM-derived parameters have shown promise in the characterisation and monitoring of head and neck tumours [154–158]. Going one step further, Federau *et al.* have reported quantitative changes in IVIM perfusion during hypercapnia [159] and visual stimulation [160], despite earlier work failing to achieve this in animal models [161].

The aim of this work was to investigate IVIM as a potential method for acquiring reliable blood volume and/or perfusion information in the healthy brain. First, a direct comparison was performed between IVIM and ASL, a method capable of quantifying blood flow within grey matter which has been repeatedly validated against PET [113, 162]. Second, the impact of CSF on the IVIM signal was assessed by application of a CSF-nulled diffusion sequence. Finally, high-resolution IVIM data were acquired to isolate and compare signals arising from grey matter, white matter and CSF.

8.3 Methods

8.3.1 Experiment 1

10 subjects were scanned on a 3 T Siemens Verio scanner with a 32-channel head coil under the group's developmental ethics agreement. A standard 6:28-minute multi-PLD PCASL scan was run (6 delay times ranging 250–1500 ms) with 15 slices and voxel dimensions 3.4×3.4×6 mm. Head and body coil calibration images and field maps were also acquired. All PCASL data were preprocessed using FSL tools for motion and field map correction, and analysed using the BASIL toolbox [101].

For the IVIM, a standard diffusion sequence was run with b-values of 0, 10, 20, 40, 80, 110, 140, 170, 200, 300, 400, 500, 600, 700, 800 and 900 s/m^2, acquired in three orthogonal directions with a twice-refocussed spin echo [163] and an EPI readout. Simulations have suggested that a minimum of 10 b-values should be acquired in order provide sufficient points for reliable biexponential signal fitting [149], and the distribution used in the present study was chosen with reference to recent literature applying IVIM in the brain within a clinical setting [157]. Other parameters included TE 84 s, TR 4 s, BW 1086 Hz/pixel, echo spacing 0.99 ms, Fourier 6/8, GRAPPA off. Images were acquired at the same matrix size and resolution as PCASL data. In order to match the PCASL imaging time, 2 repetitions were acquired and averaged on the scanner, with an imaging time of 6:12 minutes. A $b = 0$ image with reversed phase-encoding was also acquired.

A 1 mm isotropic MPRAGE structural scan was acquired, which was segmented using FAST [112] and registered to both ASL and IVIM space using FLIRT [70]. Grey matter and white matter masks were created from voxels with partial volume estimates of 50% or above.

8.3.2 Experiment 2

One subject was re-scanned with an adapted protocol which was designed to identify signal arising from the CSF compartment. A non-selective BASSI inversion pulse was applied to null signal from spins with $T_1 = 3700$ ms, and only a single slice was acquired to ensure optimal CSF suppression. Imaging time and other parameters were identical to those set out in Experiment 1. For comparison, a second set of IVIM images was acquired with the BASSI voltage set to 0 for no CSF suppression. A PCASL scan was also performed, as described above.

Because of anticipated difficulties in registering a single slice to a structural image, a double inversion recovery sequence was run at the same resolution as the IVIM diffusion scans to obtain a suitable grey matter mask. Inversion times were set at 550 and 4150 ms prior to the excitation pulse. The resulting image was field map corrected using FUGUE [164] and manually thresholded to create a grey matter mask.

8.3.3 Experiment 3

In order to analyse IVIM signals definitively only originating from a single tissue type, 6 subjects were scanned on a 3 T Siemens Prisma with a 32-channel head coil and a high-resolution RESOLVE diffusion sequence. This allowed for a 1 mm isotropic resolution with minimal distortions, such that partial voluming could be avoided in a substantial subset of voxels. In order to maintain sufficient SNR the 6:14-minute protocol was repeated 6 times. Because of the potential for motion over this long scan time, the images were not averaged. The RESOLVE sequence was set up with TE 69 ms, TR 1.6 s, BW 766 Hz/pixel, echo spacing 0.4 ms, Fourier off, GRAPPA factor 2. b-values were identical to those in Experiments 1 and 2, but were acquired with Stejskal-Tanner (single-refocussed spin echo) encoding to minimise TE and maximise SNR.

An MPRAGE scan was performed at the same resolution and matrix size as the diffusion scan. This was segmented using FAST [112] to estimate the relative proportions of GM, WM and CSF in every voxel. Masks were created from voxels with 100% of the relevant tissue type.

8.3.4 IVIM Fitting

IVIM data from Experiments 1 and 3 were first corrected for motion and eddy current distortions [165]. The reversed phase-encoding $b = 0$ scan was used to correct for susceptibility-induced distortions in Experiment 1 using the TOPUP tool [166]. Because the data acquired in Experiment 2 was for a single slice only, it was not possible to apply eddy corrections or TOPUP. Instead, a field map was used in conjunction with FUGUE [164] to reduce distortions near the sinuses.

The biexponential model described in section 2.2.4.1 was fitted to each voxel in two steps [148, 159] using least squares fitting in MATLAB (MathWorks, Natick, MA, USA). This approach aims to mitigate the problem of overfitting, under the assumption that D^* is substantially larger than D and may be neglected for large b-values. First, a monoexponential model was fit to b-values greater than 200 to estimate D:

$$S = S_0 \, e^{-bD}. \tag{8.2}$$

Then the full biexponential model was fit to all b-values, with fixed D, to estimate f_v and D^*:

$$S = S_0\big\{(1 - f_v)\, e^{-bD} + f_v\, e^{-bD^*}\big\}. \tag{8.3}$$

S_0 was unconstrained in both cases.

8.3.5 Statistical Comparisons

For Experiment 1, GM masks were applied to ASL and IVIM images. Voxels with $f_v > 0.3$ were excluded from masks as this is unphysiological, presumably as a result of CSF contamination [157]. Correlations between ASL perfusion and IVIM f_v and perfusion were hypothesised to be linear and were assessed by computing the Pearson product-moment correlation coefficients (r) and the corresponding p-values, where $p < 0.05$ was deemed to be significant.

In Experiment 2, IVIM analysis was performed both on a voxelwise and a region of interest (ROI) basis. For ROI fitting, the signal was averaged across all b-directions and all grey matter voxels in order to boost SNR.

Voxelwise fitting was performed on data from Experiment 3, and the IVIM-derived parameter maps were visually compared to structural images. Correlations between blood volume fraction f_v and GM, WM and CSF fraction of partially volumed voxels were investigated by plotting 2D histograms. Box plots were created to compare the distributions of f_v and perfusion in pure GM, WM and CSF.

8.4 Results

8.4.1 Experiment 1

Average grey matter results are presented in table 8.1. White matter perfusion cannot be reliably measured using ASL because of the long arterial arrival time

Table 8.1: Average grey matter values for each subject in Experiment 1. $f_v\,D^*$ is the IVIM perfusion parameter. ASL units are ml/100 g/min; D, D^* and $f_v\,D^*$ are all measured in m^2/s.

Subject	ASL perfusion	f_v	D ($\times10^{-3}$)	D^* ($\times10^{-3}$)	$f_v\,D^*$ ($\times10^{-3}$)
1	43.6	0.11	0.93	10.40	0.96
2	40.8	0.11	0.92	12.71	1.56
3	59.0	0.11	0.92	9.00	0.93
4	54.7	0.10	0.84	12.09	1.22
5	55.2	0.12	0.92	15.44	2.54
6	46.0	0.13	0.94	10.17	1.27
7	44.7	0.10	0.95	11.52	1.25
8	41.3	0.11	0.88	14.79	1.94
9	51.4	0.10	0.89	9.46	1.02
10	65.2	0.12	0.92	12.09	1.74
mean ± std	50.2 ± 8.2	0.11 ± 0.01	0.91 ± 0.03	11.77 ± 2.14	1.44 ± 0.51

[130]; however no such limitation applies to IVIM. $f_v\,D^*$ in white matter was found to be $0.81 \pm 0.20 \times10^{-3}$ m^2/s, leading to a GM/WM perfusion ratio of 1.87 ± 0.88 (ranging from 1.12 to 3.97).

Figure 8.1 shows ASL and IVIM maps for a subset of slices acquired from a representative subject, along with the GM mask used for IVIM parameters. The GM masks for ASL are almost identical to those for IVIM, with small differences arising from slightly different distortions between the two readouts and any motion between the scans. Maps for ASL and IVIM perfusion look qualitatively similar, with the same features visible on both sets of images. Quantitatively however, no significant correlation was observed between ASL and IVIM perfusion (figure 8.2(a), $r = 0.090$, $p = 0.805$) or ASL and IVIM f_v (figure 8.2(b), $r = 0.107$, $p = 0.768$).

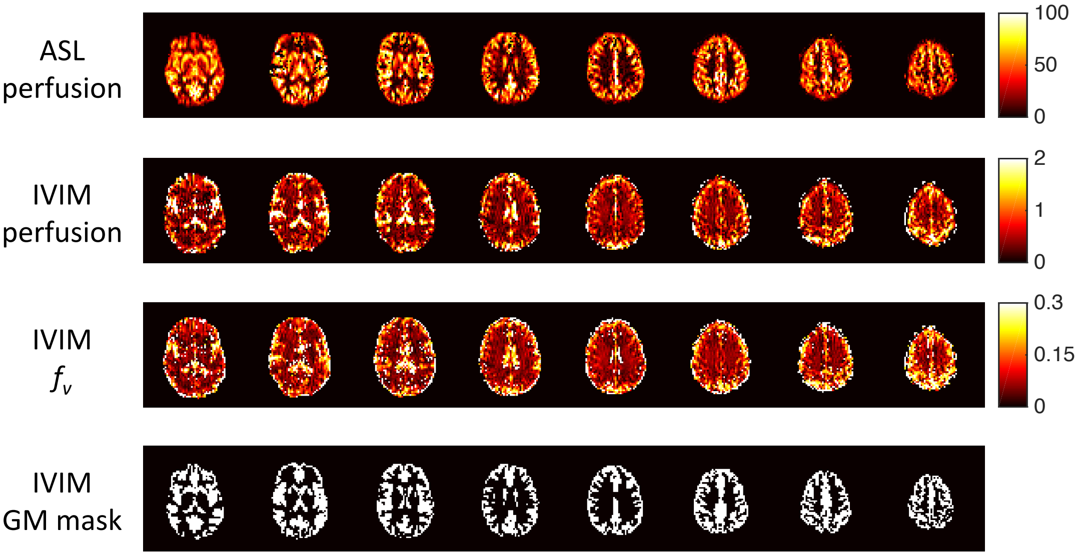

Figure 8.1: A subset of slices acquired from a single representative subject. Units are ml/100 g/min for ASL perfusion and 10^{-3} m^2/s for IVIM perfusion. f_v is the capillary blood volume fraction in each voxel.

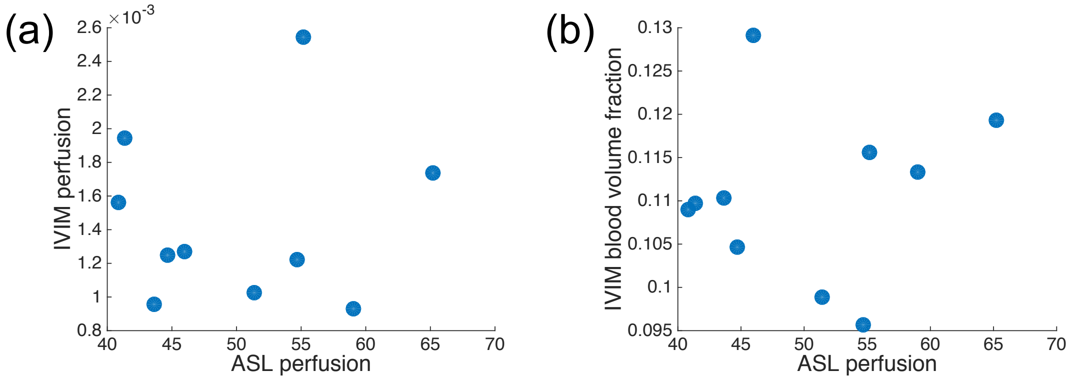

Figure 8.2: Plots comparing ASL perfusion with IVIM perfusion across the 10 subjects (a) and IVIM blood volume fraction (b) in grey matter. No significant correlation was observed in either case.

8.4.2 Experiment 2

Figure 8.3 shows the results of the voxelwise fitting of both standard and CSF-suppressed IVIM sequences, along with an ASL perfusion map of the same slice and the GM mask created from a double inversion recovery sequence. CSF signal was successfully suppressed, as may be seen by comparing the $b = 0$ images in the top row. Both blood volume fraction and perfusion maps from IVIM fits bear some resemblance to the ASL map for the case of standard IVIM; however this similarity disappears in the CSF-suppressed case.

The ROI-averaged fits for standard and CSF-suppressed IVIM signals are shown in figure 8.4. For the standard case, the signal clearly exhibits biexponential behaviour. With CSF-suppression the fits perform almost equally well; statistically the biexponential model produces a marginally higher R^2, which appears to be driven by a closer fit for $b < 40$ s/m^2, but visually there is little difference between the two fits.

8.4.3 Experiment 3

Figure 8.5 shows maps of IVIM parameters from a single representative subject, alongside a structural image and the CSF partial volume estimate map derived from it. Areas with the highest IVIM blood volume fractions f_v clearly correspond to those with the highest CSF fraction, and no obvious contrast between grey and white matter is seen in IVIM maps. All fits were done on a voxelwise basis with no smoothing or averaging applied. For reference, fits for 3 randomly selected voxels from the same subject, which contain 100% GM, WM and CSF respectively, are shown in figure 8.6.

Structural images and blood volume fraction (f_v) maps for all subjects are displayed in figure 8.7. Also shown are 2D histograms exploring the relationship

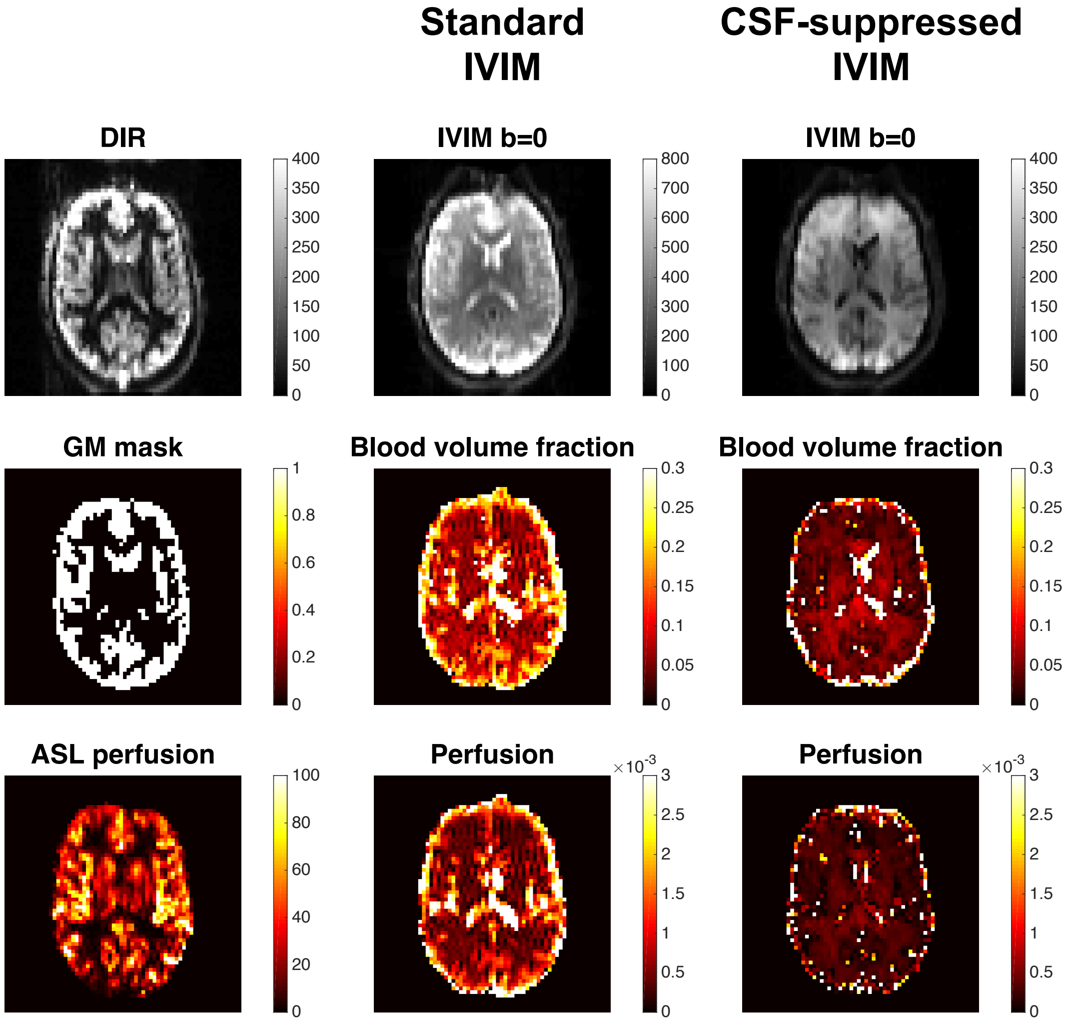

Figure 8.3: Single-slice IVIM results from Experiment 2, acquired with and without CSF-suppression. $b = 0$ images demonstrate that CSF was successfully suppressed by the sequence. Also shown is the double inversion recovery (DIR) image, which was thresholded to produce the grey matter (GM) mask. Blood volume fraction is f_v, IVIM perfusion is $f_v\,D^*$ in units of m^2/s. ASL perfusion has units of ml/100 g/min.

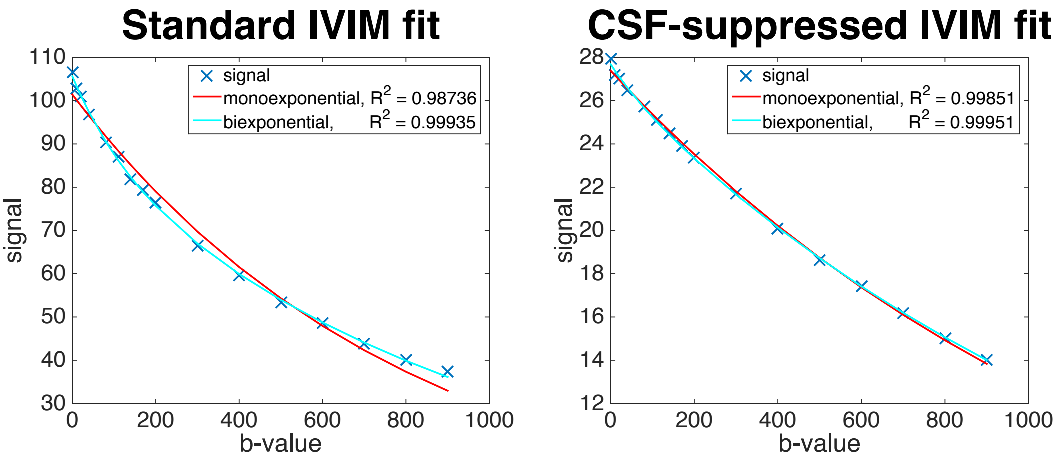

Figure 8.4: Plots showing the mono- and biexponential fits to IVIM signals from standard and CSF-suppressed data, after averaging over all grey matter voxels. The biexponential model is clearly a better fit for the standard IVIM data, whereas the monoexponential model appears sufficient for CSF-suppressed data. Note the different signal scales for the two cases.

between GM, WM and CSF partial volume estimates (pve) and IVIM blood volume fraction. No correlation is seen for GM or WM, but a positive trend is observed for CSF. Note that extreme values (100% pve voxels, $f_v = 1$) have been excluded from these histograms. Figure 8.8 compares the distribution of f_v and $f_v\,D^*$ in the form of box plots for a single subject, derived only from voxels with no partial voluming. These show considerably higher f_v and $f_v\,D^*$ in CSF compared to GM or WM. Extreme outliers were observed for all tissue types and were excluded from the plots. $f_v\,D^*$ was significantly different in CSF compared to WM ($p < 0.001$ in all subjects) and GM ($p < 0.05$ in all subjects, and $p < 0.001$ in 4 of the 6). $f_v\,D^*$ in GM and WM differed significantly in only 3 subjects ($p < 0.05$), but in all 6 cases the median values were slightly higher in WM than in GM.

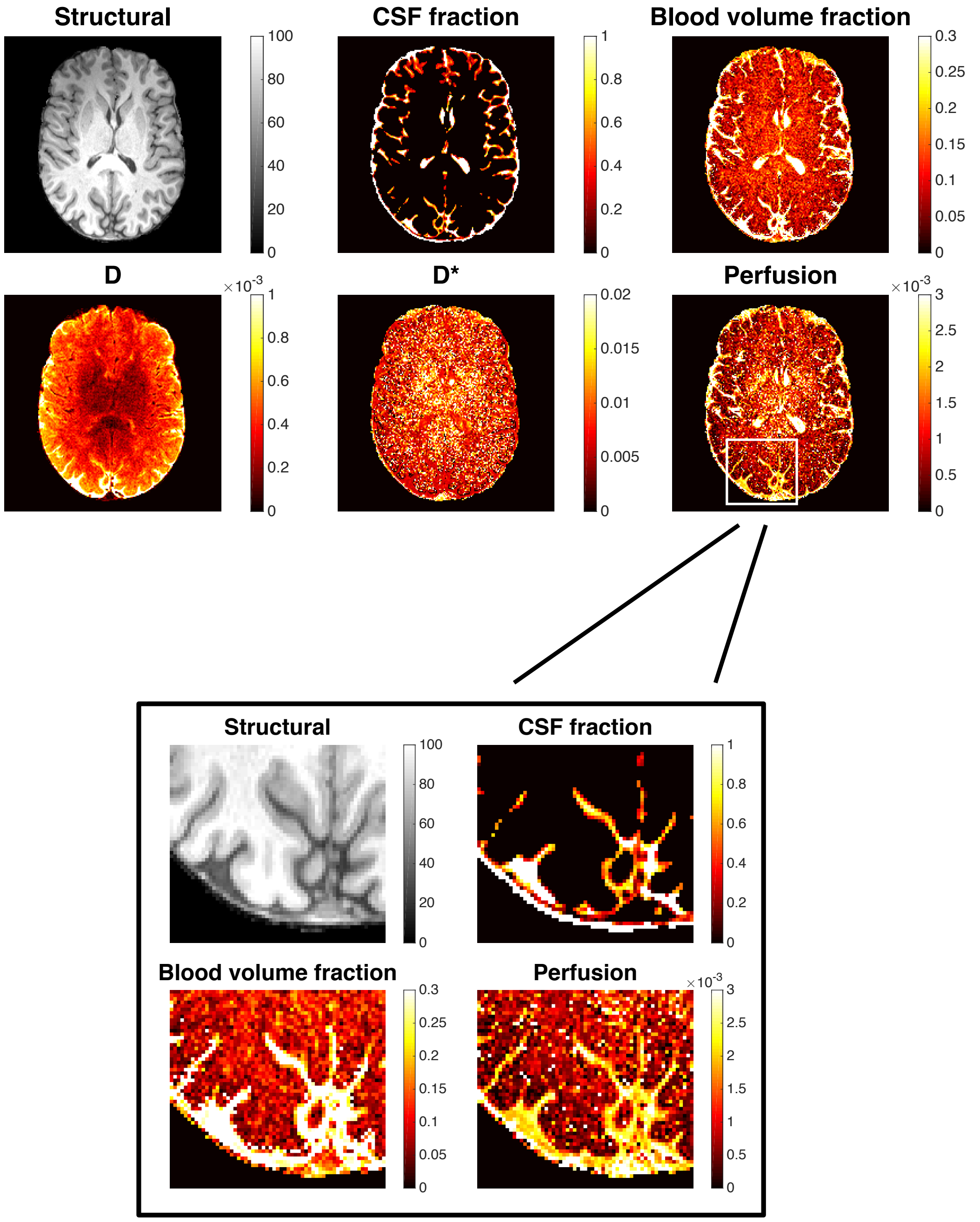

Figure 8.5: High-resolution IVIM data acquired with a RESOLVE diffusion sequence. Both blood volume fraction (f_v) and perfusion ($f_v\,D^*$) are elevated in voxels containing high fractions of CSF, and no noticeable contrast is observed between grey and white matter.

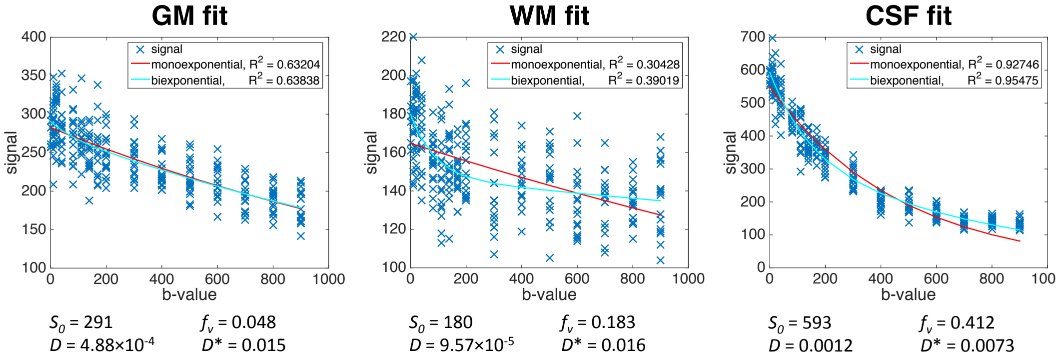

Figure 8.6: Plots of IVIM fits to single voxel data, taken from randomly selected pure tissue voxels in the slice shown in figure 8.5. Each b-value has 18 data points corresponding to 3 diffusion directions and 6 repeats. R^2 values are highest in CSF voxels, presumably because of higher signal levels (see standard IVIM $b = 0$ image in figure 8.3 for an example of raw diffusion data). The monoexponential fits shown are for comparison only and were derived from all 16 b-values; they do not represent the fits performed to calculate D.

8.5 Discussion

IVIM claims to be a quantitative model [33], yet conclusive validation of the method within the brain is still lacking, with past studies reporting both positive [167] and negative [168] correlations between f_v and DSC or ASL MRI methods, respectively. Although qualitative similarities were observed between IVIM parameters and ASL perfusion maps (figure 8.1), this study found no significant correlation between average GM values across a group of 10 subjects (figure 8.2).

At a low spatial resolution, contrast between grey and white matter is markedly reduced but still visible in IVIM parameters compared to ASL (figures 8.1 and 8.3). This is unsurprising given the limitations on arterial arrival time that ASL is subject to, meaning that WM perfusion will always appear low on ASL images. The mean ratio of GM/WM perfusion of 1.87 for IVIM compares well with the ratio of 2.07 observed in young healthy volunteers using PET [169], although the individual range in this study (1.12–3.97) was fairly large.

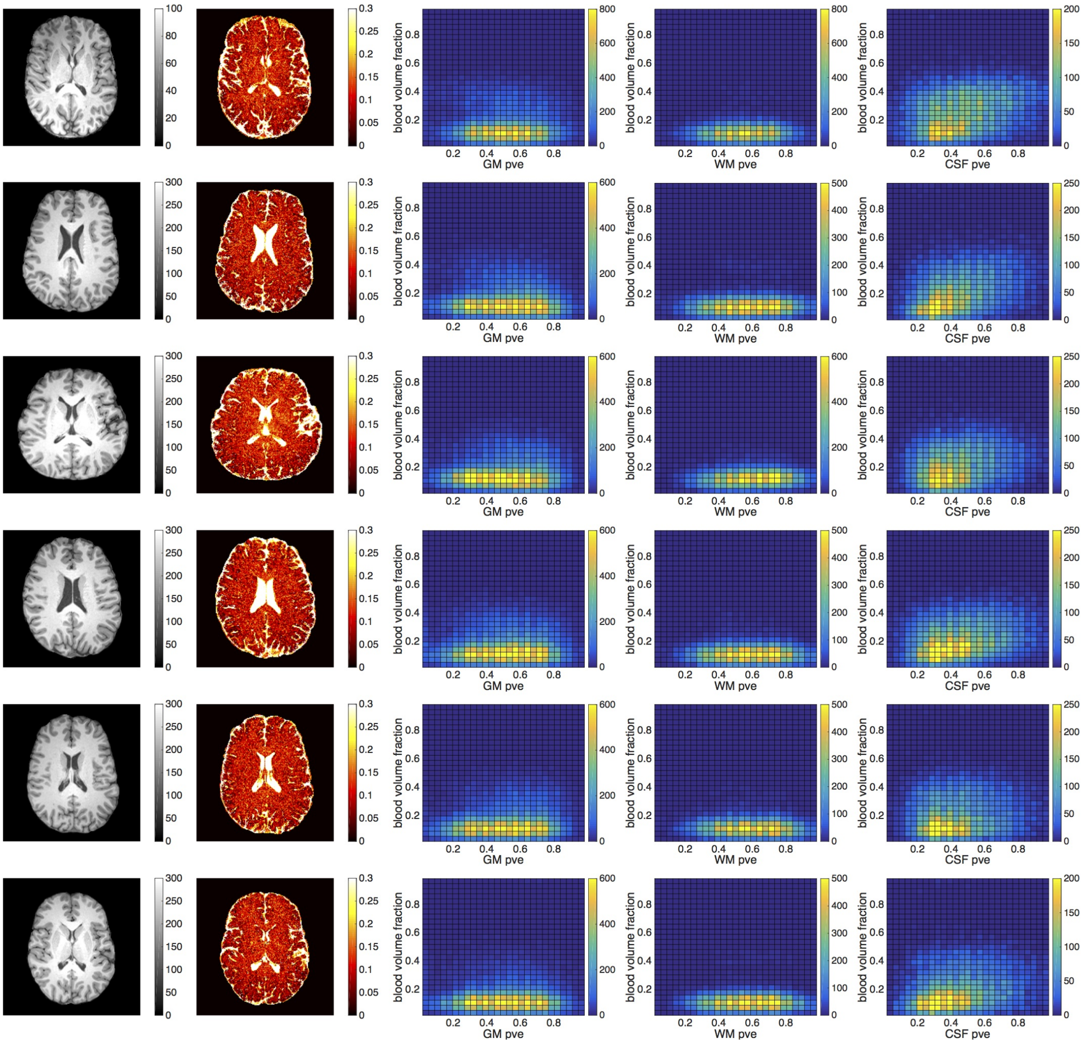

Figure 8.7: Results of Experiment 3 in all 6 subjects. Columns display one slice of the structural image (arbitrary units) and the blood volume fraction f_v, followed by histograms correlating voxelwise GM, WM and CSF partial volume estimates (pve) against blood volume fraction. Voxels containing only a single tissue type are not included in these plots.

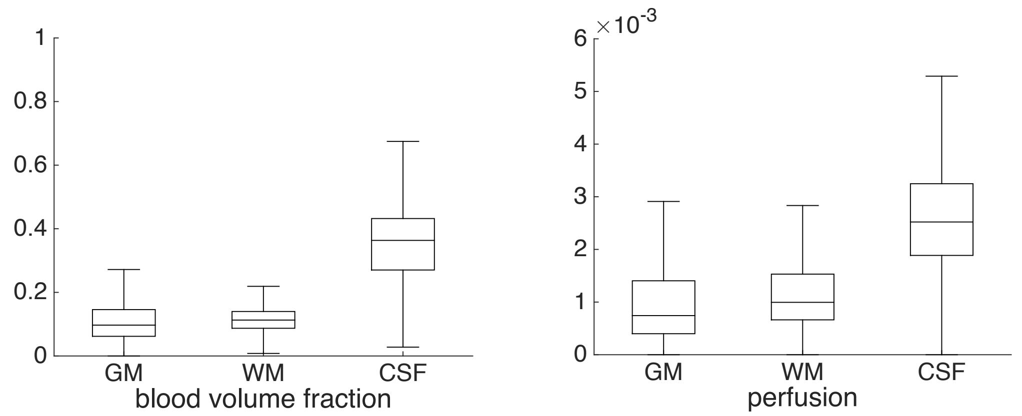

Figure 8.8: Box plots of the blood volume fraction (f_v) and perfusion ($f_v\, D^*$) values observed in pure GM, WM and CSF voxels for a single representative subject.

Using literature values for the mean capillary length $<l>$ and the total length of the capillary network L it should be possible to convert $f_v\, D^*$ to traditional units of CBF using equation 8.1. For the human brain, values of $\lambda = 0.78$ [33], $<l> = 53\ \mu\text{m}$ [134] and $L = 1$ mm [170] would result in a CBF of 21.2 ml/100 g/min, somewhat lower than the ASL-derived 50.2 ml/100 g/min in the same cohort. As the definition of what exactly constitutes a capillary is not always clear, it is plausible that the scarce literature on human brain morphometry was based on a slightly different definition than that used in the derivation of the IVIM model.

It is possible that the lack of correlation shown in figure 8.2 could be caused by different vessel properties (e.g. average length of capillary segments) between individuals. Although the ability to compare absolute perfusion between subjects is very valuable, particularly in clinical cases of potential global hypo- or hyperperfusion, the scientific community is typically more concerned with generating spatial or functional contrast. Thus the question of greatest interest is whether the contrast observed in f_v and $f_v\, D^*$ for a single subject is a true reflection on underlying blood volume or perfusion. Given past concerns over the contaminating effects of CSF signal [153], it is difficult to conclude whether the spatial similarity between ASL and IVIM images in Experiment 1 supports this hypothesis, especially as the majority of GM voxels will also include a sizeable fraction of CSF at this relatively low resolution.

Experiment 2 was designed to try to answer this question by acquiring diffusion data with and without CSF-suppression. At first glance, the results imply that the GM/WM contrast observed in IVIM-derived images is a direct result of CSF signal contamination. When CSF is successfully nulled, f_v and $f_v\,D^*$ values are notably decreased in GM (figure 8.3), and a simple monoexponential model is adequate for fitting the data (figure 8.4). This is in agreement with past literature [153].

However, there are several limitations to the method used in Experiment 2. Only a single inversion preparation pulse was implemented; this was timed to maximally suppress signal from the CSF compartment, but inevitably will also have reduced signal from other tissue types. Previous simulation work suggests that when CSF is nulled following a single inversion, signal from arterial blood is reduced to 30% and GM signal to 40% of their respective equilibrium M_0 values [171]. Thus the CSF-suppressed data not only has lower SNR compared to the standard case, but also differing relative fractions of blood, GM and WM signal contributions. This makes it difficult to draw firm conclusions from the results.

In a different approach, Experiment 3 acquired IVIM data at a much higher resolution in order to minimise the effects of partial voluming within voxels. Application of a RESOLVE sequence on a high gradient performance Prisma scanner allowed for the acquisition of ten 1 mm isotropic slices in a feasible scan time. The resulting images (see figure 8.5) show that f_v and $f_v\,D^*$ are elevated in voxels containing CSF (as expected), but that no contrast is visible between grey and white matter voxels. In addition, there appears to be some consistent correlation between f_v and CSF fraction, but not with GM or WM fraction, as shown in figure 8.7. Together, this strongly suggests that f_v is primarily sensitive to voxelwise CSF content and not true capillary blood volume.

The box plots in figure 8.8 confirm that f_v and $f_v\,D^*$ are highest in the CSF compartment, and also show that the median $f_v\,D^*$ value is marginally higher in WM than GM. The same observations were made for all subjects. Regardless of units, this result is both unexpected and unphysiological for a perfusion contrast [169]. It also suggests that the plausible GM/WM 'perfusion' ratio observed in Experiment 1 may in fact be an averaged (GM+CSF)/WM ratio.

One possible explanation for the unexpectedly high WM results is overfitting. Throughout this chapter, data have been analysed using the biexponential fitting procedure described in section 8.3.4 for all voxels, even when the simpler monoexponential fit appears to do an adequate job. This was intentional and in accordance with the recent literature [151, 159]. However, by fitting a biexponential function to a noisy monoexponential decay curve, large values for f_v can be estimated despite a true underlying $f_v = 0$. The anisotropy in WM leads to greater variance in signal across diffusion directions compared to GM (see figure 8.6), which can masquerade as a lower SNR and may hence lead to poorer fitting.

As previously mentioned, the idea that the biexponential form of the diffusion signal arises from CSF contamination is not new [153]. However the fact that this biexponential behaviour was observed even in 100% pure CSF voxels, with resulting f_v of around 0.4, suggests that IVIM may in fact be measuring CSF motion (either turbulent or related to the cardiac cycle). In larger voxels, the mixing of different tissue types may be an additional contributing factor.

It is difficult to balance the requirements for high spatial resolution (to reduce partial voluming effects), high SNR (to ensure reasonable fitting) and acceptable temporal resolution in order to carry out a functional experiment with IVIM. However, one group has recently reported observing changes in $f_v\,D^*$ with hypercapnia [159], visual stimulation [160] and at different phases during the cardiac cycle [172], and interpreted these as increases in classical perfusion. Although absolute signal magnitude is very difficult to interpret, relative changes in IVIM parameters may reflect underlying physiological modulation, somewhat analogous to the BOLD signal. However, the advantages of this method over the BOLD signal are not clear, and the impact of any concurrent changes in CSF volume or pulsatility would need to be considered [173].

There have been a number of studies demonstrating that IVIM can be used to generate clinically useful contrasts in both the abdomen [137, 142] and the brain [155, 157]. For these situations, it may not be important whether the contrast is generated by excess fluid (for example surrounding a tumour) or by true perfusion, and in all probability IVIM will – and should – continue to be a useful tool for creating these qualitative images. However, based on the results presented in this chapter, caution should be exercised in the interpretation of such images, especially if attempting to look beyond basic contrast to draw physiological conclusions from the data.

8.6 Conclusions

Within the brain, IVIM parameters f_v and $f_v\,D^*$ do not appear to be related strongly to blood volume or perfusion, but rather to CSF content. Although these contrasts may be clinically very valuable, they are not quantitative and should not be interpreted as corresponding to any specific physiological parameters.

9

Summary and Future Work

9.1 Thesis Summary

This thesis described an investigation into the signal characteristics of the Davis model, and attempted to validate the calibrated MRI technique against an independent modality, as well as searching for ways of improving aspects of the current calibrated MRI methodology. In Chapter 4 it was found that the Davis model produces consistent results at 3 and 7 T. M values increased in both magnitude and inter-subject variability as field strength was increased, in agreement with simulations, but relative CMRO_2 changes to motor tasks remained consistent. However, metabolism increases were overestimated at 1.5 T as a result of poor SNR in ASL data.

Chapter 5 tested the hypothesis that M is directly proportional to echo time, as is predicted by the theory and frequently assumed when comparing across different studies. It was confirmed that M does vary linearly with echo time, but that there is a non-zero offset, which is substantially decreased when intravascular flow crushers are applied. This suggests that the theory is valid for extravascular spins (for which it was intended), but that intravascular signal contribution is not negligible as is commonly assumed.

In Chapter 6 a direct comparison was performed between calibrated MRI and triple oxygen PET. Although resting blood flow showed significant correlation between the two modalities, neither OEF nor $CMRO_2$ were correlated. MRI values for OEF were considerably lower than expected in this study. Chapter 7 built on these results by investigating 4 possible causes for the poor results: the lack of background suppression, the use of a nasal cannula for gas delivery, assuming the shapes of end-tidal respiratory traces for analysis, and not applying any physiological noise modelling. The greatest improvements were demonstrated by delivering respiratory stimuli via a gas mask and by applying background suppression. Using personalised end-tidal traces showed some improvement in fitting for a subset of subjects. However, the use of physiological noise modelling showed no improvements in this study, suggesting that random scanner noise had a greater effect on the data.

Finally, Chapter 8 considered the use of IVIM as an alternative method for measuring blood volume or perfusion in the brain. Although a qualitative similarity was observed between IVIM and ASL maps with large voxel sizes, higher-resolution data confirmed that the primary source of IVIM contrast arises from CSF, and it is not possible to obtain reliable, quantitative information from the IVIM method within the brain.

9.2 Future Work

Much remains to be done in the area of calibrated MRI. The ability to non-invasively image resting OEF in the brain is particularly inviting, but has yet to be verified against an independent modality or to make the transition into clinical research, let alone clinical practice. Below are two ideas for future work that have arisen during the course of this thesis.

Steady State Hypercapnia Challenge

It would be interesting to consider applying a multi-PLD PCASL sequence during mild hypercapnia as well as during baseline. As well as improving SNR through additional signal averaging, this would account for any changes in blood arrival times which may be mistaken for increased perfusion in the single PLD case, and may be particularly useful in the measurement of cerebrovascular reactivity with ASL. It could be combined with a dual echo or double excitation readout to allow for simultaneous BOLD information on BOLD response. However, longer periods of even mild hypercapnia are less well tolerated by subjects, which would have to be taken into account.

Extension to a Patient Population

The translation of the calibrated MRI method from healthy subjects to a clinical setting remains a challenge. Although velocity-selective ASL has an SNR penalty compared to PCASL, it may prove valuable in quantifying perfusion in patients with a very slow or collateral blood flow. It may be possible to adapt the Davis model to a wider range of physiology, for example by removing the assumptions that arterial blood is 100% oxygenated. The Cardiff model may be particularly useful in this setting, as the Grubb flow-volume coupling constant – which may be expected to vary significantly within pathological tissue – no longer needs to be assumed. Measuring and using end-tidal respiratory information for such subjects may significantly improve signal fitting, especially if patients are under sedation or have impaired lung function.

Bibliography

[1] D. P. Bulte, M. Kelly, M. Germuska, J. Xie, M. A. Chappell, T. W. Okell, M. G. Bright, and P. Jezzard. Quantitative measurement of cerebral physiology using respiratory-calibrated MRI. *NeuroImage*, 60(1):582–591, 2012.

[2] C. J. Gauthier and R. D. Hoge. Magnetic resonance imaging of resting OEF and CMRO2 using a generalized calibration model for hypercapnia and hyperoxia. *NeuroImage*, 60(2):1212–1225, 2012.

[3] R. G. Wise, A. D. Harris, A. J. Stone, and K. Murphy. Measurement of OEF and absolute CMRO2: MRI-based methods using interleaved and combined hypercapnia and hyperoxia. *NeuroImage*, 83:135–147, 2013.

[4] R. B. Buxton. *Introduction to functional magnetic resonance imaging: principles and techniques*. Cambridge University Press, 2009.

[5] E. M. Haacke, R. W. Brown, M. R. Thompson, and R. Venkatesan. *Magnetic resonance imaging: physical principles and sequence design*. John Wiley & Sons, 1999.

[6] S. A. Huettel, A. W. Song, and G. McCarthy. *Functional magnetic resonance imaging*. Sinauer Associates Sunderland, 2004.

[7] M. A. Bernstein, K. F. King, and X. J. Zhou. *Handbook of MRI pulse sequences*. Elsevier, 2004.

[8] Y. Gossuin, H. Aline, P. Gillis, and L. V. Quoc. Physics of magnetic resonance imaging: from spin to pixel. *Journal of Physics D: Applied Physics*, 43(21):213001, 2010.

[9] S. Ogawa, T.-M. Lee, A. R. Kay, and D. W. Tank. Brain magnetic resonance imaging with contrast dependent on blood oxygenation. *Proceedings of the National Academy of Sciences*, 87(24):9868–9872, 1990.

[10] K. K. Kwong, J. W. Belliveau, D. A. Chesler, I. E. Goldberg, R. M. Weisskoff, B. P. Poncelet, D. N. Kennedy, B. E. Hoppel, M. S. Cohen, and R. Turner. Dynamic magnetic resonance imaging of human brain activity during primary sensory stimulation. *Proceedings of the National Academy of Sciences*, 89(12):5675–5679, 1992.

[11] S. Ogawa, D. W. Tank, R. Menon, J. M. Ellermann, S. G. Kim, H. Merkle, and K. Ugurbil. Intrinsic signal changes accompanying sensory stimulation: functional brain mapping with magnetic resonance imaging. *Proceedings of the National Academy of Sciences*, 89(13):5951–5955, 1992.

[12] R. B. Buxton. Dynamic models of BOLD contrast. *NeuroImage*, 62(2):953–961, 2012.

[13] E. T. Petersen, I. Zimine, Y.-C. L. Ho, and X. Golay. Non-invasive measurement of perfusion: a critical review of arterial spin labelling techniques. *British Journal of Radiology*, 79:688–701, 2006.

[14] D. C. Alsop, J. A. Detre, X. Golay, M. Günther, J. Hendrikse, L. Hernandez-Garcia, H. Lu, B. J. MacIntosh, L. M. Parkes, M. Smits, *et al.* Recommended implementation of arterial spin-labeled perfusion MRI for clinical applications: A consensus of the ISMRM perfusion study group and the European consortium for ASL in dementia. *Magnetic Resonance in Medicine*, 73(1):102–116, 2015.

[15] R. R. Edelman, B. Siewert, D. G. Darby, B. S. Venketasen Thangaraj, A. C. Nobre, M. M. Mesulam, and S. Warach. Qualitative mapping of cerebral blood flow and functional localization with echo-planar MR imaging and signal targeting with alternating radio frequency. *Radiology*, 192(2):513–520, 1994.

[16] E. C. Wong, R. B. Buxton, and L. R. Frank. Implementation of quantitative perfusion imaging techniques for functional brain mapping using pulsed arterial spin labeling. *NMR in Biomedicine*, 10(45):237–249, 1997.

[17] S.-G. Kim. Quantification of relative cerebral blood flow change by flow-sensitive alternating inversion recovery (FAIR) technique: Application to functional mapping. *Magnetic Resonance in Medicine*, 34(3):293–301, 1995.

[18] A. G. Gardener, P. A. Gowland, and S. T. Francis. Implementation of quantitative perfusion imaging using pulsed arterial spin labeling at ultra-high field. *Magnetic Resonance in Medicine*, 61(4):874–882, 2009.

[19] E. C. Wong, R. B. Buxton, and L. R. Frank. Quantitative imaging of perfusion using a single subtraction (QUIPSS and QUIPSS II). *Magnetic Resonance in Medicine*, 39(5):702–708, 1998.

[20] R. B. Buxton, L. R. Frank, E. C. Wong, B. Siewert, S. Warach, and R. R. Edelman. A general kinetic model for quantitative perfusion imaging with arterial spin labeling. *Magnetic Resonance in Medicine*, 40(3):383–396, 1998.

[21] W. Dai, D. Garcia, C. de Bazelaire, and D. C. Alsop. Continuous flow-driven inversion for arterial spin labeling using pulsed radio frequency and gradient fields. *Magnetic Resonance in Medicine*, 60(6):1488–1497, 2008.

[22] E. C. Wong. New developments in arterial spin labeling pulse sequences. *NMR in Biomedicine*, 26(8):887–891, 2013.

[23] E. C. Wong, M. Cronin, W.-C. Wu, B. Inglis, L. R. Frank, and T. T. Liu. Velocity-selective arterial spin labeling. *Magnetic Resonance in Medicine*, 55(6):1334–1341, 2006.

[24] N. Maleki, W. Dai, and D. C. Alsop. Optimization of background suppression for arterial spin labeling perfusion imaging. *Magnetic Resonance Materials in Physics, Biology and Medicine*, 25(2):127–133, 2012.

[25] E. Ghariq, M. A. Chappell, S. Schmid, W. M. Teeuwisse, and M. J. P. van Osch. Effects of background suppression on the sensitivity of dual-echo arterial spin labeling MRI for BOLD and CBF signal changes. *NeuroImage*, 103:316–322, 2014.

[26] J. J. Chen and G. B. Pike. Origins of the BOLD post-stimulus undershoot. *NeuroImage*, 46(3):559–568, 2009.

[27] K. Uludağ, D. J. Dubowitz, E. J. Yoder, K. Restom, T. T. Liu, and R. B. Buxton. Coupling of cerebral blood flow and oxygen consumption during physiological activation and deactivation measured with fMRI. *NeuroImage*, 23(1):148–155, 2004.

[28] C. I. Mark, J. A. Fisher, and G. B. Pike. Improved fMRI calibration: precisely controlled hyperoxic versus hypercapnic stimuli. *NeuroImage*, 54(2):1102–1111, 2011.

[29] V. J. Schmithorst, L. Hernandez-Garcia, J. Vannest, A. Rajagopal, G. Lee, and S. K. Holland. Optimized simultaneous ASL and BOLD functional imaging of the whole brain. *Journal of Magnetic Resonance Imaging*, 39(5):1104–1117, 2014.

[30] A. Einstein. Über die von der molekularkinetischen Theorie der Wärme geforderte Bewegung von in ruhenden Flüssigkeiten suspendierten Teilchen. *Annalen der Physik*, 322(8):549–560, 1905.

[31] D. Le Bihan, E. Breton, D. Lallemand, P. Grenier, E. Cabanis, and M. Laval-Jeantet. MR imaging of intravoxel incoherent motions: Application to diffusion and perfusion in neurologic disorders. *Radiology*, 161(2):401–407, 1986.

[32] H. R. Weiss, E. Buchweitz, T. J. Murtha, and M. Auletta. Quantitative regional determination of morphometric indices of the total and perfused capillary network in the rat brain. *Circulation Research*, 51(4):494–503, 1982.

[33] D. Le Bihan and R. Turner. The capillary network: A link between IVIM and classical perfusion. *Magnetic Resonance in Medicine*, 27(1):171–178, 1992.

[34] Wikipedia. Chemical synapse – Wikipedia, the free encyclopedia. `http://upload.wikimedia.org/wikipedia/commons/3/30/Chemical_synapse_schema_cropped.jpg`. [Online; accessed 4 May 2015].

[35] D. Attwell and S. B. Laughlin. An energy budget for signaling in the grey matter of the brain. *Journal of Cerebral Blood Flow & Metabolism*, 21(10):1133–1145, 2001.

[36] J. Hatazawa, H. Fujita, I. Kanno, T. Satoh, H. Iida, S. Miura, M. Murakami, T. Okudera, A. Inugami, T. Ogawa, *et al.* Regional cerebral blood flow, blood volume, oxygen extraction fraction, and oxygen utilization rate in normal volunteers measured by the autoradiographic technique and the single breath inhalation method. *Annals of Nuclear Medicine*, 9(1):15–21, 1995.

[37] G. J. Kelloff, J. M. Hoffman, B. Johnson, H. I. Scher, B. A. Siegel, E. Y. Cheng, B. D. Cheson, J. O'Shaughnessy, K. Z. Guyton, D. A. Mankoff, *et al.* Progress and promise of FDG-PET imaging for cancer patient management and oncologic drug development. *Clinical Cancer Research*, 11(8):2785–2808, 2005.

[38] R. B. Firestone. Table of radioactive isotopes – Isotopes project, Ernest Orlando Lawrence Berkeley National Laboratory. `http://ie.lbl.gov/toi/nucSearch.asp`. [Online; accessed 5 May 2015].

[39] J. P. Coles, T. D. Fryer, P. Smielewski, D. A. Chatfield, L. A. Steiner, A. J. Johnston, S. P. M. J. Downey, G. B. Williams, F. Aigbirhio, P. J. Hutchinson, *et al.* Incidence and mechanisms of cerebral ischemia in early clinical head injury. *Journal of Cerebral Blood Flow & Metabolism*, 24(2):202–211, 2004.

[40] M. A. Mintun, M. E. Raichle, W. R. Martin, and P. Herscovitch. Brain oxygen utilization measured with O-15 radiotracers and positron emission tomography. *Journal of Nuclear Medicine*, 25(2):177–187, 1984.

[41] J. U. Blicher, C. J. Stagg, J. O'Shea, L. Østergaard, B. J. MacIntosh, H. Johansen-Berg, P. Jezzard, and M. J. Donahue. Visualization of altered neurovascular coupling in chronic stroke patients using multimodal functional MRI. *Journal of Cerebral Blood Flow & Metabolism*, 32(11):2044–2054, 2012.

[42] T. L. Davis, K. K. Kwong, R. M. Weisskoff, and B. R. Rosen. Calibrated functional MRI: mapping the dynamics of oxidative metabolism. *Proceedings of the National Academy of Sciences*, 95(4):1834–1839, 1998.

[43] P. A. Chiarelli, D. P. Bulte, R. Wise, D. Gallichan, and P. Jezzard. A calibration method for quantitative BOLD fMRI based on hyperoxia. *NeuroImage*, 37(3):808–820, 2007.

[44] J. J. Chen and G. B. Pike. Global cerebral oxidative metabolism during hypercapnia and hypocapnia in humans: implications for BOLD fMRI. *Journal of Cerebral Blood Flow & Metabolism*, 30(6):1094–1099, 2010.

[45] K. M. Sicard and T. Q. Duong. Effects of hypoxia, hyperoxia, and hypercapnia on baseline and stimulus-evoked BOLD, CBF, and CMRO2 in spontaneously breathing animals. *NeuroImage*, 25(3):850–858, 2005.

[46] J. L. Boxerman, L. M. Hamberg, B. R. Rosen, and R. M. Weisskoff. MR contrast due to intravascular magnetic susceptibility perturbations. *Magnetic Resonance in Medicine*, 34(4):555–566, 1995.

[47] R. D. Hoge, J. Atkinson, B. Gill, G. R. Crelier, S. Marrett, and G. B. Pike. Investigation of BOLD signal dependence on cerebral blood flow and oxygen

consumption: the deoxyhemoglobin dilution model. *Magnetic Resonance in Medicine*, 42(5):849–863, 1999.

[48] R. L. Grubb, M. E. Raichle, J. O. Eichling, and M. M. Ter-Pogossian. The effects of changes in PaCO2 cerebral blood volume, blood flow, and vascular mean transit time. *Stroke*, 5(5):630–639, 1974.

[49] J. J. Chen and G. B. Pike. BOLD-specific cerebral blood volume and blood flow changes during neuronal activation in humans. *NMR in Biomedicine*, 22(10):1054–1062, 2009.

[50] J. J. Chen and G. B. Pike. MRI measurement of the BOLD-specific flow–volume relationship during hypercapnia and hypocapnia in humans. *NeuroImage*, 53(2):383–391, 2010.

[51] D. McAuley. Aa gradient – GlobalRPh, the clinician's ultimate reference. `http://www.globalrph.com/aagradient.htm`. [Online; accessed 18 May 2015].

[52] C. J. Gauthier and R. D. Hoge. A generalized procedure for calibrated MRI incorporating hyperoxia and hypercapnia. *Human Brain Mapping*, 34(5):1053–1069, 2013.

[53] J. M. Murkin, S. J. Adams, R. J. Novick, M. Quantz, D. Bainbridge, I. Iglesias, A. Cleland, B. Schaefer, B. Irwin, and S. Fox. Monitoring brain oxygen saturation during coronary bypass surgery: a randomized, prospective study. *Anesthesia & Analgesia*, 104(1):51–58, 2007.

[54] M.-C. Taillefer and A. Y. Denault. Cerebral near-infrared spectroscopy in adult heart surgery: systematic review of its clinical efficacy. *Canadian Journal of Anesthesia*, 52(1):79–87, 2005.

[55] S. P. Gopinath, C. S. Robertson, C. F. Contant, R. K. Narayan, R. G. Grossman, and B. Chance. Early detection of delayed traumatic intracranial hematomas using near-infrared spectroscopy. *Journal of Neurosurgery*, 83(3):438–444, 1995.

[56] N. Yokose, K. Sakatani, Y. Murata, T. Awano, T. Igarashi, S. Nakamura, T. Hoshino, and Y. Katayama. Bedside monitoring of cerebral blood oxygenation and hemodynamics after aneurysmal subarachnoid hemorrhage by quantitative time-resolved near-infrared spectroscopy. *World Neurosurgery*, 73(5):508–513, 2010.

[57] F. Scholkmann, S. Kleiser, A. J. Metz, R. Zimmermann, J. M. Pavia, U. Wolf, and M. Wolf. A review on continuous wave functional near-infrared spectroscopy and imaging instrumentation and methodology. *NeuroImage*, 85(1):6–27, 2014.

[58] Wikipedia. Functional near-infrared spectroscopy – Wikipedia, the free encyclopedia. `http://upload.wikimedia.org/wikipedia/commons/6/6e/Oxy_and_Deoxy_Hemoglobin_Near-Infrared_absorption_spectra.png`. [Online; accessed 13 May 2015].

[59] R. D. Hoge. Calibrated fMRI. *NeuroImage*, 62(2):930–937, 2012.

[60] S. N. Krieger, C. J. Gauthier, D. Ivanov, L. Huber, E. Roggenhofer, B. Sehm, R. Turner, and G. F. Egan. Regional reproducibility of calibrated BOLD functional MRI: Implications for the study of cognition and plasticity. *NeuroImage*, 101:8–20, 2014.

[61] N. P. Blockley, V. E. M. Griffith, P. Jezzard, and D. P. Bulte. Cross-field analysis of hypercapnia calibrated BOLD. In *Proceedings of the 21st Annual Meeting ISMRM*, 2013.

[62] V. E. M. Griffeth, N. P. Blockley, A. B. Simon, and R. B. Buxton. A new functional MRI approach for investigating modulations of brain oxygen metabolism. *PloS One*, 8(6):e68122, 2013.

[63] W. van der Zwaag, S. Francis, K. Head, A. Peters, P. Gowland, P. Morris, and R. Bowtell. fMRI at 1.5, 3 and 7 T: characterising BOLD signal changes. *NeuroImage*, 47(4):1425–1434, 2009.

[64] V. E. M. Griffeth and R. B. Buxton. A theoretical framework for estimating cerebral oxygen metabolism changes using the calibrated-BOLD method: modeling the effects of blood volume distribution, hematocrit, oxygen extraction fraction, and tissue signal properties on the BOLD signal. *NeuroImage*, 58(1):198–212, 2011.

[65] J. M. Zhao, C. S. Clingman, M. J. Närväinen, R. A. Kauppinen, and P. van Zijl. Oxygenation and hematocrit dependence of transverse relaxation rates of blood at 3T. *Magnetic Resonance in Medicine*, 58(3):592–597, 2007.

[66] N. P. Blockley, L. Jiang, A. G. Gardener, C. N. Ludman, S. T. Francis, and P. A. Gowland. Field strength dependence of R1 and R2* relaxivities of human whole blood to prohance, vasovist, and deoxyhemoglobin. *Magnetic Resonance in Medicine*, 60(6):1313–1320, 2008.

[67] G. D. Hammer and S. J. McPhee. *Pathophysiology of Disease: An Introduction to Clinical Medicine, 6th Edition.* McGraw Hill Medical, 2009.

[68] J. S. Perlmutter, W. J. Powers, P. Herscovitch, P. T. Fox, and M. E. Raichle. Regional asymmetries of cerebral blood flow, blood volume, and oxygen utilization and extraction in normal subjects. *Journal of Cerebral Blood Flow & Metabolism*, 7(1):64–67, 1987.

[69] M. W. Woolrich, S. Jbabdi, B. Patenaude, M. Chappell, S. Makni, T. Behrens, C. Beckmann, M. Jenkinson, and S. M. Smith. Bayesian analysis of neuroimaging data in FSL. *NeuroImage*, 45(1):S173–S186, 2009.

[70] M. Jenkinson, P. Bannister, M. Brady, and S. Smith. Improved optimization for the robust and accurate linear registration and motion correction of brain images. *NeuroImage*, 17(2):825–841, 2002.

[71] S. M. Smith. Fast robust automated brain extraction. *Human Brain Mapping*, 17(3):143–155, 2002.

[72] M. Jenkinson, C. F. Beckmann, T. E. J. Behrens, M. W. Woolrich, and S. M. Smith. FSL. *NeuroImage*, 62(2):782–790, 2012.

[73] N. Kriegeskorte, W. K. Simmons, P. S. F. Bellgowan, and C. I. Baker. Circular analysis in systems neuroscience: the dangers of double dipping. *Nature Neuroscience*, 12(5):535–540, 2009.

[74] D. P. Bulte, K. Drescher, and P. Jezzard. Comparison of hypercapnia-based calibration techniques for measurement of cerebral oxygen metabolism with MRI. *Magnetic Resonance in Medicine*, 61(2):391–398, 2009.

[75] I. D. Driver, E. L. Hall, S. J. Wharton, S. E. Pritchard, S. T. Francis, and P. A. Gowland. Calibrated BOLD using direct measurement of changes in venous oxygenation. *NeuroImage*, 63(3):1178–1187, 2012.

[76] M. J. Donahue, J. U. Blicher, L. Østergaard, D. A. Feinberg, B. J. MacIntosh, K. L. Miller, M. Günther, and P. Jezzard. Cerebral blood flow, blood volume, and oxygen metabolism dynamics in human visual and motor cortex as measured by whole-brain multi-modal magnetic resonance imaging. *Journal of Cerebral Blood Flow & Metabolism*, 29(11):1856–1866, 2009.

[77] A. Kastrup, G. Krüger, T. Neumann-Haefelin, G. H. Glover, and M. E. Moseley. Changes of cerebral blood flow, oxygenation, and oxidative metabolism during graded motor activation. *NeuroImage*, 15(1):74–82, 2002.

[78] J. Petr, J.-C. Ferré, H. Raoult, E. Bannier, J.-Y. Gauvrit, and C. Barillot. Template-based approach for detecting motor task activation-related hyperperfusion in pulsed ASL data. *Human Brain Mapping*, 35(4):1179–1189, 2014.

[79] B. Stefanovic, J. M. Warnking, K. M. Rylander, and G. B. Pike. The effect of global cerebral vasodilation on focal activation hemodynamics. *NeuroImage*, 30(3):726–734, 2006.

[80] P. Vilela, M. Pimentel, I. Sousa, and P. Figueiredo. Quantification of perfusion changes during a motor task using arterial spin labeling. *The Neuroradiology Journal*, 24(1):85–91, 2011.

[81] B. Stefanovic, J. M. Warnking, and G. B. Pike. Hemodynamic and metabolic responses to neuronal inhibition. *NeuroImage*, 22(2):771–778, 2004.

[82] P. A. Chiarelli, D. P. Bulte, D. Gallichan, S. K. Piechnik, R. Wise, and P. Jezzard. Flow-metabolism coupling in human visual, motor, and supplementary motor areas assessed by magnetic resonance imaging. *Magnetic Resonance in Medicine*, 57(3):538–547, 2007.

[83] Y. Chen and T. B. Parrish. Caffeine's effects on cerebrovascular reactivity and coupling between cerebral blood flow and oxygen metabolism. *NeuroImage*, 44(3):647–652, 2009.

[84] B. M. Ances, O. Leontiev, J. E. Perthen, C. Liang, A. E. Lansing, and R. B. Buxton. Regional differences in the coupling of cerebral blood flow and oxygen metabolism changes in response to activation: implications for BOLD-fMRI. *NeuroImage*, 39(4):1510–1521, 2008.

[85] B. M. Ances, C. L. Liang, O. Leontiev, J. E. Perthen, A. S. Fleisher, A. E. Lansing, and R. B. Buxton. Effects of aging on cerebral blood flow, oxygen metabolism, and blood oxygenation level dependent responses to visual stimulation. *Human Brain Mapping*, 30(4):1120–1132, 2009.

[86] C. J. Gauthier, C. Madjar, F. B. Tancredi, B. Stefanovic, and R. D. Hoge. Elimination of visually evoked BOLD responses during carbogen inhalation: implications for calibrated MRI. *NeuroImage*, 54(2):1001–1011, 2011.

[87] A.-L. Lin, P. T. Fox, Y. Yang, H. Lu, L.-H. Tan, and J.-H. Gao. Evaluation of MRI models in the measurement of CMRO2 and its relationship with CBF. *Magnetic Resonance in Medicine*, 60(2):380–389, 2008.

[88] O. Leontiev and R. B. Buxton. Reproducibility of BOLD, perfusion, and CMRO2 measurements with calibrated-BOLD fMRI. *NeuroImage*, 35(1):175–184, 2007.

[89] J. E. Perthen, A. E. Lansing, J. Liau, T. T. Liu, and R. B. Buxton. Caffeine-induced uncoupling of cerebral blood flow and oxygen metabolism: a calibrated BOLD fMRI study. *NeuroImage*, 40(1):237–247, 2008.

[90] E. L. Hall, I. D. Driver, S. E. Pritchard, P. A. Gowland, and S. T. Francis. Voxel-wise estimation of M and CMRO2 at 7T. In *Proceedings of the ISMRM 20th Annual Meeting & Exhibition*, 2012.

[91] K. Uludağ, B. Müller-Bierl, and K. Uğurbil. An integrative model for neuronal activity-induced signal changes for gradient and spin echo functional imaging. *NeuroImage*, 48(1):150–165, 2009.

[92] F. B. Tancredi, C. J. Gauthier, C. Madjar, D. S. Bolar, J. A. Fisher, D. J. J. Wang, and R. D. Hoge. Comparison of pulsed and pseudocontinuous arterial spin-labeling for measuring CO2-induced cerebrovascular reactivity. *Journal of Magnetic Resonance Imaging*, 36(2):312–321, 2012.

[93] C. Triantafyllou, R. D. Hoge, G. Krueger, C. J. Wiggins, A. Potthast, G. C. Wiggins, and L. L. Wald. Comparison of physiological noise at 1.5 T, 3 T and 7 T and optimization of fMRI acquisition parameters. *NeuroImage*, 26(1):243–250, 2005.

[94] J. L. Boxerman, P. A. Bandettini, K. K. Kwong, J. R. Baker, T. L. Davis, B. R. Rosen, and R. M. Weisskoff. The intravascular contribution to fMRI signal change: Monte Carlo modeling and diffusion-weighted studies in vivo. *Magnetic Resonance in Medicine*, 34(1):4–10, 1995.

[95] S. Suri, C. E. Mackay, M. E. Kelly, M. Germuska, E. M. Tunbridge, G. B. Frisoni, P. M. Matthews, K. P. Ebmeier, D. P. Bulte, and N. Filippini. Reduced cerebrovascular reactivity in young adults carrying the APOE $\varepsilon4$ allele. *Alzheimer's & Dementia*, 11(6):648–657, 2015.

[96] J. C. Baron, M. G. Bousser, A. Rey, A. Guillard, D. Comar, and P. Castaigne. Reversal of focal "misery-perfusion syndrome" by extra-intracranial arterial bypass in hemodynamic cerebral ischemia. A case study with 15O positron emission tomography. *Stroke*, 12(4):454–459, 1981.

[97] G. Marchal, P. Rioux, M. C. Petit-Tabou, J. M. Derlon, J. C. Baron, C. Serrati, F. Viader, V. de la Sayette, F. Le Doze, P. Lochon, *et al.* PET imaging of cerebral perfusion and oxygen consumption in acute ischaemic stroke: relation to outcome. *The Lancet*, 341(8850):925–927, 1993.

[98] P. T. Fox and M. E. Raichle. Focal physiological uncoupling of cerebral blood flow and oxidative metabolism during somatosensory stimulation in human subjects. *Proceedings of the National Academy of Sciences*, 83(4):1140–1144, 1986.

[99] J.-C. Baron and T. Jones. Oxygen metabolism, oxygen extraction and positron emission tomography: historical perspective and impact on basic and clinical neuroscience. *NeuroImage*, 61(2):492–504, 2012.

[100] H. Ito, I. Kanno, C. Kato, T. Sasaki, K. Ishii, Y. Ouchi, A. Iida, H. Okazawa, K. Hayashida, N. Tsuyuguchi, *et al.* Database of normal human cerebral blood flow, cerebral blood volume, cerebral oxygen extraction fraction and cerebral metabolic rate of oxygen measured by positron emission tomography with 15O-labelled carbon dioxide or water, carbon monoxide and oxygen: a multicentre study in Japan. *European Journal of Nuclear Medicine and Molecular Imaging*, 31(5):635–643, 2004.

[101] M. Chappell, A. R. Groves, B. Whitcher, M. W. Woolrich, *et al.* Variational Bayesian inference for a nonlinear forward model. *IEEE Transactions on Signal Processing*, 57(1):223–236, 2009.

[102] M. Jones, J. Berwick, N. Hewson-Stoate, C. Gias, and J. Mayhew. The effect of hypercapnia on the neural and hemodynamic responses to somatosensory stimulation. *NeuroImage*, 27(3):609–623, 2005.

[103] J. P. Culver, T. Durduran, D. Furuya, C. Cheung, J. H. Greenberg, and A. G. Yodh. Diffuse optical tomography of cerebral blood flow, oxygenation, and metabolism in rat during focal ischemia. *Journal of Cerebral Blood Flow & Metabolism*, 23(8):911–924, 2003.

[104] J. M. Murkin and M. Arango. Near-infrared spectroscopy as an index of brain and tissue oxygenation. *British Journal of Anaesthesia*, 103(Suppl 1):i3–i13, 2009.

[105] P. E. Kinahan and J. G. Rogers. Analytic 3D image reconstruction using all detected events. *IEEE Transactions on Nuclear Science*, 36(1):964–968, 1989.

[106] J. P. Coles, T. D. Fryer, P. Smielewski, K. Rice, J. C. Clark, J. D. Pickard, and D. K. Menon. Defining ischemic burden after traumatic brain injury using 15O PET imaging of cerebral physiology. *Journal of Cerebral Blood Flow & Metabolism*, 24(2):191–201, 2004.

[107] R. S. J. Frackowiak, G.-L. Lenzi, T. Jones, and J. D. Heather. Quantitative measurement of regional cerebral blood flow and oxygen metabolism in man using 15O and positron emission tomography: theory, procedure, and normal values. *Journal of Computer Assisted Tomography*, 4(6):727–736, 1980.

[108] A. A. Lammertsma, J.-C. Baron, and T. Jones. Correction for intravascular activity in the oxygen-15 steady-state technique is independent of the regional hematocrit. *Journal of Cerebral Blood Flow & Metabolism*, 7(3):372–374, 1987.

[109] P. Herscovitch and M. E. Raichle. What is the correct value for the brain–blood partition coefficient for water? *Journal of Cerebral Blood Flow & Metabolism*, 5(1):65–69, 1985.

[110] M. E. Phelps, S. C. Huang, E. J. Hoffman, and D. E. Kuhl. Validation of tomographic measurement of cerebral blood volume with C-11-labeled carboxyhemoglobin. *Journal of Nuclear Medicine*, 20(4):328–334, 1979.

[111] P. Smielewski, J. P. Coles, T. D. Fryer, P. S. Minhas, D. K. Menon, and J. D. Pickard. Integrated image analysis solutions for PET datasets in damaged brain. *Journal of Clinical Monitoring and Computing*, 17(7-8):427–440, 2002.

[112] Y. Zhang, M. Brady, and S. Smith. Segmentation of brain MR images through a hidden Markov random field model and the expectation-maximization algorithm. *IEEE Transactions on Medical Imaging*, 20(1):45–57, 2001.

[113] L. W. Golen, J. Kuijer, M. C. Huisman, R. G. IJzerman, F. Barkhof, M. Diamant, and A. A. Lammertsma. Quantification of cerebral blood flow in healthy volunteers and type 1 diabetic patients: Comparison of MRI arterial spin labeling and [15O] H2O positron emission tomography (PET). *Journal of Magnetic Resonance Imaging*, 40(6):1300–1309, 2014.

[114] K. Zhang, H. Herzog, J. Mauler, C. Filss, T. W. Okell, E. R. Kops, L. Tellmann, T. Fischer, B. Brocke, W. Sturm, *et al.* Comparison of cerebral blood flow acquired by simultaneous [15O] water positron emission tomography and arterial spin labeling magnetic resonance imaging. *Journal of Cerebral Blood Flow & Metabolism*, 34(8):1373–1380, 2014.

[115] J. B. De Vis, J. Hendrikse, A. Bhogal, A. Adams, L. J. Kappelle, and E. T. Petersen. Age-related changes in brain hemodynamics; a calibrated MRI study. *Human Brain Mapping*, 2015. DOI: 10.1002/hbm.22891.

[116] C. C. Faraco, M. K. Strother, L. M. Dethrage, L. Jordan, R. Singer, P. F. Clemmons, and M. J. Donahue. Dual echo vessel-encoded ASL for simultaneous BOLD and CBF reactivity assessment in patients with ischemic cerebrovascular disease. *Magnetic Resonance in Medicine*, 73(4):1579–1592, 2015.

[117] H. V. Hare, M. Germuska, M. E. Kelly, and D. P. Bulte. Comparison of CO2 in air versus carbogen for the measurement of cerebrovascular reactivity with magnetic resonance imaging. *Journal of Cerebral Blood Flow & Metabolism*, 33(11):1799–1805, 2013.

[118] A. B. Simon, V. E. Griffeth, E. C. Wong, and R. B. Buxton. A novel method of combining blood oxygenation and blood flow sensitive magnetic resonance imaging techniques to measure the cerebral blood flow and oxygen metabolism responses to an unknown neural stimulus. *PloS One*, 8(1):e54816, 2013.

[119] F. Xu, J. Uh, M. R. Brier, J. Hart, U. S. Yezhuvath, H. Gu, Y. Yang, and H. Lu. The influence of carbon dioxide on brain activity and metabolism in conscious humans. *Journal of Cerebral Blood Flow & Metabolism*, 31(1):58–67, 2011.

[120] D. P. Bulte, P. A. Chiarelli, R. G. Wise, and P. Jezzard. Cerebral perfusion response to hyperoxia. *Journal of Cerebral Blood Flow & Metabolism*, 27(1):69–75, 2007.

[121] J. B. De Vis, E. T. Petersen, A. Bhogal, N. S. Hartkamp, C. J. M. Klijn, L. J. Kappelle, and J. Hendrikse. Calibrated MRI to evaluate cerebral hemodynamics in patients with an internal carotid artery occlusion. *Journal of Cerebral Blood Flow & Metabolism*, 35(6):1015–1023, 2015.

[122] J. Simpson, N. Sudhan, H. Hare, J. Donnelly, X. Liu, F. Aigbirhio, T. Fryer, G. Stocks-Gee, P. Smielewski, D. Bulte, *et al.* Comparison of 15oxygen positron emission tomography and near-infrared spectroscopy for measurement of cerebral physiology. *Critical Care*, 19(Suppl 1):445, 2015.

[123] T. Alderliesten, J. B. De Vis, P. M. A. Lemmers, F. Van Bel, M. J. N. L. Benders, J. Hendrikse, and E. T. Petersen. Simultaneous quantitative assessment of cerebral physiology using respiratory-calibrated MRI and near-infrared spectroscopy in healthy adults. *NeuroImage*, 85:255–263, 2014.

[124] J. C. W. Brooks, C. F. Beckmann, K. L. Miller, R. G. Wise, C. A. Porro, I. Tracey, and M. Jenkinson. Physiological noise modelling for spinal functional magnetic resonance imaging studies. *NeuroImage*, 39(2):680–692, 2008.

[125] E. Lüders, H. Steinmetz, and L. Jäncke. Brain size and grey matter volume in the healthy human brain. *NeuroReport*, 13(17):2371–2374, 2002.

[126] H. V. Hare, N. P. Blockley, A. G. Gardener, S. Clare, and D. P. Bulte. Investigating the field-dependence of the Davis model: Calibrated fMRI at 1.5, 3 and 7T. *NeuroImage*, 112:189–196, 2015.

[127] R. G. Wise, K. T. S. Pattinson, D. P. Bulte, P. A. Chiarelli, S. D. Mayhew, G. M. Balanos, D. F. O'Connor, T. R. Pragnell, P. A. Robbins, I. Tracey, *et al.* Dynamic forcing of end-tidal carbon dioxide and oxygen applied to functional magnetic resonance imaging. *Journal of Cerebral Blood Flow & Metabolism*, 27(8):1521–1532, 2007.

[128] D. M. Mandell, J. S. Han, J. Poublanc, A. P. Crawley, J. A. Stainsby, J. A. Fisher, and D. J. Mikulis. Mapping cerebrovascular reactivity using blood oxygen level-dependent MRI in patients with arterial steno-occlusive disease comparison with arterial spin labeling MRI. *Stroke*, 39(7):2021–2028, 2008.

[129] M. J. Donahue, M. Ayad, R. Moore, M. Osch, R. Singer, P. Clemmons, and M. Strother. Relationships between hypercarbic reactivity, cerebral blood flow, and arterial circulation times in patients with moyamoya disease. *Journal of Magnetic Resonance Imaging*, 38(5):1129–1139, 2013.

[130] P. Van Gelderen, J. A. De Zwart, and J. H. Duyn. Pittfalls of MRI measurement of white matter perfusion based on arterial spin labeling. *Magnetic Resonance in Medicine*, 59(4):788–795, 2008.

[131] D. Le Bihan, E. Breton, D. Lallemand, M. L. Aubin, J. Vignaud, and M. Laval-Jeantet. Separation of diffusion and perfusion in intravoxel incoherent motion MR imaging. *Radiology*, 168(2):497–505, 1988.

[132] W. Meier-Ruge, O. Hunziker, U. Schulz, H.-J. Tobler, and A. Schweizer. Stereological changes in the capillary network and nerve cells of the aging human brain. *Mechanisms of Ageing and Development*, 14(1):233–243, 1980.

[133] A. Løkkegaard, J. R. Nyengaard, and M. J. West. Stereological estimates of number and length of capillaries in subdivisions of the human hippocampal region. *Hippocampus*, 11(6):726–740, 2001.

[134] F. Lauwers, F. Cassot, V. Lauwers-Cances, P. Puwanarajah, and H. Duvernoy. Morphometry of the human cerebral cortex microcirculation: general characteristics and space-related profiles. *NeuroImage*, 39(3):936–948, 2008.

[135] I. Joo, J. M. Lee, J. K. Han, and B. I. Choi. Intravoxel incoherent motion diffusion-weighted MR imaging for monitoring the therapeutic efficacy of the vascular disrupting agent CKD-516 in rabbit VX2 liver tumors. *Radiology*, 272(2):417–426, 2014.

[136] B. Guiu, J.-M. Petit, V. Capitan, S. Aho, D. Masson, P.-H. Lefevre, S. Favelier, R. Loffroy, B. Vergès, P. Hillon, *et al.* Intravoxel incoherent motion diffusion-weighted imaging in nonalcoholic fatty liver disease: a 3.0-T MR study. *Radiology*, 265(1):96–103, 2012.

[137] I. Yamada, W. Aung, Y. Himeno, T. Nakagawa, and H. Shibuya. Diffusion coefficients in abdominal organs and hepatic lesions: evaluation with intravoxel incoherent motion echo-planar MR imaging. *Radiology*, 210(3):617–623, 1999.

[138] A. Luciani, A. Vignaud, M. Cavet, J. Tran Van Nhieu, A. Mallat, L. Ruel, A. Laurent, J.-F. Deux, P. Brugieres, and A. Rahmouni. Liver cirrhosis: intravoxel incoherent motion MR imaging – pilot study 1. *Radiology*, 249(3):891–899, 2008.

[139] A. M. Chow, D. S. Gao, S. J. Fan, Z. Qiao, F. Y. Lee, J. Yang, K. Man, and E. X. Wu. Liver fibrosis: an intravoxel incoherent motion (IVIM) study. *Journal of Magnetic Resonance Imaging*, 36(1):159–167, 2012.

[140] T. A. Powers, C. Lorenz, G. E. Holburn, and R. R. Price. Renal artery stenosis: in vivo perfusion MR imaging. *Radiology*, 178(2):543–548, 1991.

[141] E. E. Sigmund, P.-H. Vivier, D. Sui, N. A. Lamparello, K. Tantillo, A. Mikheev, H. Rusinek, J. S. Babb, P. Storey, V. S. Lee, *et al.* Intravoxel incoherent motion and diffusion-tensor imaging in renal tissue under hydration and furosemide flow challenges. *Radiology*, 263(3):758–769, 2012.

[142] H. Chandarana, S. K. Kang, S. Wong, H. Rusinek, J. L. Zhang, S. Arizono, W. C. Huang, J. Melamed, J. S. Babb, E. F. Suan, *et al.* Diffusion-weighted intravoxel incoherent motion imaging of renal tumors with histopathologic correlation. *Investigative Radiology*, 47(12):688–696, 2012.

[143] K. M. Kang, J. M. Lee, J. H. Yoon, B. Kiefer, J. K. Han, and B. I. Choi. Intravoxel incoherent motion diffusion-weighted MR imaging for characterization of focal pancreatic lesions. *Radiology*, 270(2):444–453, 2014.

[144] T. J. Re, A. Lemke, M. Klauss, F. B. Laun, D. Simon, K. Grünberg, S. Delorme, L. Grenacher, R. Manfredi, R. P. Mucelli, *et al.* Enhancing pancreatic adenocarcinoma delineation in diffusion derived intravoxel incoherent motion f-maps through automatic vessel and duct segmentation. *Magnetic Resonance in Medicine*, 66(5):1327–1332, 2011.

[145] A. Lemke, F. B. Laun, D. Simon, B. Stieltjes, and L. R. Schad. An in vivo verification of the intravoxel incoherent motion effect in diffusion-weighted imaging of the abdomen. *Magnetic Resonance in Medicine*, 64(6):1580–1585, 2010.

[146] S. Bisdas. Are we ready to image the incoherent molecular motion in our minds? *Neuroradiology*, 55(5):537–540, 2013.

[147] R. M. Henkelman. Does IVIM measure classical perfusion? *Magnetic Resonance in Medicine*, 16(3):470–475, 1990.

[148] S. Suo, N. Lin, H. Wang, L. Zhang, R. Wang, S. Zhang, J. Hua, and J. Xu. Intravoxel incoherent motion diffusion-weighted MR imaging of breast cancer at 3.0 tesla: Comparison of different curve-fitting methods. *Journal of Magnetic Resonance Imaging*, 42(2):362–370, 2014.

[149] A. Lemke, B. Stieltjes, L. R. Schad, and F. B. Laun. Toward an optimal distribution of b values for intravoxel incoherent motion imaging. *Magnetic Resonance Imaging*, 29(6):766–776, 2011.

[150] Y. Pang, B. Turkbey, M. Bernardo, J. Kruecker, S. Kadoury, M. J. Merino, B. J. Wood, P. A. Pinto, and P. L. Choyke. Intravoxel incoherent motion MR imaging for prostate cancer: An evaluation of perfusion fraction and diffusion coefficient derived from different b-value combinations. *Magnetic Resonance in Medicine*, 69(2):553–562, 2013.

[151] W.-C. Wu, Y.-F. Chen, H.-M. Tseng, and S.-C. Yang. Caveat of measuring perfusion indexes using intravoxel incoherent motion magnetic resonance imaging in the human brain. *European Radiology*, 25(8):2485–2492, 2015.

[152] J. Pekar, C. T. Moonen, and P. van Zijl. On the precision of diffusion/perfusion imaging by gradient sensitization. *Magnetic Resonance in Medicine*, 23(1):122–129, 1992.

[153] K. K. Kwong, R. C. McKinstry, D. Chien, A. P. Crawley, J. D. Pearlman, and B. R. Rosen. CSF-suppressed quantitative single-shot diffusion imaging. *Magnetic Resonance in Medicine*, 21(1):157–163, 1991.

[154] M. Sumi, M. Van Cauteren, T. Sumi, M. Obara, Y. Ichikawa, and T. Nakamura. Salivary gland tumors: use of intravoxel incoherent motion MR imaging for assessment of diffusion and perfusion for the differentiation of benign from malignant tumors. *Radiology*, 263(3):770–777, 2012.

[155] T. Hauser, M. Essig, A. Jensen, L. Gerigk, F. B. Laun, M. Münter, D. Simon, and B. Stieltjes. Characterization and therapy monitoring of head and neck carcinomas using diffusion-imaging-based intravoxel incoherent motion parameters – preliminary results. *Neuroradiology*, 55(5):527–536, 2013.

[156] C. H. Suh, H. S. Kim, S. S. Lee, N. Kim, H. M. Yoon, C.-G. Choi, and S. J. Kim. Atypical imaging features of primary central nervous system lymphoma that mimics glioblastoma: utility of intravoxel incoherent motion MR imaging. *Radiology*, 272(2):504–513, 2014.

[157] C. Federau, K. O'Brien, R. Meuli, P. Hagmann, and P. Maeder. Measuring brain perfusion with intravoxel incoherent motion (IVIM): initial clinical experience. *Journal of Magnetic Resonance Imaging*, 39(3):624–632, 2014.

[158] D. Y. Kim, H. S. Kim, M. J. Goh, C. G. Choi, and S. J. Kim. Utility of intravoxel incoherent motion MR imaging for distinguishing recurrent metastatic tumor from treatment effect following gamma knife radiosurgery: Initial experience. *American Journal of Neuroradiology*, 35(11):2082–2090, 2014.

[159] C. Federau, P. Maeder, K. O'Brien, P. Browaeys, R. Meuli, and P. Hagmann. Quantitative measurement of brain perfusion with intravoxel incoherent motion MR imaging. *Radiology*, 265(3):874–881, 2012.

[160] C. Federau, K. O'Brien, A. Birbaumer, R. Meuli, P. Hagmann, and P. Maeder. Functional mapping of the human visual cortex with intravoxel incoherent motion MRI. *PloS One*, 10(2):e0117706, 2015.

[161] R. C. McKinstry, R. M. Weiskoff, J. W. Belliveau, J. M. Vevea, J. B. Moore, K. W. Kwong, E. F. Halpern, and B. R. Rosen. Ultrafast MR imaging of water mobility: animal models of altered cerebral perfusion. *Journal of Magnetic Resonance Imaging*, 2(4):377–384, 1992.

[162] D. F. R. Heijtel, H. J. M. M. Mutsaerts, E. Bakker, P. Schober, M. F. Stevens, E. T. Petersen, B. N. M. van Berckel, C. B. L. M. Majoie, J. Booij, M. J. P. van Osch, *et al.* Accuracy and precision of pseudo-continuous arterial spin labeling perfusion during baseline and hypercapnia: A head-to-head comparison with 15O H2O positron emission tomography. *NeuroImage*, 92:182–192, 2014.

[163] T. G. Reese, O. Heid, R. M. Weisskoff, and V. J. Wedeen. Reduction of eddy-current-induced distortion in diffusion MRI using a twice-refocused spin echo. *Magnetic Resonance in Medicine*, 49(1):177–182, 2003.

[164] M. Webster. FUGUE. `http://fsl.fmrib.ox.ac.uk/fsl/fslwiki/FUGUE`. [Online; accessed 14 August 2015].

[165] S. Smith. FDT. `http://fsl.fmrib.ox.ac.uk/fsl/fslwiki/FDT`. [Online; accessed 14 August 2015].

[166] J. L. R. Andersson, S. Skare, and J. Ashburner. How to correct susceptibility distortions in spin-echo echo-planar images: application to diffusion tensor imaging. *NeuroImage*, 20(2):870–888, 2003.

[167] R. Wirestam, M. Borg, S. Brockstedt, A. Lindgren, S. Holtås, and F. Ståhlberg. Perfusion-related parameters in intravoxel incoherent motion MR imaging compared with CBV and CBF measured by dynamic susceptibility-contrast MR technique. *Acta Radiologica*, 42(2):123–128, 2001.

[168] Y. Lin, J. Li, Z. Zhang, Q. Xu, Z. Zhou, Z. Zhang, Y. Zhang, and Z. Zhang. Comparison of intravoxel incoherent motion diffusion-weighted MR imaging and arterial spin labeling MR imaging in gliomas. *BioMed Research International*, 2015. DOI: 10.1155/2015/234245.

[169] P. Pantano, J. C. Baron, P. Lebrun-Grandie, N. Duquesnoy, M. G. Bousser, and D. Comar. Regional cerebral blood flow and oxygen consumption in human aging. *Stroke*, 15(4):635–641, 1984.

[170] S. Fantini. Dynamic model for the tissue concentration and oxygen saturation of hemoglobin in relation to blood volume, flow velocity, and oxygen consumption: Implications for functional neuroimaging and coherent hemodynamics spectroscopy (CHS). *NeuroImage*, 85:202–221, 2014.

[171] C. Federau and K. O'Brien. Increased brain perfusion contrast with T2-prepared intravoxel incoherent motion (T2prep IVIM) MRI. *NMR in Biomedicine*, 28(1):9–16, 2015.

[172] C. Federau, P. Hagmann, P. Maeder, M. Müller, R. Meuli, M. Stuber, and K. O'Brien. Dependence of brain intravoxel incoherent motion perfusion parameters on the cardiac cycle. *PloS One*, 8(8):e72856, 2013.

[173] A. Scouten and R. T. Constable. VASO-based calculations of CBV change: Accounting for the dynamic CSF volume. *Magnetic Resonance in Medicine*, 59(2):308–315, 2008.